Multidirectional Seismic Excitation Effects in Building Response Estimation: Collaborative Research with USGS (Dr. Nicolas Luco) and AIR

AWARD No. **06HQGR0011**

Drs. Paolo Bazzurro, Jaesung Park, and Polsak Tothong
AIR Worldwide Corporation
388 Market Street, Suite 610
San Francisco, CA 94111
415/912-3111 (phone)
415/912-3112 (fax)
pbazzurro@air-worldwide.com
jpark@air-worldwide.com
ptothong@air-worldwide.com

in collaboration with
Dr. Nicolas Luco(USGS)

TABLE OF CONTENTS

ABSTRACT

This study provides insights in the seismic performance assessment of structures subject to multi-directional ground motions. A seven story brittle concrete moment resisting frame building designed in the 1960's is selected as the case study. The building performance is statistically evaluated by running many real ground motion recordings through a computer model of the structure and monitoring response measures of interest (e.g., the maximum peak interstory drift ratio, δ_{max}). The values of such response measures are then "predicted" based on appropriate ground motion parameters, called Intensity Measures or IM's, which characterize the intensity of the shaking applied. Engineers often seek to obtain a high accuracy in structural response assessment by developing complex two-dimensional (2D) and three-dimensional (3D) models of their buildings and by applying several IM's to estimate the structural response. On the hazard side, well established tools such Probabilistic Seismic Hazard Analysis (PSHA) and the recently developed vectorized extension of it, called here the Vector PSHA are used to estimate how often ground motions with such parameters may occur at the site of interest. The coupling of the seismic hazard and response prediction leads to the computation of the site-specific and building-specific drift hazard curves, which can be used for assessing the performance of the building versus life safety and serviceability requirements.

The application of this procedure to real life structures requires that the link between seismic hazard and structural response be done seamlessly. The consensus of how this "coupling" should be performed, however, has not yet been reached especially when the building is modeled as a 3D entity. Also, it is unclear how the analyses should be performed when the main axes of the building are aligned with the strike of the main causative faults in the area and what are the consequences of neglecting to incorporate the building orientation into the analyses.

This study has addressed the following issues pertinent to computing the likelihood of exceeding acceptable seismic responses for buildings located close to faults: a) effects of modeling the structure with increasing levels of complexity (two frames in 2 Dimensions or a single 3 Dimensional model) on the drift hazard curves, b) predicting the building response with different orientations with respect to the causative fault using several combinations of ground motion parameters, and c) coupling the site hazard (both scalar and vector) with the building response. The study also briefly addressed the so-called 30%-rule prescribed by building codes to design corner columns belonging to moment resisting frames of buildings subject to multi-directional ground motions. The main lessons learned from this study are:

a) Modeling a structure as a 2D frame or as a 3D entity can result in quite different drift hazard curves and especially different collapse probabilities. When designing 2D frames attention should be devoted to the modeling of the gravity frames if very large deformations are to be predicted accurately. When gravity frames are excluded and leaning columns only are used, then large deformations can be overestimated.
b) Orientation of this building with respect to the fault strike changed the probability of collapse by as much as 70%.
c) The selection of the IM to be used as predictor of building response is important because, for the same building orientation, the drift hazard curves that result may vary by a factor of 2 or more at larger drifts. IM's yielding the smallest level of response variability should be preferred.
d) The 30%-rule appears to be unconservative in most cases of practical interest due to the high correlations of ground motion parameters acting along the main orthogonal axes of the building.

1   SCOPE OF WORK AND MOTIVATION

This study provides insights in the seismic performance assessment of structures subject to multi-directional ground motions. In state-of-the-art and advanced state-of-practice studies, the assessment is done by coupling the likelihood that a structure will undergo severe response levels associated with undesirable limit states (e.g., major damage or collapse) when subject to ground motions of given intensity with the likelihood that such ground motions may be experienced at the structure site. In this study the response assessment was performed for a building but this methodology is general and it can be applied to other types of structures, such as bridges, dams, and offshore platforms.

The building performance is statistically evaluated by running many real ground motion recordings through a computer model of the structure and monitoring response measures of interest (e.g., maximum peak interstory drift ratio). The values of such response measures are then "predicted" based on appropriate ground motion parameters, called Intensity Measures or IM's, which characterize the intensity of the shaking applied. Engineers often seek to obtain a high accuracy in structural response assessment by developing complex two-dimensional (2D) and three-dimensional (3D) models of their buildings and by applying several IM's to estimate the structural response. On the hazard side, well established tools such Probabilistic Seismic Hazard Analysis (PSHA) and the recently developed vectorized extension of it, called here the Vector PSHA or VPSHA for short, are used to estimate how often ground motions with such parameters may occur at the site of interest.

The application of this procedure to real life structures requires that the link between seismic hazard and structural response be done seamlessly. The consensus of how this "coupling" should be performed, however, has not yet been reached especially when the building is modeled as a 3D entity. Existing building codes and guidelines do not offer much guidance. For example, when the structure is modeled as two separate frames aligned in the directions of its principal axes it is unclear how the response and therefore the likelihood that a certain performance may not be met in the two main orthogonal directions should be combined. When a 3D model is chosen, on the other hand, the coupling with the hazard requires the use of the still rather unfamiliar VPSHA tool and recently developed covariance matrices of various ground motion parameters.

This study investigates how seismic hazard and response of a building should (and should not) be coupled to evaluate the adequacy of its seismic performance. Here we have modeled a mid-rise, seven-story concrete frame building that was built in Van Nuys, California. We considered *three different orientations* of its main axes (two aligned and one at an undefined angle) with respect to the strike of the main nearby faults. To mimic the levels of modeling adopted by engineers in projects of different budgets, we have considered *four modeling options*: a) single-degree-of-freedom (SDOF) system, b) two-degree-of-freedom (2DOF) bi-directional system, c) two separate orthogonal 2D frames, and d) a 3D frame. Only cases c) and d) are discussed here. As response predictors, we have considered multiple combinations of spectral accelerations at the frequencies corresponding to the fundamental and second modes of vibration of the building in the longitudinal and transverse direction and to other frequencies in between. In addition to the elastic IM's above, we also have considered the inelastic spectral displacement at the fundamental period of the building. We used PSHA and VPSHA to estimate the rate of occurrence of such IM's at the building site. For this exercise we assumed that the building is located in San Francisco rather than Van Nuys. The San Francisco site, being close to major faults of same strike-slip mechanism and similar orientation such as the San Andreas and the Hayward Faults, shows an anisotropic seismic hazard at longer periods due to directivity effects that make the chances of observing an IM level higher in the fault-normal (i.e., approximately E-W) direction. Given the multitude of faults with different orientations and rupture mechanisms in Southern California, the seismic hazard at the Van Nuys site is much more isotropic. The effect of the anisotropy of the seismic hazard on building performance is one of the aspects that this study intends to address.

4

2   ANALYSIS SET-UP

2.1   *Description and validation of the building models*

For this study, we have considered a seven-story, 3 bay-by-8 bay concrete moment-resisting frame building without seismic detailing built in 1965 in Van Nuys, California. The height of the first story is 4.12m while the height of all the other stories is approximately the same and equal to 2.65m. This building was selected for three reasons:

a. The building was instrumented when both the Whittier Narrows and the Northridge Earthquakes struck Southern California. The building motion recordings allow a calibration of the computer model and, therefore, a more realistic building response assessment.
b. It has been extensively studied (e.g., Doulatabadi, 1997; PEER, 2005; Jalayer, 2006). Models of the two perpendicular frames and of the 3-Dimensional structure were already developed by researchers at the Pacific Earthquake Engineering Research (PEER) Center and at the University of British Columbia in Vancouver, Canada, using different computer software packages.
c. This rather weak and brittle building is expected to undergo severe nonlinear behavior and at times collapse (i.e., numerical instability due to excessively large displacements) when subject to the array of strong ground motions selected for this project. The realm of severe post-elastic behavior is where the application of these probabilistic response and risk assessment methods is more fruitful.

The more complex 2D and 3D computer representations of this building were developed at AIR while the simpler SDOF and 2DOF models were assembled at USGS. Only the 2D and 3D models are discussed in details here while the SDOF and 2DOF models are part of a separate report by Dr. Luco. In the attempt of achieving a better consistency between numerical results and field observations, we used recent advancements in numerical structural analysis technology and re-modeled the building within the OpenSees analysis platform (OpenSees, 2002). The columns and beams of the models follow the centerline dimensions of the building plan (Doulatabadi, 1997; PEER, 2005; Theiss, 2005). The perimeter moment frames are designed to resist the lateral forces and modeled using non-linear beam-column element with 5 point integration along the element. All column elements consider the second-order P-Delta effects. The interior gravity system comprises 2-way reinforced concrete flat slabs supported by interior columns. The slab is modeled with nonlinear beam-column elements that consider the effective width of the slab. Each nonlinear beam-column element comprises fiber sections, whose geometry is defined in the building plan. The uni-axial material behavior of the concrete is simulated using the OpenSees Concrete02 material model with three different strength levels along the height of the building. Due to the low transverse reinforcement ratio of this building design, all columns and beams are considered as unconfined. The response of reinforcing steel for Grade 40 and 60 in the axial direction is simulated using the OpenSees Steel02 material model. The brittle shear failure of exterior columns observed in the event of Northridge earthquake is simulated using the limitState and limitCurve model in the OpenSees (Elwood and Moehle, 2003). The shear failure model defines the shear strength as a function of inter-story drift, axial load, and section properties. The limitCurve models at the 3rd, 4th, and 5th stories, where the shear failures occurred at Northridge earthquake, are calibrated using the delta parameter in the model to get good agreement with the physical observations after the Northridge earthquake and the floor displacement recordings.

The OpenSees 3D model of the building is shown in Figure 1 and the 2D models of the longitudinal and transverse frames of the same building are shown in Figure 2 and Figure 3, respectively. Figure 4 displays the non-linear beam-column elements of the OpenSees 3D model with a view of the fiber sections in

three-dimensional space. The 2D longitudinal building model has a dual-frame configuration with rigid diaphragm consisting of a perimeter moment-resisting frame and an interior gravity frame. The interior gravity frame can fail in flexure but not in shear. In the transverse direction the 2D model includes instead a leaning column but not a gravity frame. This is done intentionally to mimic the most widely used practice where the response contribution of gravity frames is excluded. An example of calibrated limitState and limitCurve models for a column is displayed in Figure 5 where shear failure occurs at about 1.5% interstory drift. The shear springs in the columns at the other floors were assumed to fail between 2.5 and 4% drift ratio. Note that the horizontal shear springs in the two orthogonal directions in the 3D model are not coupled. The uncoupling implies that a column may retain its original shear capacity in one direction while it has failed in the perpendicular direction. This is certainly a limitation of the 3D model.

The accuracy of the simulated response of the 3D and 2D models has been tested using the recordings of the motion that this building experienced during the 1994 Northridge earthquake. The location of the sensors in the building is shown in Figure 6. Figure 7 and Figure 8 show the comparison between the simulated (3D Model) and the recorded total floor displacement time histories (THs) in the longitudinal and in the transverse directions, respectively, during the Northridge earthquake. The agreement between the recorded and simulated THs is very good especially at the lower floors. Using the 2D models, similar comparisons for both total floor displacement and floor displacement relative to the ground are shown for the longitudinal direction in Figure 9 and Figure 10, respectively, and for the transverse direction in Figure 11 and Figure 12, respectively. The agreement in these cases is excellent also at higher floors.

The elastic first and second mode periods of vibration of the building for modes acting prevalently along the two main orthogonal axes are

- **3D model**: T_{L1}=1.38s; T_{L2}=0.46s; T_{T1}=1.25s; T_{T2}=0.43s;
- **2D models**: T_{L1}=1.39s; T_{L2}=0.47s; T_{T1}=1.22; T_{T2}=0.41s;

where the subscript L stands for longitudinal direction, the subscript T for transverse direction, and the subscripts 1 and 2 refer to the first and the second mode periods of vibration in the direction under consideration, respectively. The mode shapes corresponding of the first modes of vibration in longitudinal and transverse directions are shown in Figure 13.
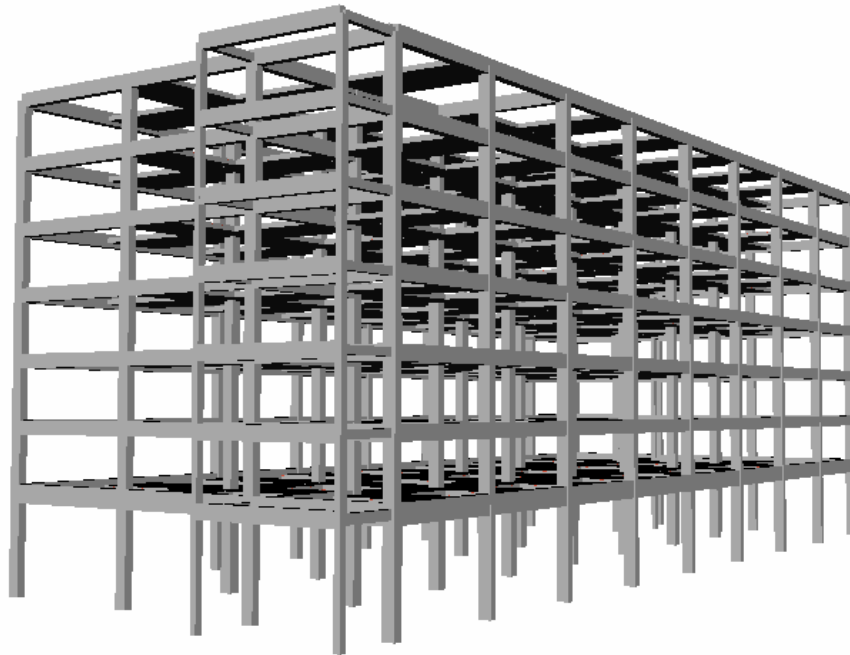
**Figure 1** 3D model of Van Nuys building developed using OpenSees.
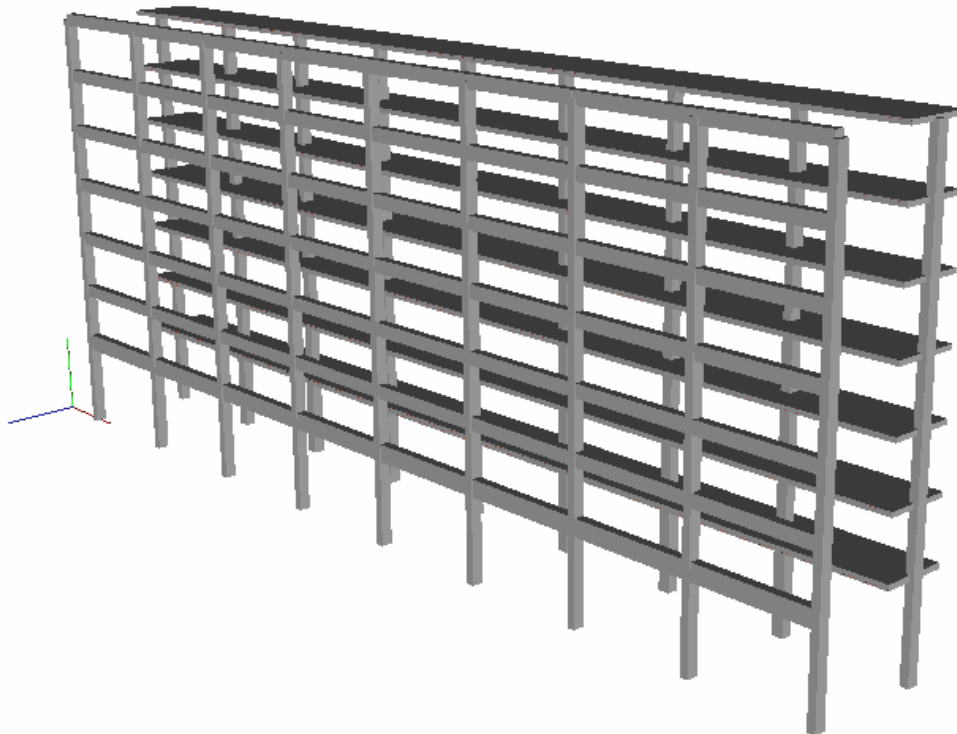
Figure 2 2D model of the longitudinal frame of the Van Nuys building developed using OpenSees.
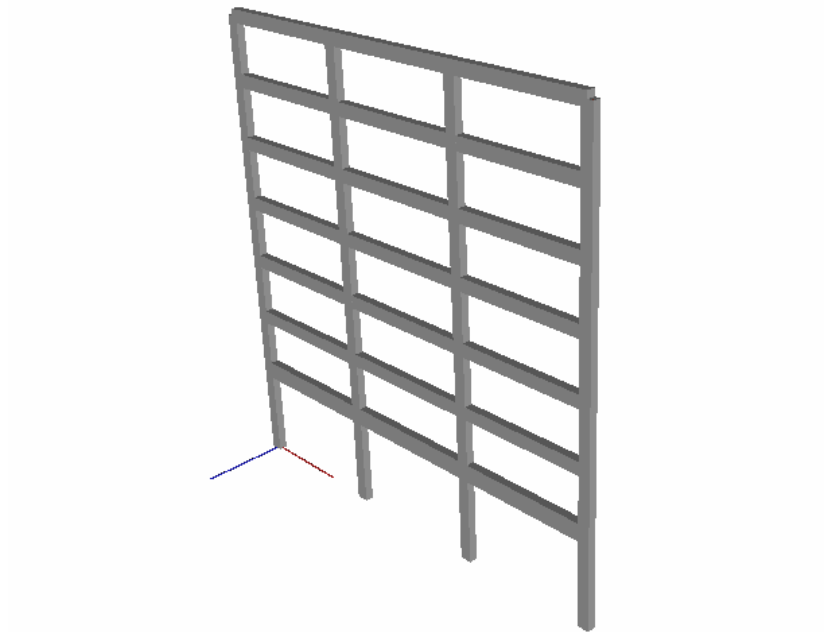
Figure 3 2D model of the transverse frame of the Van Nuys building developed using OpenSees.
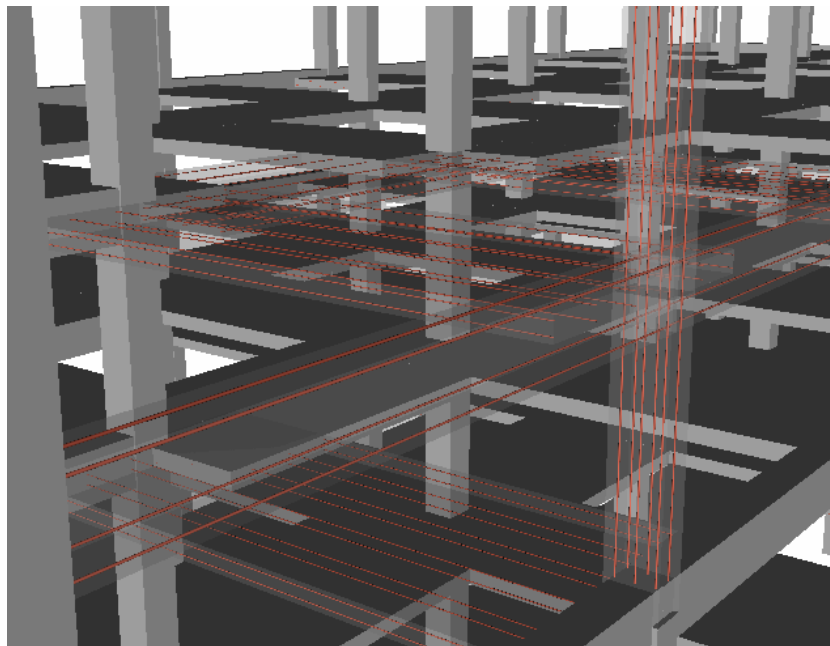
Figure 4 Details of the steel rebars in slabs, beams and columns included in the model.
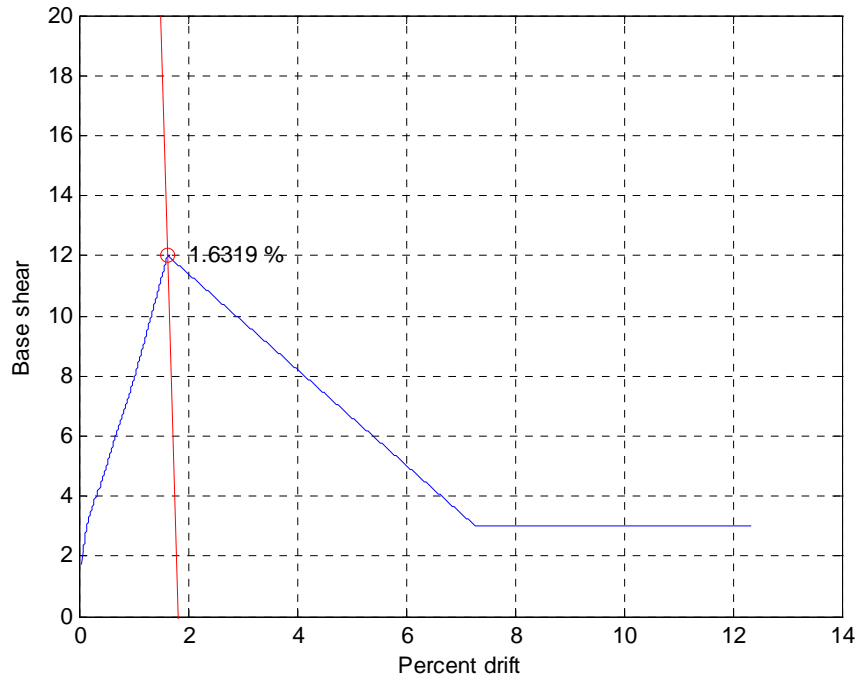
Figure 5. Example of limitState (blue line) and limitCurve (red line) for one of the columns at the 3rd, 4th, and 5th story of the exterior moment resisting frame. The springs at all the other stories fail between 2.5 and 4% interstory drift ratio.
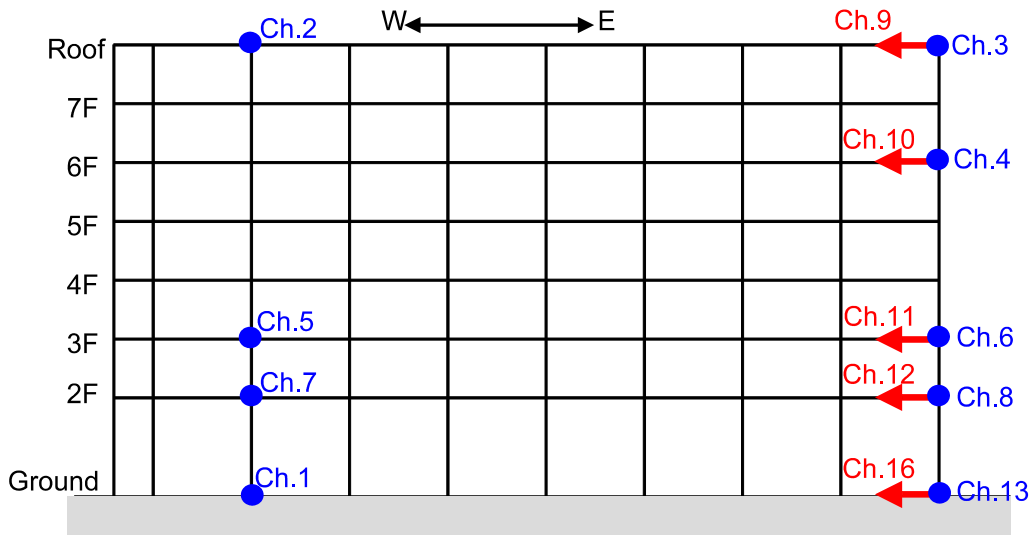
Figure 6 Sensor locations in the Van Nuys building.
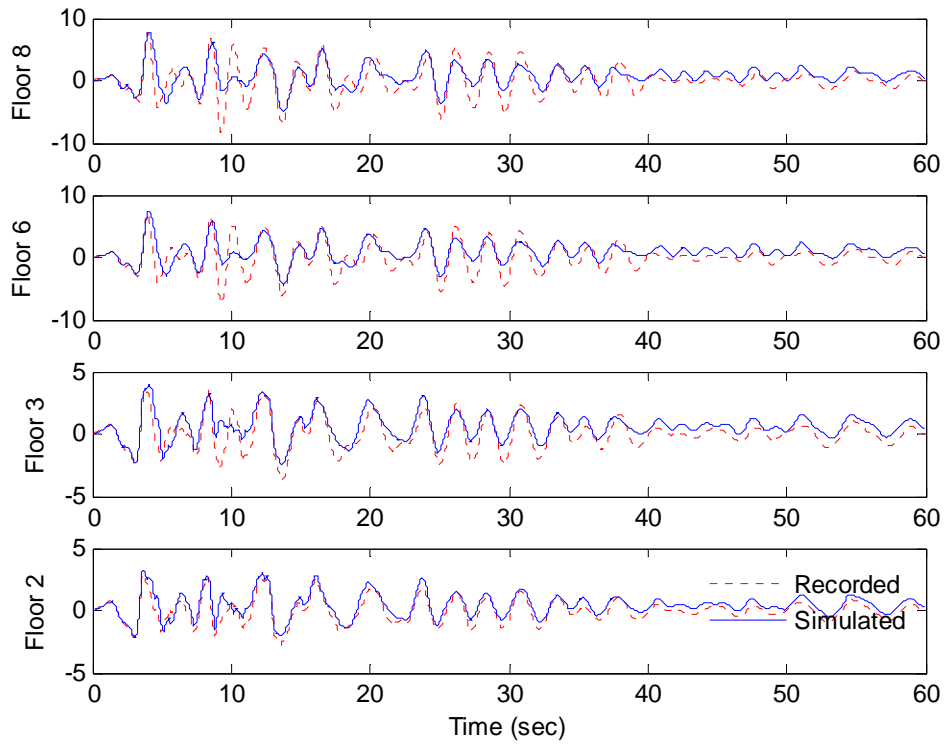
Figure 7 Total floor displacement in longitudinal direction. (Channel 12, 11, 10, and 9) (3D model)
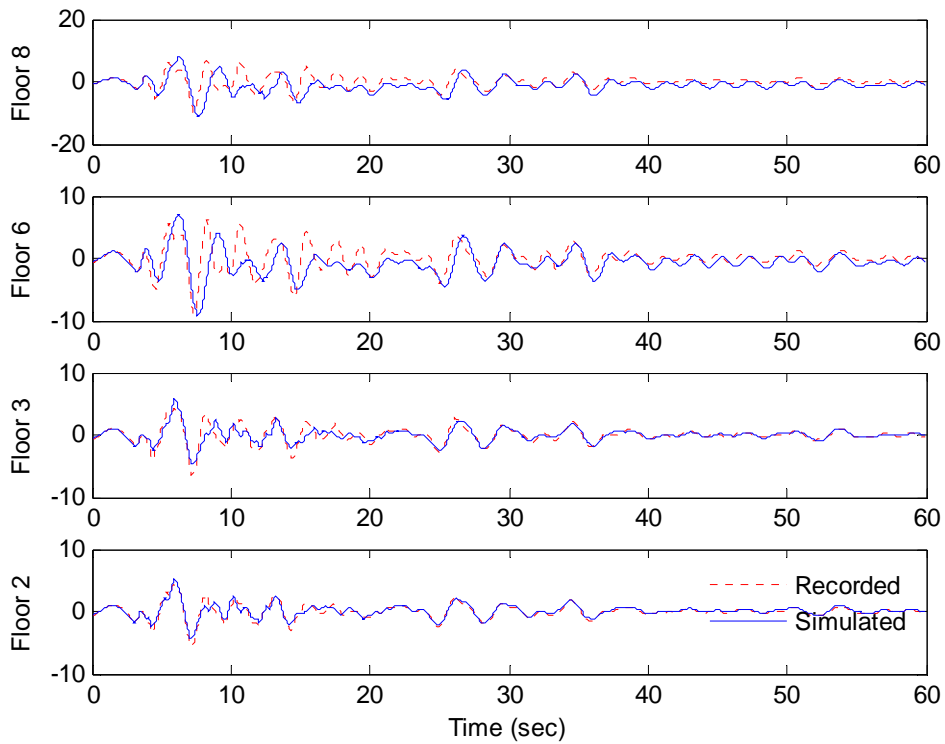
Figure 8 Total floor displacement in transverse direction. (Channel 8, 6, 4, and 3) (3D model)
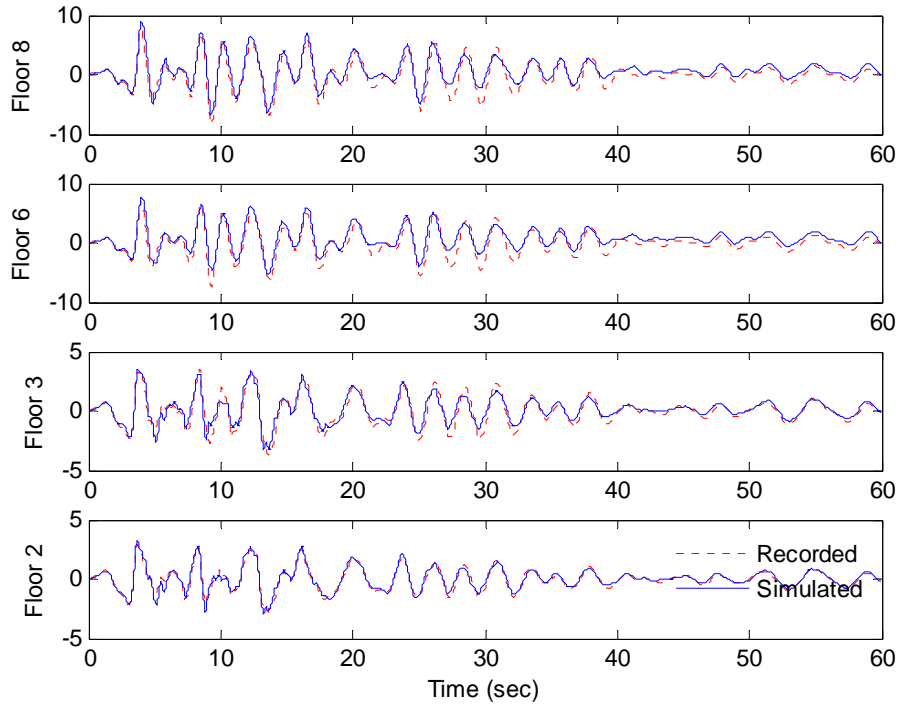
Figure 9 Total floor displacement in longitudinal direction. (Channel 12, 11, 10, and 9) (2D Model)
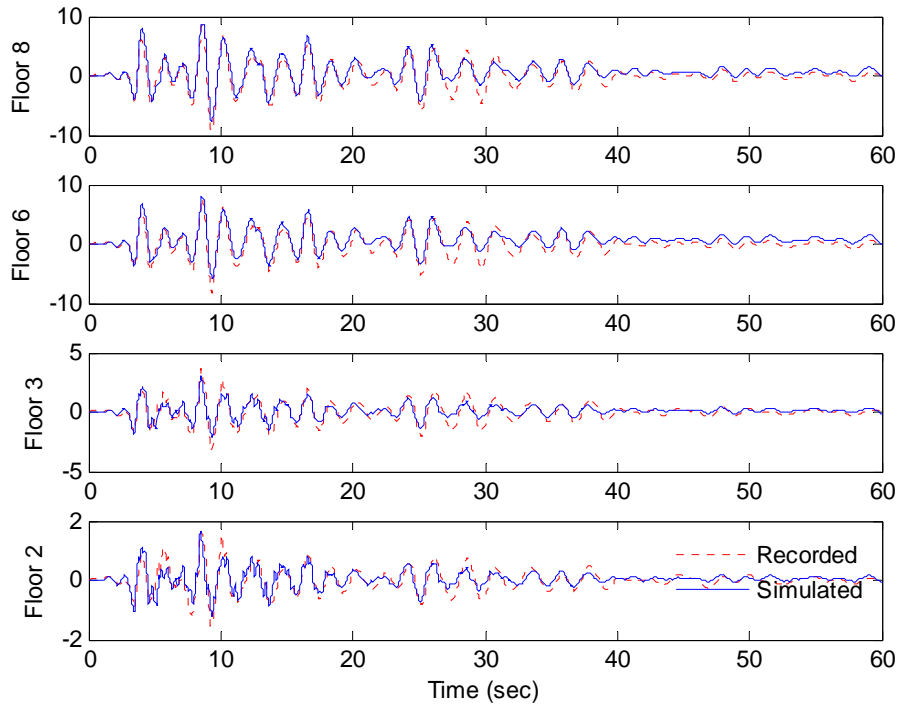
Figure 10 Relative floor displacement in longitudinal direction. (Channel 12, 11, 10, and 9) (2D Model)

11
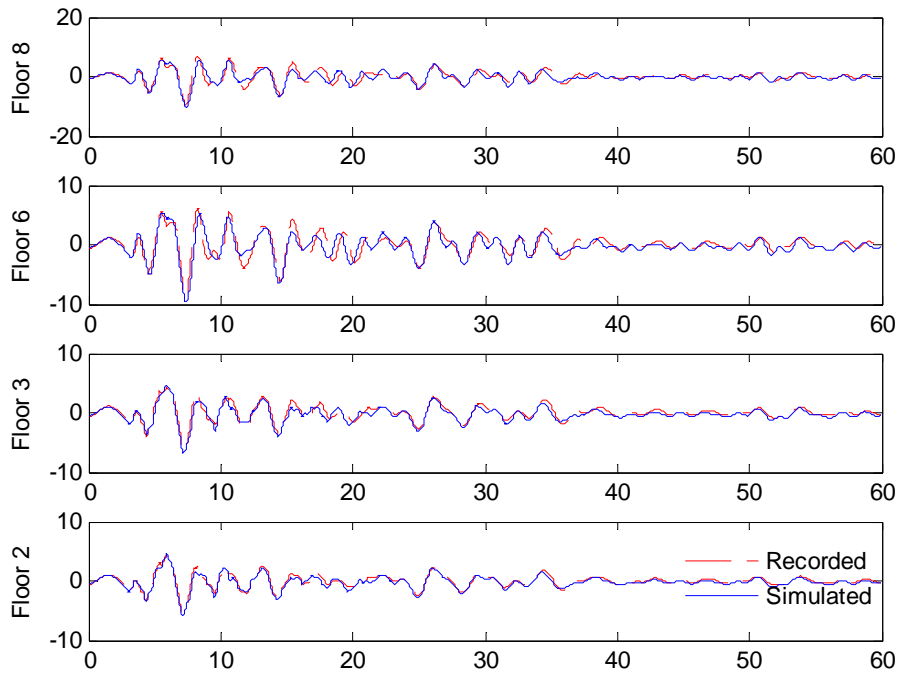
**Figure 11** Total floor displacement in transverse direction. (Channel 8, 6, 4, and 3) (2D Model)
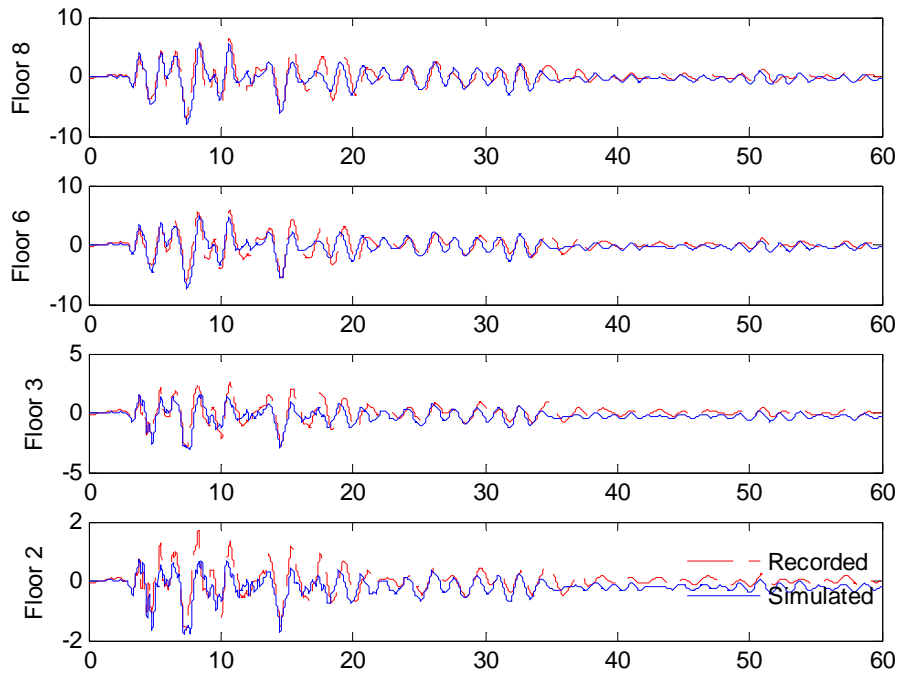
Figure 12. Relative floor displacement in transverse direction. (Channel 8, 6, 4, and 3) (2D Model)

T_{L1}=1.38s T_{T1}=1.25s
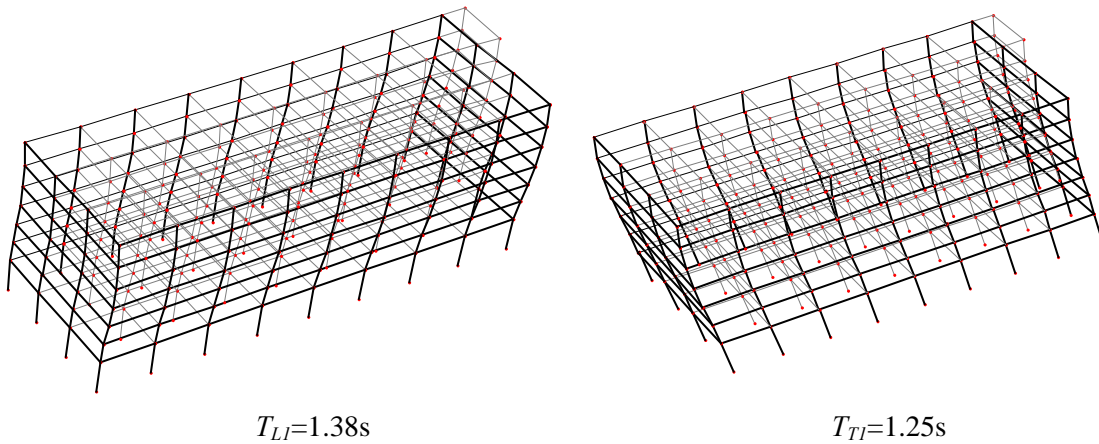
Figure 13 Modal shapes corresponding to the first mode in longitudinal direction (left) and first mode in transverse direction (right).

2.2 Description of the Ground Motion Database

One hundred pairs of horizontal strong ground motion recordings from 24 mostly shallow crustal earthquakes that occurred in California and worldwide from 1971 (San Fernando earthquake) to 2004 (Parkfield earthquake) were used as input to the nonlinear dynamic analyses of the reinforced concrete building discussed in the previous subsection. The moment magnitude, M, of these earthquakes ranges from 5.7 (1979 Coyote Lake earthquake) to 7.9 (2002 Denali earthquake) and the site-to-rupture closest distance, R, varies from 0.07km to 32.1km with an average value of about 8km (Figure 14). Some of these accelerograms can be configured as being pulse-like "near-source" records while others are more "ordinary" records. Some summary statistics of the PGA values of this ensemble of accelerograms are listed in Table 1 while the PGA histograms are shown in Figure 15. Table 2a to Table 2e list the characteristics of each record in this database. These 100 pairs of horizontal components have been used both in the orientation as originally recorded (Columns 6 and 7) and also rotated according to the fault-normal (FN) and fault-parallel (FP) directions of the causative fault (Columns 8 and 9). The database of ground motions recently compiled within the PEER-funded Next Generation Attenuation (NGA) Relationships Project (http://peer.berkeley.edu/research/funded_projects_1/project_1L11.html) and the database of the California Strong Motion Instrumentation Program (CSMIP) (http://www.consrv.ca.gov/CGS/smip/index.htm) of the California Geological Survey were the two data sources for these records, as specified in the last column of the table.

It is important to emphasize that this large number of ground motions is necessary only to statistically validate the findings of this study. A significantly smaller database will be sufficient in most practical applications.

13
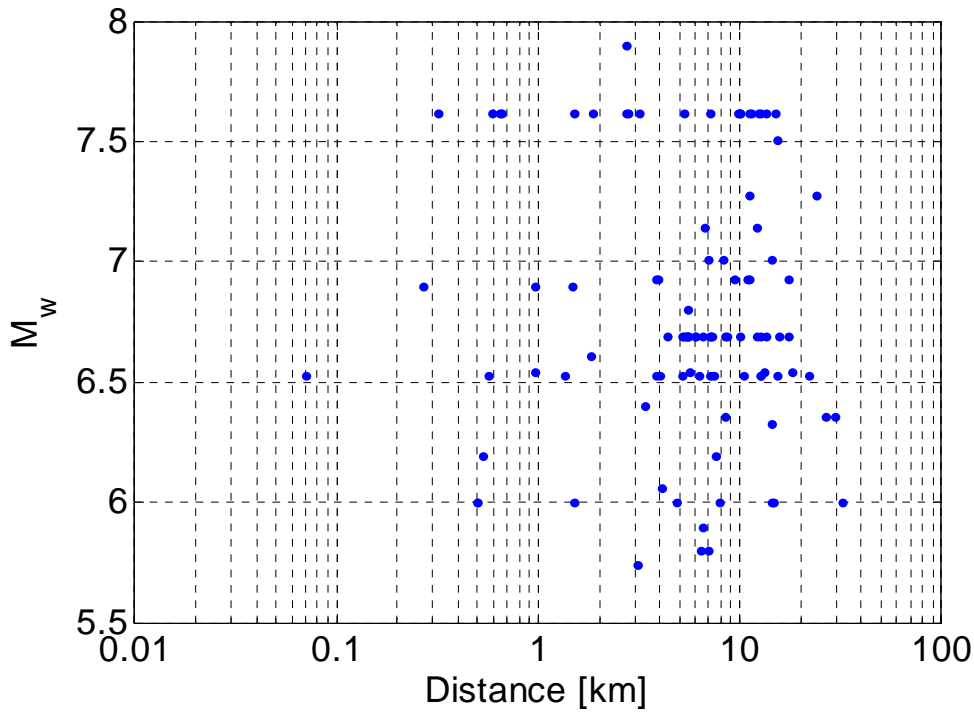
Figure 14 Magnitude-Distance scattergram for the 100 records considered in this study.
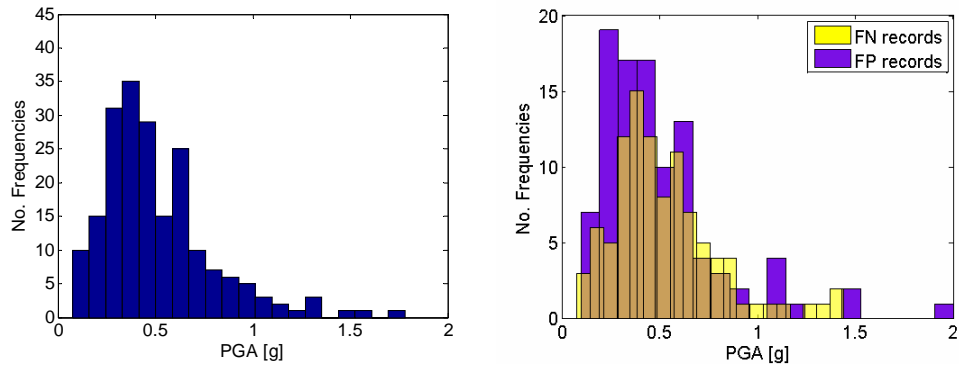
Figure 15 Histograms of PGA (g) for the horizontal components as recorded and rotated in the fault-normal and fault-parallel directions.

	Min	Max	Avg	Median
Recorded	0.07	1.78	0.51	0.44
Rotated FP	0.10	2.00	0.49	0.41
Rotated FN	0.08	1.43	0.52	0.46

Table 1. Summary statistics of the PGA values (g) of the accelerograms used in this study. The first row refers to the components as recorded while the second and the third refer to the components rotated in the fault parallel and fault normal conditions.

Earthquake	Station Name	Date	Mw	Distance (km)	Direction	PGA (g)	RandHorFile Name	PGA (g)	Data Source
Cape Mendocino	Cape Mendocino	25-Apr-92	7.01	6.96	FN	1.269	CPM000	1.497	NGA
Cape Mendocino	Cape Mendocino	25-Apr-92	7.01	6.96	FP	1.431	CPM090	1.039	NGA
Cape Mendocino	Petrolia	25-Apr-92	7.01	8.18	FN	0.615	PET000	0.590	NGA
Cape Mendocino	Petrolia	25-Apr-92	7.01	8.18	FP	0.630	PET090	0.662	NGA
Cape Mendocino	Rio Dell Overpass - FF	25-Apr-92	7.01	14.33	FN	0.416	RIO270	0.385	NGA
Cape Mendocino	Rio Dell Overpass - FF	25-Apr-92	7.01	14.33	FP	0.541	RIO360	0.549	NGA
Parkfield	FAULT ZONE 12	28-Sep-04	6.00	1.5	chan1	0.379	CE36138_chan1	0.276	CSMIP
Parkfield	FAULT ZONE 12	28-Sep-04	6.00	1.5	chan2	0.209	CE36138_chan2	0.303	CSMIP
Parkfield	CHOLAME 2 WEST	28-Sep-04	6.00	14.3	chan1	0.584	CE36228_chan1	0.604	CSMIP
Parkfield	CHOLAME 2 WEST	28-Sep-04	6.00	14.3	chan2	0.420	CE36228_chan2	0.369	CSMIP
Parkfield	FAULT ZONE 1	28-Sep-04	6.00	4.8	chan1	0.579	CE36407_chan1	0.592	CSMIP
Parkfield	FAULT ZONE 1	28-Sep-04	6.00	4.8	chan2	0.692	CE36407_chan2	0.819	CSMIP
Parkfield	CHOLAME 3 WEST	28-Sep-04	6.00	14.5	chan1	0.534	CE36410_chan1	0.320	CSMIP
Parkfield	CHOLAME 3 WEST	28-Sep-04	6.00	14.5	chan2	0.305	CE36410_chan2	0.565	CSMIP
Parkfield	FAULT ZONE 15	28-Sep-04	6.00	0.5	chan1	0.239	CE36445_chan1	0.141	CSMIP
Parkfield	FAULT ZONE 15	28-Sep-04	6.00	0.5	chan2	0.174	CE36445_chan2	0.229	CSMIP
Parkfield	CHOLAME 1 EAST	28-Sep-04	6.00	7.9	chan1	0.439	CE36452_chan1	0.426	CSMIP
Parkfield	CHOLAME 1 EAST	28-Sep-04	6.00	7.9	chan2	0.326	CE36452_chan2	0.343	CSMIP
Parkfield	FAULT ZONE 14	28-Sep-04	6.00	0.5	chan1	0.820	CE36456_chan1	1.311	CSMIP
Parkfield	FAULT ZONE 14	28-Sep-04	6.00	0.5	chan2	1.131	CE36456_chan2	0.538	CSMIP
Parkfield	COALINGA - SLACK CANYON, HIDDEN VALLEY RANCH	28-Sep-04	6.00	32.1	chan1	0.348	CE46175_chan1	0.211	CSMIP
Parkfield	COALINGA - SLACK CANYON, HIDDEN VALLEY RANCH	28-Sep-04	6.00	32.1	chan2	0.220	CE46175_chan2	0.347	CSMIP
Chalfant Valley-02	Zack Brothers Ranch	21-Jul-86	6.19	7.58	FN	0.383	C-ZAK270	0.143	NGA
Chalfant Valley-02	Zack Brothers Ranch	21-Jul-86	6.19	7.58	FP	0.413	C-ZAK360	0.108	NGA
Chi-Chi, Taiwan	CHY006	20-Sep-99	7.62	9.77	FN	0.311	CHY006-N	0.345	NGA
Chi-Chi, Taiwan	CHY006	20-Sep-99	7.62	9.77	FP	0.374	CHY006-W	0.364	NGA
Chi-Chi, Taiwan	CHY028	20-Sep-99	7.62	3.14	FN	0.663	CHY028-E	0.653	NGA
Chi-Chi, Taiwan	CHY028	20-Sep-99	7.62	3.14	FP	0.887	CHY028-N	0.821	NGA
Chi-Chi, Taiwan	CHY034	20-Sep-99	7.62	14.82	FN	0.291	CHY034-N	0.310	NGA
Chi-Chi, Taiwan	CHY034	20-Sep-99	7.62	14.82	FP	0.336	CHY034-W	0.248	NGA
Chi-Chi, Taiwan	CHY035	20-Sep-99	7.62	12.65	FN	0.261	CHY035-E	0.252	NGA
Chi-Chi, Taiwan	CHY035	20-Sep-99	7.62	12.65	FP	0.279	CHY035-N	0.246	NGA
Chi-Chi, Taiwan	CHY080	20-Sep-99	7.62	2.69	FN	0.624	CHY080-E	0.968	NGA
Chi-Chi, Taiwan	CHY080	20-Sep-99	7.62	2.69	FP	1.160	CHY080-N	0.902	NGA
Chi-Chi, Taiwan	CHY101	20-Sep-99	7.62	9.96	FN	0.451	CHY101-E	0.353	NGA
Chi-Chi, Taiwan	CHY101	20-Sep-99	7.62	9.96	FP	0.379	CHY101-N	0.440	NGA
Chi-Chi, Taiwan	TCU052	20-Sep-99	7.62	0.66	FN	0.390	TCU052-E	0.348	NGA
Chi-Chi, Taiwan	TCU052	20-Sep-99	7.62	0.66	FP	0.376	TCU052-N	0.419	NGA
Chi-Chi, Taiwan	TCU065	20-Sep-99	7.62	0.59	FN	0.822	TCU065-E	0.814	NGA
Chi-Chi, Taiwan	TCU065	20-Sep-99	7.62	0.59	FP	0.585	TCU065-N	0.603	NGA

Table 2a. Database of horizontal component ground motions used in this study. The PGA values in Column 9 refer to the accelerograms as recorded and those in Column 7 refer to the records rotated according to the fault strike direction. Legend: NGA = Next Generation of Attenuation Equations project; CSMIP: California Strong Motion Instrumentation Program.

Earthquake	Station Name	Date	Mw	Distance (km)	Direction	PGA (g)	RandHorFile Name	PGA (g) Random Hor	Data Source
Chi-Chi, Taiwan	TCU067	20-Sep-99	7.62	0.64	FN	0.558	TCU067-E	0.503	NGA
Chi-Chi, Taiwan	TCU067	20-Sep-99	7.62	0.64	FP	0.312	TCU067-N	0.325	NGA
Chi-Chi, Taiwan	TCU068	20-Sep-99	7.62	0.32	FN	0.562	TCU068-E	0.566	NGA
Chi-Chi, Taiwan	TCU068	20-Sep-99	7.62	0.32	FP	0.397	TCU068-N	0.462	NGA
Chi-Chi, Taiwan	TCU071	20-Sep-99	7.62	5.31	FN	0.566	TCU071-E	0.567	NGA
Chi-Chi, Taiwan	TCU071	20-Sep-99	7.62	5.31	FP	0.660	TCU071-N	0.655	NGA
Chi-Chi, Taiwan	TCU072	20-Sep-99	7.62	7.03	FN	0.488	TCU072-E	0.489	NGA
Chi-Chi, Taiwan	TCU072	20-Sep-99	7.62	7.03	FP	0.393	TCU072-N	0.400	NGA
Chi-Chi, Taiwan	TCU074	20-Sep-99	7.62	13.46	FN	0.616	TCU074-E	0.597	NGA
Chi-Chi, Taiwan	TCU074	20-Sep-99	7.62	13.46	FP	0.315	TCU074-N	0.349	NGA
Chi-Chi, Taiwan	TCU076	20-Sep-99	7.62	2.76	FN	0.305	TCU076-E	0.303	NGA
Chi-Chi, Taiwan	TCU076	20-Sep-99	7.62	2.76	FP	0.417	TCU076-N	0.416	NGA
Chi-Chi, Taiwan	TCU079	20-Sep-99	7.62	10.97	FN	0.733	TCU079-E	0.743	NGA
Chi-Chi, Taiwan	TCU079	20-Sep-99	7.62	10.97	FP	0.393	TCU079-N	0.393	NGA
Chi-Chi, Taiwan	TCU084	20-Sep-99	7.62	11.24	FN	1.157	TCU084-E	1.157	NGA
Chi-Chi, Taiwan	TCU084	20-Sep-99	7.62	11.24	FP	0.420	TCU084-N	0.417	NGA
Chi-Chi, Taiwan	TCU102	20-Sep-99	7.62	1.51	FN	0.293	TCU102-E	0.298	NGA
Chi-Chi, Taiwan	TCU102	20-Sep-99	7.62	1.51	FP	0.168	TCU102-N	0.169	NGA
Chi-Chi, Taiwan	TCU116	20-Sep-99	7.62	12.4	FN	0.184	TCU116-E	0.184	NGA
Chi-Chi, Taiwan	TCU116	20-Sep-99	7.62	12.4	FP	0.147	TCU116-N	0.148	NGA
Chi-Chi, Taiwan	TCU129	20-Sep-99	7.62	1.84	FN	1.013	TCU129-E	1.010	NGA
Chi-Chi, Taiwan	TCU129	20-Sep-99	7.62	1.84	FP	0.642	TCU129-N	0.634	NGA
Chi-Chi, Taiwan	WGK	20-Sep-99	7.62	9.96	FN	0.290	WGK-E	0.334	NGA
Chi-Chi, Taiwan	WGK	20-Sep-99	7.62	9.96	FP	0.497	WGK-N	0.484	NGA
Coalinga-01	Parkfield - Vineyard Cany 1E	02-May-83	6.36	26.38	FN	0.158	H-PV1000	0.167	NGA
Coalinga-01	Parkfield - Vineyard Cany 1E	02-May-83	6.36	26.38	FP	0.173	H-PV1090	0.230	NGA
Coalinga-01	Pleasant Valley P.P. - bldg	02-May-83	6.36	8.41	FN	0.377	H-PVB045	0.380	NGA
Coalinga-01	Pleasant Valley P.P. - bldg	02-May-83	6.36	8.41	FP	0.284	H-PVB135	0.285	NGA
Coalinga-01	Pleasant Valley P.P. - yard	02-May-83	6.36	8.41	FN	0.590	H-PVY045	0.592	NGA
Coalinga-01	Pleasant Valley P.P. - yard	02-May-83	6.36	8.41	FP	0.547	H-PVY135	0.551	NGA
Coalinga-01	Parkfield - Fault Zone 14	02-May-83	6.36	29.48	FN	0.245	H-Z14000	0.282	NGA
Coalinga-01	Parkfield - Fault Zone 14	02-May-83	6.36	29.48	FP	0.263	H-Z14090	0.274	NGA
Coyote Lake	Gilroy Array #6	06-Aug-79	5.74	3.11	FN	0.452	G06230	0.434	NGA
Coyote Lake	Gilroy Array #6	06-Aug-79	5.74	3.11	FP	0.333	G06320	0.316	NGA
Denali, Alaska	TAPS Pump Station #10	03-Nov-02	7.90	2.74	FN	0.335	ps10047	0.319	NGA
Denali, Alaska	TAPS Pump Station #10	03-Nov-02	7.90	2.74	FP	0.284	ps10317	0.318	NGA
Dinar, Turkey	Dinar	01-Oct-95	6.40	3.36	FN	0.324	DIN090	0.352	NGA
Dinar, Turkey	Dinar	01-Oct-95	6.40	3.36	FP	0.285	DIN180	0.282	NGA
Duzce, Turkey	Bolu	12-Nov-99	7.14	12.04	FN	0.782	BOL000	0.728	NGA
Duzce, Turkey	Bolu	12-Nov-99	7.14	12.04	FP	0.779	BOL090	0.822	NGA

Table 2b. Database of horizontal component ground motions used in this study. The PGA values in Column 9 refer to the accelerograms as recorded and those in Column 7 refer to the records rotated according to the fault strike direction. Legend: NGA = Next Generation of Attenuation Equations project; CSMIP: California Strong Motion Instrumentation Program.

Earthquake	Station Name	Date	Mw	Distance (km)	Direction	PGA (g)	RandHorFile Name	PGA (g) Random Hor	Data Source
Duzce, Turkey	Duzce	12-Nov-99	7.14	6.58	FN	0.358	DZC180	0.312	NGA
Duzce, Turkey	Duzce	12-Nov-99	7.14	6.58	FP	0.518	DZC270	0.358	NGA
Erzican, Turkey	Erzincan	13-Mar-92	6.69	4.38	FN	0.486	ERZ-NS	0.515	NGA
Erzican, Turkey	Erzincan	13-Mar-92	6.69	4.38	FP	0.420	ERZ-EW	0.496	NGA
Gazli, USSR	Karakyr	17-May-76	6.80	5.46	FN	0.600	GAZ000	0.608	NGA
Gazli, USSR	Karakyr	17-May-76	6.80	5.46	FP	0.710	GAZ090	0.718	NGA
Imperial Valley-06	Brawley Airport	15-Oct-79	6.53	10.42	FN	0.158	H-BRA225	0.160	NGA
Imperial Valley-06	Brawley Airport	15-Oct-79	6.53	10.42	FP	0.210	H-BRA315	0.220	NGA
Imperial Valley-06	El Centro Array #1	15-Oct-79	6.53	21.68	FN	0.138	H-E01140	0.139	NGA
Imperial Valley-06	El Centro Array #1	15-Oct-79	6.53	21.68	FP	0.137	H-E01230	0.134	NGA
Imperial Valley-06	El Centro Array #4	15-Oct-79	6.53	7.05	FN	0.357	H-E04140	0.485	NGA
Imperial Valley-06	El Centro Array #4	15-Oct-79	6.53	7.05	FP	0.475	H-E04230	0.360	NGA
Imperial Valley-06	El Centro Array #5	15-Oct-79	6.53	3.95	FN	0.375	H-E05140	0.519	NGA
Imperial Valley-06	El Centro Array #5	15-Oct-79	6.53	3.95	FP	0.527	H-E05230	0.379	NGA
Imperial Valley-06	El Centro Array #6	15-Oct-79	6.53	1.35	FN	0.442	H-E06140	0.410	NGA
Imperial Valley-06	El Centro Array #6	15-Oct-79	6.53	1.35	FP	0.400	H-E06230	0.439	NGA
Imperial Valley-06	El Centro Array #7	15-Oct-79	6.53	0.56	FN	0.462	H-E07140	0.338	NGA
Imperial Valley-06	El Centro Array #7	15-Oct-79	6.53	0.56	FP	0.335	H-E07230	0.463	NGA
Imperial Valley-06	El Centro Array #8	15-Oct-79	6.53	3.86	FN	0.468	H-E08140	0.602	NGA
Imperial Valley-06	El Centro Array #8	15-Oct-79	6.53	3.86	FP	0.590	H-E08230	0.454	NGA
Imperial Valley-06	El Centro Array #10	15-Oct-79	6.53	6.17	FN	0.176	H-E10050	0.171	NGA
Imperial Valley-06	El Centro Array #10	15-Oct-79	6.53	6.17	FP	0.227	H-E10320	0.224	NGA
Imperial Valley-06	El Centro Array #11	15-Oct-79	6.53	12.45	FN	0.370	H-E11140	0.364	NGA
Imperial Valley-06	El Centro Array #11	15-Oct-79	6.53	12.45	FP	0.379	H-E11230	0.380	NGA
Imperial Valley-06	EC County Center FF	15-Oct-79	6.53	7.31	FN	0.180	H-ECC002	0.213	NGA
Imperial Valley-06	EC County Center FF	15-Oct-79	6.53	7.31	FP	0.222	H-ECC092	0.235	NGA
Imperial Valley-06	El Centro Differential Array	15-Oct-79	6.53	5.09	FN	0.417	H-EDA270	0.352	NGA
Imperial Valley-06	El Centro Differential Array	15-Oct-79	6.53	5.09	FP	0.444	H-EDA360	0.480	NGA
Imperial Valley-06	EC Meloland Overpass FF	15-Oct-79	6.53	0.07	FN	0.378	H-EMO000	0.314	NGA
Imperial Valley-06	EC Meloland Overpass FF	15-Oct-79	6.53	0.07	FP	0.266	H-EMO270	0.296	NGA
Imperial Valley-06	Parachute Test Site	15-Oct-79	6.53	12.69	FN	0.135	H-PTS225	0.111	NGA
Imperial Valley-06	Parachute Test Site	15-Oct-79	6.53	12.69	FP	0.190	H-PTS315	0.204	NGA
Imperial Valley-06	Westmorland Fire Sta	15-Oct-79	6.53	15.25	FN	0.077	H-WSM090	0.074	NGA
Imperial Valley-06	Westmorland Fire Sta	15-Oct-79	6.53	15.25	FP	0.098	H-WSM180	0.110	NGA
Kobe, Japan	KJMA	16-Jan-95	6.90	0.96	FN	0.854	KJM000	0.821	NGA
Kobe, Japan	KJMA	16-Jan-95	6.90	0.96	FP	0.548	KJM090	0.599	NGA
Kobe, Japan	Takatori	16-Jan-95	6.90	1.47	FN	0.682	TAK000	0.611	NGA
Kobe, Japan	Takatori	16-Jan-95	6.90	1.47	FP	0.605	TAK090	0.616	NGA
Kobe, Japan	Takarazuka	16-Jan-95	6.90	0.27	FN	0.645	TAZ000	0.693	NGA
Kobe, Japan	Takarazuka	16-Jan-95	6.90	0.27	FP	0.697	TAZ090	0.694	NGA

Table 2c. Database of horizontal component ground motions used in this study. The PGA values in Column 9 refer to the accelerograms as recorded and those in Column 7 refer to the records rotated according to the fault strike direction. Legend: NGA = Next Generation of Attenuation Equations project; CSMIP: California Strong Motion Instrumentation Program.

Earthquake	Station Name	Date	Mw	Distance (km)	Direction	PGA (g)	RandHorFile Name	PGA (g) Random Hor	Data Source
Kocaeli, Turkey	Duzce	17-Aug-99	7.51	15.37	FN	0.283	DZC180	0.312	NGA
Kocaeli, Turkey	Duzce	17-Aug-99	7.51	15.37	FP	0.375	DZC270	0.358	NGA
Landers	Joshua Tree	28-Jun-92	7.28	11.03	FN	0.288	JOS000	0.274	NGA
Landers	Joshua Tree	28-Jun-92	7.28	11.03	FP	0.267	JOS090	0.284	NGA
Landers	Yermo Fire Station	28-Jun-92	7.28	23.62	FN	0.222	YER270	0.245	NGA
Landers	Yermo Fire Station	28-Jun-92	7.28	23.62	FP	0.222	YER360	0.152	NGA
Loma Prieta	BRAN	18-Oct-89	6.93	10.72	FN	0.637	BRN000	0.481	NGA
Loma Prieta	BRAN	18-Oct-89	6.93	10.72	FP	0.413	BRN090	0.526	NGA
Loma Prieta	Corralitos	18-Oct-89	6.93	3.85	FN	0.484	CLS000	0.644	NGA
Loma Prieta	Corralitos	18-Oct-89	6.93	3.85	FP	0.514	CLS090	0.479	NGA
Loma Prieta	Gilroy Array #2	18-Oct-89	6.93	11.07	FN	0.406	G02000	0.367	NGA
Loma Prieta	Gilroy Array #2	18-Oct-89	6.93	11.07	FP	0.303	G02090	0.322	NGA
Loma Prieta	LGPC	18-Oct-89	6.93	3.88	FN	0.944	LGP000	0.966	NGA
Loma Prieta	LGPC	18-Oct-89	6.93	3.88	FP	0.537	LGP090	0.587	NGA
Loma Prieta	WAHO	18-Oct-89	6.93	17.47	FN	0.509	WAH000	0.398	NGA
Loma Prieta	WAHO	18-Oct-89	6.93	17.47	FP	0.615	WAH090	0.672	NGA
Loma Prieta	Saratoga - W Valley Coll.	18-Oct-89	6.93	9.31	FN	0.403	WVC000	0.255	NGA
Loma Prieta	Saratoga - W Valley Coll.	18-Oct-89	6.93	9.31	FP	0.256	WVC270	0.332	NGA
Morgan Hill	Coyote Lake Dam (SW Abut)	24-Apr-84	6.19	0.53	FN	0.814	CYC195	0.711	NGA
Morgan Hill	Coyote Lake Dam (SW Abut)	24-Apr-84	6.19	0.53	FP	1.080	CYC285	1.298	NGA
Northridge-01	LA - Sepulveda VA Hospital	17-Jan-94	6.69	8.44	FN	0.731	0637-270	0.749	NGA
Northridge-01	LA - Sepulveda VA Hospital	17-Jan-94	6.69	8.44	FP	0.707	0637-360	0.934	NGA
Northridge-01	Jensen Filter Plant Generator	17-Jan-94	6.69	5.43	FN	0.518	0655-022	0.571	NGA
Northridge-01	Jensen Filter Plant Generator	17-Jan-94	6.69	5.43	FP	1.067	0655-292	1.024	NGA
Northridge-01	Arleta - Nordhoff Fire Sta	17-Jan-94	6.69	8.66	FN	0.237	ARL090	0.344	NGA
Northridge-01	Arleta - Nordhoff Fire Sta	17-Jan-94	6.69	8.66	FP	0.332	ARL360	0.308	NGA
Northridge-01	Jensen Filter Plant	17-Jan-94	6.69	5.43	FN	0.518	JEN022	0.571	NGA
Northridge-01	Jensen Filter Plant	17-Jan-94	6.69	5.43	FP	1.068	JEN292	1.024	NGA
Northridge-01	Simi Valley - Katherine Rd	17-Jan-94	6.69	13.42	FN	1.066	KAT000	0.877	NGA
Northridge-01	Simi Valley - Katherine Rd	17-Jan-94	6.69	13.42	FP	0.614	KAT090	0.640	NGA
Northridge-01	LA Dam	17-Jan-94	6.69	5.92	FN	0.576	LDM064	0.511	NGA
Northridge-01	LA Dam	17-Jan-94	6.69	5.92	FP	0.415	LDM334	0.349	NGA
Northridge-01	Canyon Country - W Lost Cany	17-Jan-94	6.69	12.44	FN	0.466	LOS000	0.410	NGA
Northridge-01	Canyon Country - W Lost Cany	17-Jan-94	6.69	12.44	FP	0.337	LOS270	0.482	NGA
Northridge-01	Beverly Hills - 14145 Mulhol	17-Jan-94	6.69	17.15	FN	0.379	MUL009	0.416	NGA
Northridge-01	Beverly Hills - 14145 Mulhol	17-Jan-94	6.69	17.15	FP	0.502	MUL279	0.516	NGA
Northridge-01	Newhall - Fire Sta	17-Jan-94	6.69	5.92	FN	0.724	NWH090	0.583	NGA
Northridge-01	Newhall - Fire Sta	17-Jan-94	6.69	5.92	FP	0.651	NWH360	0.590	NGA
Northridge-01	Pacoima Dam (downstr)	17-Jan-94	6.69	7.01	FN	0.499	PAC175	0.415	NGA
Northridge-01	Pacoima Dam (downstr)	17-Jan-94	6.69	7.01	FP	0.245	PAC265	0.434	NGA

Table 2d. Database of horizontal component ground motions used in this study. The PGA values in Column 9 refer to the accelerograms as recorded and those in Column 7 refer to the records rotated according to the fault strike direction. Legend: NGA = Next Generation of Attenuation Equations project; CSMIP: California Strong Motion Instrumentation Program.

Earthquake	Station Name	Date	Mw	Distance (km)	Direction	PGA (g)	RandHorFile Name	PGA (g) Random Hor	Data Source
Northridge-01	Pacoima Kagel Canyon	17-Jan-94	6.69	7.26	FN	0.526	PKC090	0.301	NGA
Northridge-01	Pacoima Kagel Canyon	17-Jan-94	6.69	7.26	FP	0.236	PKC360	0.433	NGA
Northridge-01	Pacoima Dam (upper left)	17-Jan-94	6.69	7.01	FN	1.376	PUL104	1.585	NGA
Northridge-01	Pacoima Dam (upper left)	17-Jan-94	6.69	7.01	FP	1.465	PUL194	1.285	NGA
Northridge-01	Sun Valley - Roscoe Blvd	17-Jan-94	6.69	10.05	FN	0.298	RO3000	0.303	NGA
Northridge-01	Sun Valley - Roscoe Blvd	17-Jan-94	6.69	10.05	FP	0.394	RO3090	0.444	NGA
Northridge-01	Rinaldi Receiving Sta	17-Jan-94	6.69	6.5	FN	0.870	RRS228	0.825	NGA
Northridge-01	Rinaldi Receiving Sta	17-Jan-94	6.69	6.5	FP	0.424	RRS318	0.487	NGA
Northridge-01	Sylmar - Converter Sta East	17-Jan-94	6.69	5.19	FN	0.839	SCE018	0.828	NGA
Northridge-01	Sylmar - Converter Sta East	17-Jan-94	6.69	5.19	FP	0.495	SCE288	0.493	NGA
Northridge-01	Sylmar - Converter Sta	17-Jan-94	6.69	5.35	FN	0.594	SCS052	0.612	NGA
Northridge-01	Sylmar - Converter Sta	17-Jan-94	6.69	5.35	FP	0.795	SCS142	0.897	NGA
Northridge-01	Northridge - 17645 Saticoy St	17-Jan-94	6.69	12.09	FN	0.413	STC090	0.368	NGA
Northridge-01	Northridge - 17645 Saticoy St	17-Jan-94	6.69	12.09	FP	0.422	STC180	0.477	NGA
Northridge-01	Sylmar - Olive View Med FF	17-Jan-94	6.69	5.3	FN	0.733	SYL090	0.604	NGA
Northridge-01	Sylmar - Olive View Med FF	17-Jan-94	6.69	5.3	FP	0.595	SYL360	0.843	NGA
Northridge-01	Tarzana - Cedar Hill A	17-Jan-94	6.69	15.6	FN	1.333	TAR090	1.779	NGA
Northridge-01	Tarzana - Cedar Hill A	17-Jan-94	6.69	15.6	FP	1.998	TAR360	0.990	NGA
Northridge-01	Newhall - W Pico Canyon Rd.	17-Jan-94	6.69	5.48	FN	0.426	WPI046	0.455	NGA
Northridge-01	Newhall - W Pico Canyon Rd.	17-Jan-94	6.69	5.48	FP	0.279	WPI316	0.325	NGA
N. Palm Springs	North Palm Springs	08-Jul-86	6.06	4.04	FN	0.670	NPS210	0.594	NGA
N. Palm Springs	North Palm Springs	08-Jul-86	6.06	4.04	FP	0.616	NPS300	0.694	NGA
San Salvador	Geotech Investig Center	10-Oct-86	5.80	6.3	FN	0.846	GIC090	0.875	NGA
San Salvador	Geotech Investig Center	10-Oct-86	5.80	6.3	FP	0.365	GIC180	0.475	NGA
San Salvador	National Geografical Inst	10-Oct-86	5.80	6.99	FN	0.421	NGI180	0.406	NGA
San Salvador	National Geografical Inst	10-Oct-86	5.80	6.99	FP	0.611	NGI270	0.612	NGA
San Fernando	Pacoima Dam (upper left abut)	09-Feb-71	6.61	1.81	FN	1.435	PUL164	1.226	NGA
San Fernando	Pacoima Dam (upper left abut)	09-Feb-71	6.61	1.81	FP	0.855	PUL254	1.160	NGA
Superstition Hills-02	El Centro Imp. Co. Cent	24-Nov-87	6.54	18.2	FN	0.308	B-ICC000	0.358	NGA
Superstition Hills-02	El Centro Imp. Co. Cent	24-Nov-87	6.54	18.2	FP	0.223	B-ICC090	0.258	NGA
Superstition Hills-02	Parachute Test Site	24-Nov-87	6.54	0.95	FN	0.419	B-PTS225	0.455	NGA
Superstition Hills-02	Parachute Test Site	24-Nov-87	6.54	0.95	FP	0.344	B-PTS315	0.377	NGA
Superstition Hills-02	Superstition Mtn Camera	24-Nov-87	6.54	5.61	FN	0.747	B-SUP045	0.682	NGA
Superstition Hills-02	Superstition Mtn Camera	24-Nov-87	6.54	5.61	FP	0.908	B-SUP135	0.894	NGA
Superstition Hills-02	Westmorland Fire Sta	24-Nov-87	6.54	13.03	FN	0.210	B-WSM090	0.172	NGA
Superstition Hills-02	Westmorland Fire Sta	24-Nov-87	6.54	13.03	FP	0.235	B-WSM180	0.211	NGA
Victoria, Mexico	Cerro Prieto	09-Jun-80	6.33	14.37	FN	0.628	CPE045	0.621	NGA
Victoria, Mexico	Cerro Prieto	09-Jun-80	6.33	14.37	FP	0.598	CPE315	0.587	NGA
Westmorland	Westmorland Fire Sta	26-Apr-81	5.90	6.5	FN	0.412	WSM090	0.368	NGA
Westmorland	Westmorland Fire Sta	26-Apr-81	5.90	6.5	FP	0.399	WSM180	0.496	NGA

Table 2e. Database of horizontal component ground motions used in this study. The PGA values in Column 9 refer to the accelerograms as recorded and those in Column 7 refer to the records rotated according to the fault strike direction. Legend: NGA = Next Generation of Attenuation Equations project; CSMIP: California Strong Motion Instrumentation Program.

2.3   *Methodology for prediction of building response*

In this study we estimate the response of the 7-story Van Nuys concrete building (Figure 1 to Figure 3) subject to multi-directional horizontal ground motions for the following 3 building orientations:

Orientation 1   Building longitudinal direction (8 bays) aligned with the fault-parallel (FP) direction of the ground shaking and transverse direction (3 bays) aligned with the fault normal FN direction of the ground shaking

Orientation 2   Building transverse direction aligned with the FP direction of the ground shaking and longitudinal direction aligned with the FN direction of the ground shaking

Orientation 3   Building oriented at an undefined angle with respect to the causative fault

Both 3D and 2D models were subject to the database of accelerograms described in the previous subsection and the building's dynamic response was monitored (see Section 3). In the Orientations 1 and 2 above the rotated horizontal components (Columns 6 and 7 in Table 2a to Table 2e) were used whereas in the Orientation 3 above we applied the accelerograms as recorded (Columns 8 and 9). The vertical component of a ground motion is rarely important for the response of ordinary buildings and it has not been utilized in this study.

The structure's response has been gauged by the maximum (across the height of the building) peak (in time) interstory drift ratio, δ_{max}. Note that in the 3D case δ_{max} is computed from the maximum displacement either along one of the axes or as a vector sum of the displacements along both axes. The definition applied in each case is clearly specified. Also, the value of the displacement entered in the δ_{max} computations is the average of those computed for the four corner columns. In the 2D frame cases the averaging is done for the first and last columns. δ_{max} was selected because in framed buildings it is a good indicator of the collapse capacity of the structure.

The quantity δ_{max} is then statistically estimated via conventional regression techniques using appropriate intensity parameters of the ground motion as predictor variables. For the purpose of this study the predictors were chosen as described below.

- The 5%-damped spectral accelerations at the first and second period of vibration of the building in the directions of the building principal axes. These four periods were called T_{L1}; T_{L2}; T_{T1}; and T_{T2} in Subsection 2.1. We have considered both the spectral acceleration, $S_a(T)$, of an arbitrary component (either randomly rotated – Orientation 3 – or rotated in relation to the direction of fault strike – Orientations 1 and 2) or of an "average" component, $S_a(T)_{gm}$. The latter is the geometric mean (i.e., the mean of the natural logarithms) of the spectral acceleration of both horizontal components at the same period, T. Recall that for the same scenario event, the median of the two quantities $S_a(T)$ and $S_a(T)_{gm}$ coincide but the uncertainty of the former is larger than that of the latter (Baker and Cornell (2006b). In addition, we have utilized, somewhat unconventionally, the geometric mean of the spectral acceleration at different periods and orientations of the recordings with respect to the strike of the causative fault and consider it as a single predictor of response (e.g., Stewart *et al.*, 2001). For example, we considered $S_a(T_{L1};T_{T1})_{gm}$ at the two periods, T_{L1} and T_{T1}, of the first mode of vibration in each of the direction of the principal axes of the building.

- The inelastic spectral displacement, $S_{di}(T)$, at the initial linear elastic first period of vibration of the building in either the longitudinal or the transverse direction. The value of S_{di} for each record in the database of Subsection 2.2 is determined from the peak response (over time) of a bilinear oscillator with 5% hardening stiffness and 5% damping

ratio with a hysteretic behavior such as that shown in Figure 16. The value of the yield displacement, d_y, of the oscillator that provided the largest reduction in response variability for a given $S_{di}(T)$ was selected for this study. The largest reduction in δ_{max} in the transverse direction for the 3D model is achieved for all those d_y–T pairs that form the depression in the surface in Figure 17. These pairs are depicted in blue in the figure. Similar figures omitted here were used to calibrate the selection of d_y for the 3D longitudinal direction response and for the response of the 2D frames. For the 3D model we chose a value of d_y equal to 1.6in for the longitudinal direction and of 1.14in for the transverse direction. The optimized d_y values are 2.20in for the longitudinal 2D frame and 1.72in for the 2D transverse frame. As shown by Tothong and Cornell (2006a) and Tothong and Luco (2007), this optimized d_y selection method is superior to the conventional one based on global pushover analysis results (Fajfar, 2000; Chopra 2001) especially when the structure experiences large deformations (i.e., when stiffness and strength degradation occurs after damage). Note that for simplicity we kept the value of T to be the same as the initial linear elastic period of the building of the first mode of vibration along each axis although a slightly larger reduction of dispersion could be achieved with different T values.
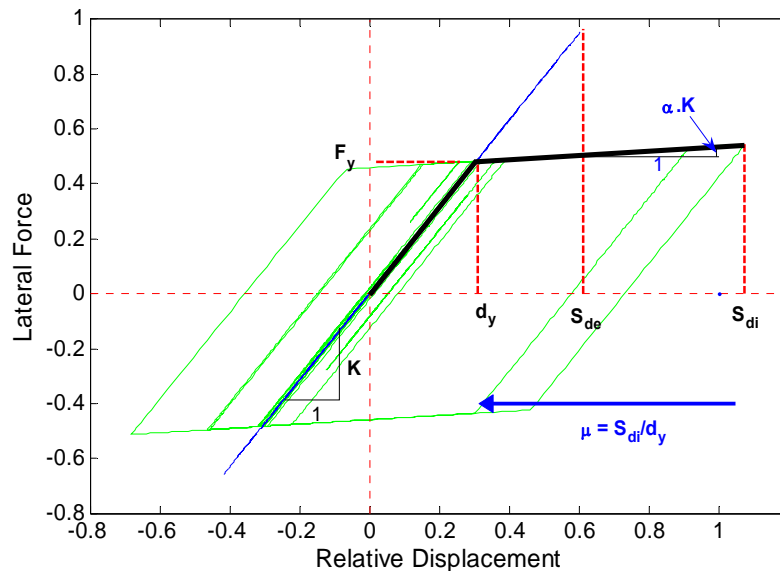
Figure 16 Backbone curve and hysteretic behavior of the bi-linear inelastic oscillator used in this study to determine the values of the predictor $S_{di}(T)$.
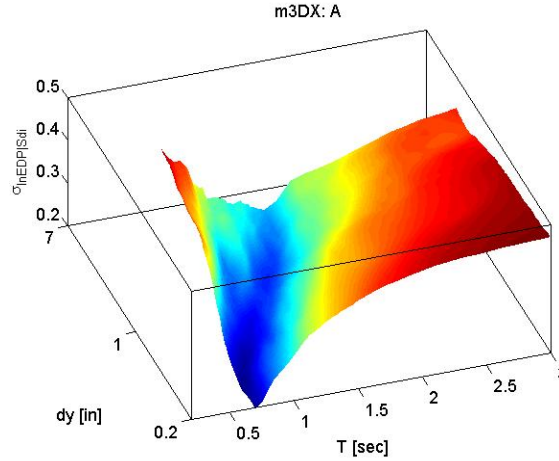
Figure 17 Values of the response dispersion from the 3D model given $S_{di}(T)$ for a range of d_y and T pairs. The largest reduction in dispersion is achieved for the d_y and T pairs shown in blue above.

In this study we have limited our attention to S_a's and S_{di}'s and we have neglected other IM's because, as described in the next subsection, S_a's and S_{di}'s will be used in the PSHA and VPSHA computations. For a scalar PSHA computation, a prediction equation for the parameter at hand given the basic variables of an earthquake event (e.g., M and R) is the only necessary item. Prediction equations are available for a multitude of parameters (e.g., Stewart *et al.*, 2001) including $S_{di}(T)$ (Tothong and Cornell, 2006b). However, for VPSHA the variance-covariance matrix, Σ, of the considered IM's is also needed. At this point in time, Σ is available for single-component S_a's at different periods and across orthogonal components of three-dimensional ground motions (Inoue, 1990; Baker and Cornell, 2006b). Strictly speaking, the variance-covariance matrix in the aforementioned studies was empirically developed for randomly oriented components (applied here to building Orientation 3) but it is applicable to fault-normal and fault-parallel rotated components as well (Baker, 2007) (used for building Orientations 1 and 2). In this project we have also developed a variance-covariance matrix for $S_{di}(T)$ limited to the values of T and d_y considered here. Σ is not yet available for any other ground motion parameters.

Finally, although our attention has been on spectral accelerations and inelastic spectral displacements, we have also considered whether the magnitude, M, of the causative event and the site-to-rupture distance, R, in addition to S_a and S_{di} may improve the accuracy of the response prediction.

2.4 Methodology for PSHA and VPSHA

A probabilistic seismic hazard analysis both in conventional scalar form and also, when appropriate, in vector form is performed for the building site. As mentioned earlier, to maximize the anisotropy of the seismic hazard the Van Nuys building has been assumed to be located downtown San Francisco at the following coordinates (Lat: 37.7905; Long: -122.3925). Hazard analyses were repeated for the orientations of the building specified in Orientations 1-3 and for the following IM's:

- $S_a(T_{L1})$ and $S_a(T_{T1})$, the spectral accelerations at the fundamental period of vibration of the building in the longitudinal and transverse directions, respectively, of an arbitrary horizontal component. We also consider, when appropriate, the geometric mean of these spectral accelerations computed from both horizontal components, (i.e., $S_a(T_{L1})_{gm}$, $S_a(T_{T1})_{gm}$, and $S_a(T_{L1};T_{T1})_{gm}$). Of course, if $T_{L1} \cong T_{T1}$ then $S_a(T_{L1})_{gm} \cong S_a(T_{T1})_{gm} \cong S_a(T_{L1};T_{T1})_{gm}$. These geometric means are considered because available ground motion prediction equations are typically

developed for the geometric mean of the two horizontal components rather than for the spectral accelerations of an arbitrary horizontal component.

- $S_{di}(T_{L1})$ and $S_{di}(T_{T1})$, the inelastic spectral displacement of an arbitrary horizontal component, and $S_{di}(T_{L1};T_{T1})_{gm}$, the geometric mean of S_{di} in two orthogonal directions for different period and values of yield displacements, d_y.

In all cases the scalar seismic hazard was computed using the PSHA code developed by Abrahamson (2002). The directivity effects on the site ground motion were explicitly modeled by considering multiple locations for the hypocenter within the rupture plane and by modifying the attenuation relationship of Abrahamson and Silva (1997) for stiff soil conditions according to Somerville *et al.* (1997). Note that, in line with Baker and Cornell (2006b), the PSHA code was modified to handle both single ground motion parameters that are measures of motion in different directions and at different periods (e.g., $S_a(T_{L1};T_{T1})_{gm}$ and $S_{di}(T_{L1};T_{T1})_{gm}$) and also the increase in variability of parameters related to an arbitrary component of motion (e.g., $S_a(T_{L1})$) rather than the more customary geometric mean of both horizontal components (e.g., $S_a(T_{L1})_{gm}$). Note that we did not compute the seismic hazard for any of the *IM*'s involving periods that correspond to the second mode of vibration in each direction (e.g., using the same notation above, $S_a(T_{L2})$, $S_a(T_{T2})$, $S_a(T_{L2})_{gm}$, $S_a(T_{T2})_{gm}$, $S_a(T_{L1};T_{L2})_{gm}$, $S_a(T_{T1};T_{T2})_{gm}$, $S_a(T_{L1};T_{L2},T_{T1};T_{T2})_{gm}$ and similarly for S_{di}'s). As shown in Chapter 3, for this 7-story building the additional reduction in response variability given by the knowledge of the intensity of the ground motion at the second period was insignificant. Using predictors that account for second and higher modes is expected to be useful for taller and more flexible structures. For the hazard analyses that consider the S_{di}'s, the PSHA code was modified according to Tothong and Cornell (2006b). Since the prediction equation for S_{di} is an extension of existing attenuation relationships for S_a, the computed scalar or vector S_{di} hazard is fully consistent with that expressed in terms of S_a.

The vector hazard instead has been computed following the procedure introduced by Bazzurro (1998), and Bazzurro and Cornell (2001 and 2002) and, for consistency, using the same prediction equation as in the scalar case.

2.5   *Methodology for the computation of probabilistic interstory drift hazard curves*

The statistical analyses of the building response (Subsection 2.3) provide a link between the level of ground motion and the expected response level while the seismic hazard analyses (Subsection 2.4) establish the likelihood that any level of ground motion will be observed at the building site. We seek to compute the curves that define the likelihood that the structural response, here measured by δ_{max}, may exceed different threshold values associated with important limit states (e.g., immediate occupancy, life safety, and collapse) for the building at a given site. These curves are obtained by coupling the building response with the site hazard via an operation called convolution, which is simply an application of the total probability theorem. For simplicity, these curves will be referred to as the drift hazard curves.

There is no clear consensus, however, on how response/hazard coupling should be accomplished, either in the research or in the practicing engineering communities. Some of the main issues are related to

- *a*   The interpretation of drift hazard curves from two 2D models for a structure which is, of course, a 3D entity and their comparison with drift hazard curves from a 3D model.
- *b*   The consideration for the orientation of the building's principal axes in a seismic environment that, in general, is not isotropic (e.g., Petersen and Frankel, 2003).
- *c*   The mechanics of the coupling to ensure that the response analysis and the hazard computations are combined correctly. For example, the response is often predicted based on $S_a(T)$ and the hazard is computed for $S_a(T)_{gm}$ or they are both based on the same quantity $S_a(T)$ but the dispersion of $S_a(T)$ for any given earthquake is underestimated in the hazard evaluation.

For items *a* and *b* above we developed the drift hazard curves for the 3D and the two 2D models for the three orientations of the building identified in Subsection 2.3. To address item *c* we have performed the coupling for the 16 combinations of S_a's and S_{di}'s in building response evaluation and in PSHA/VPSHA calculations listed in Table 3. Column 3 in Table 3 indicates whether the parameter used for predicting δ_{max} is for an average component or for an arbitrary component. Again, the selection of the former or the latter affects the uncertainty in the estimate of the response given the value of the predictor. Column 4 indicates which definition of the parameter is used in the hazard calculation and this affects the dispersion used in the prediction equation. If the parameter is for an average component the dispersion is the same published in the attenuation equation, if it is for an arbitrary component the dispersion is amplified as specified by Baker and Cornell (2006b). However, when the parameter is the geometric mean of S_a's and S_{di}'s at different periods and orientations (e.g., $S_a(T_{L1};T_{T1})_{gm}$ and $S_{di}(T_{L1};T_{T1})_{gm}$ as in cases 13 and 16), the dispersion of this single combined parameter is always obtained from the dispersion of the arbitrary component of the original parameters (e.g., $S_a(T_{L1})$ and $S_a(T_{T1})$). Column 5 specifies whether scalar or joint hazard were computed for the predictor(s) in Column 4. Finally, note that, as specified Column 7, the procedures for computing drift hazard curves for the Analysis cases 1, 4, and 7 are, rigorously speaking, incorrect. These cases are considered here only for discussion purposes since they are likely to be adopted in practice. Analysis cases 1-3 are performed for the transverse frame because it is prone to slightly larger floor displacements in the middle and top floors (see Figure 42 to come).

Analysis No.	Model Description	IM in response prediction	IM in PSHA/VPSHA	Dispersion in PSHA/VPSHA	Hazard analysis	Correct
1	Transverse Frame	$S_a(T_{T1})$	$S_a(T_{T1})_{gm}$	average component	PSHA	N
2	Transverse Frame	$S_a(T_{T1})$	$S_a(T_{T1})$	arbitrary component	PSHA	Y
3	Transverse Frame	$S_a(T_{T1})_{gm}$	$S_a(T_{T1})_{gm}$	average component	PSHA	Y
4	2 2D Frames	$S_a(T_{L1})$ and $S_a(T_{T1})$	$S_a(T_{L1})_{gm}$ and $S_a(T_{T1})_{gm}$	average component	2 PSHA	N
5	2 2D Frames	$S_a(T_{L1})$ and $S_a(T_{T1})$	$S_a(T_{L1})$ and $S_a(T_{T1})$	arbitrary component	2 PSHA	Y
6	2 2D Frames	$S_a(T_{L1})_{gm}$ and $S_a(T_{T1})_{gm}$	$S_a(T_{L1})$ and $S_a(T_{T1})_{gm}$	average component	2 PSHA	Y
7	2 2D Frames	$S_a(T_{L1};T_{T1})_{gm}$	$S_a(T_{L1};T_{T1})_{gm}$	arbitrary component	PSHA	Y
8	2 2D Frames	$S_{di}(T_{L1})$ and $S_{di}(T_{T1})$	$S_{di}(T_{L1})$ and $S_{di}(T_{T1})$	arbitrary component	2 PSHA	Y
9	3D Frame	$S_a(T_{L1})$ and $S_a(T_{T1})$	$S_a(T_{L1})_{gm}$ and $S_a(T_{T1})_{gm}$	average component	VPSHA	N
10	3D Frame	$S_a(T_{L1})$ and $S_a(T_{T1})$	$S_a(T_{L1})$ and $S_a(T_{T1})$	arbitrary component	VPSHA	Y
11	3D Frame	$S_a(T_{L1})$ and $S_a(T_{T1})$	$S_a(T_{L1})$ and $S_a(T_{T1})$	arbitrary component	2 PSHA	Y
12	3D Frame	$S_a(T_{L1})_{gm}$ and $S_a(T_{T1})_{gm}$	$S_a(T_{L1})_{gm}$ and $S_a(T_{T1})_{gm}$	average component	VPSHA	Y
13	3D Frame	$S_a(T_{L1};T_{T1})_{gm}$	$S_a(T_{L1};T_{T1})_{gm}$	arbitrary component	PSHA	Y
14	3D Frame	$S_{di}(T_{L1})$ and $S_{di}(T_{T1})$	$S_{di}(T_{L1})$ and $S_{di}(T_{T1})$	arbitrary component	2 PSHA	Y
15	3D Frame	$S_{di}(T_{L1})$ and $S_{di}(T_{T1})$	$S_{di}(T_{L1})$ and $S_{di}(T_{T1})$	arbitrary component	VPSHA	Y
16	3D Frame	$S_{di}(T_{L1};T_{T1})_{gm}$	$S_{di}(T_{L1};T_{T1})_{gm}$	arbitrary component	PSHA	Y

Table 3 Analysis cases considered for the evaluation of drift hazard curves.

3 ANALYSIS RESULTS

3.1 *Seismic hazard at the building site*

The site scalar and joint hazard at the downtown San Francisco site for the *IM*'s listed in Column 4 of Table 3 is shown for the undefined ground motion orientation in Figure 18 and Figure 19. This case applies to the undefined direction of the building (Orientation 3). Similarly, for the longitudinal frame of the building aligned with FN direction (approximately E-W for this site) (Orientation 2) the hazard is shown in Figure 20 and Figure 21. The hazard that applies to Orientation 1 of the building, namely the longitudinal frame aligned with the FP direction (approximately N-S for this site) is shown in Figure 22. The joint hazard for this last case is very similar to the hazard in Figure 21 because T_{L1} and T_{T1} are close and, therefore, it is omitted. Figure 23 shows the ratio of the $S_a(T_{L1})$ and $S_a(T_{L1})_{gm}$ hazard curves for the 3 different directions considered here. The hazard in S_{di} terms for the three building orientations is shown in Figure 24 to Figure 30. Note that in all these figures the scalar hazard is conventionally expressed in terms of mean annual frequency (MAF) of exceeding any specific acceleration value. The joint hazard, however, is expressed in terms of MAF or "equaling"

different acceleration values where, strictly speaking, "equaling" means "in the neighborhood of" the specified values.

The effect of the anisotropy of the spectral acceleration hazard appears to be noticeable from values of 0.3g and higher, which have mean return period (MRP) of at least 100 years at this location. For example, the MAF for a $S_a(T_{L1})$=1.0g in the E-W (FN) and N-S (FP) directions is within ±15% from the MAF for an unspecified, random direction (Figure 23a). Similarly, only the MAF of exceeding values of S_{di} equal to 0.5in or larger varies for the three different orientations of the building axes. As above, this value has a MRP of about 100 years. The MAF of exceeding 20in in the E-W (FN) and N-S (FP) directions is within ±15% from the MAF for an unspecified, random direction. Hence, for all practical purposes the anisotropy of the seismic hazard at this site and at this oscillator period becomes significant at hazard levels associated with MRP values of 1,000 years or longer. Similarly, the effects on the site hazard due to the difference in the uncertainty of the spectral acceleration for an arbitrary component or for an average component become noticeable only for acceleration levels with MRP of 1,000 years or longer.

Finally, by inspecting Figure 19, Figure 21, Figure 25, Figure 27, and Figure 29 it is clear that the correlation of the two ground motion parameters $S_a(T_{L1})$ and $S_a(T_{T1})$, or $S_{di}(T_{L1})$ and $S_{di}(T_{T1})$ at the site is very high. The joint hazard, in fact, resembles a very steep ridge. For example, the correlation coefficient, ρ_{tot}, between $S_a(T_{L1})$ and $S_a(T_{T1})$ at this site for the random orientation case is 0.97 for Orientations 1 and 2 and 0.89 for Orientation 3. Recall that the correlation of $S_a(T_{L1})$ and $S_a(T_{T1})$ at a site is composed of two factors. The first one, $\rho_{\varepsilon12}$, which is site-independent, is the correlation of $S_a(T_{L1})$ and $S_a(T_{T1})$ (given M and R) studied by Inoue (1990) and Baker and Cornell (2006b), which in this case is already high and amounts to 0.75. The second source of correlation, which is implicitly built in the PSHA code, (Bazzurro and Cornell, 2002) is due to the commonality (not equality) of the source-to-site decay of the two ground motion parameters for a given event. This second source of correlation is site-dependent because the decay of the ground motion parameters depends on M and R and each site has a unique distribution of M and R of nearby events. This second source of correlation alone would give a correlation coefficient, ρ_{MR}, of $S_a(T_{L1})$ and $S_a(T_{T1})$ at this site equal to 0.54 for Orientations 1 and 2 and of 0.43 for Orientation 3. The effects of the two sources of correlation can be appreciated by inspecting Figure 31 which, in the left panels displays the contours of the MAF of the $S_a(T_{L1})$ and $S_a(T_{T1})$ for the FP-FN case (Orientations 1 and 2, ρ_{tot}=0.97) and for the random case (Orientation 3, ρ_{tot}=0.89). The contours of the MAF that one would obtain by setting $\rho_{\varepsilon12}$=0 are, of course, much wider given the artificially lower correlation (ρ_{tot}=ρ_{MR}=0.54 in Panel (b) and ρ_{tot}=ρ_{MR}=0.43 in Panel (d)).

The correlation of $S_{di}(T_{L1})$ and $S_{di}(T_{T1})$ at this site is high but less pronounced than for the S_a case, as it is evident from Figure 25, Figure 27, Figure 29. This is because the $\rho_{\varepsilon12}$ term is lower for $S_{di}(T_{L1})$ and $S_{di}(T_{T1})$ of the 3D model, that is $\rho_{\varepsilon12}$=0.64 for the Orientations 1 and 2 case (FP-FN) and $\rho_{\varepsilon12}$=0.69 for the Orientation 3 case (random).

The extremely high correlation between these two ground motion parameters plays an important role in the discussion of the so-called "30% design rule" that will be discussed in Subsection 3.5.
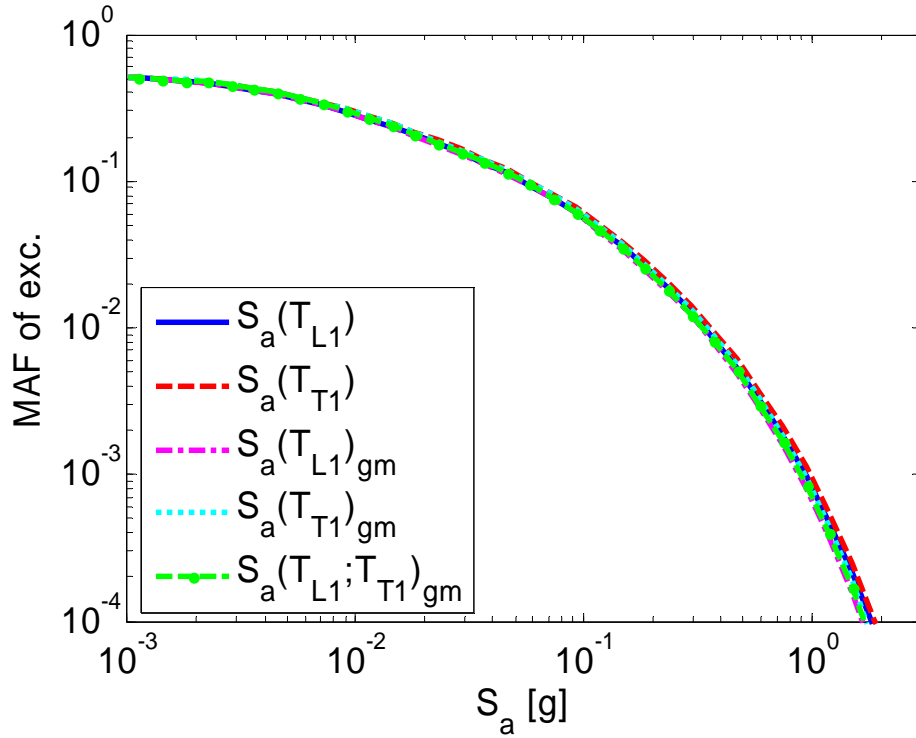
Figure 18 Scalar seismic hazard curves for $S_a(T_{L1})$, $S_a(T_{T1})$, $S_a(T_{L1})_{gm}$, $S_a(T_{T1})_{gm}$, and $S_a(T_{L1};T_{T1})_{gm}$ for an undefined ground shaking direction. This case applies to the undefined building orientation case (Orientation 3).
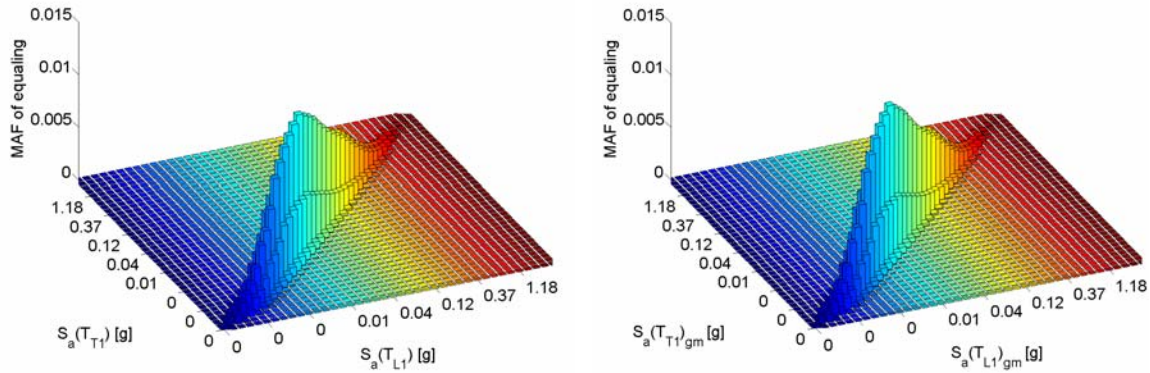

Figure 19 Joint seismic hazard for $S_a(T_{L1})$ and $S_a(T_{T1})$ (left) and for $S_a(T_{L1})_{gm}$ and $S_a(T_{T1})_{gm}$ (right) for an undefined direction. Note that $S_a(T_{L1})$ and $S_a(T_{T1})$ (and similarly for $S_a(T_{L1})_{gm}$ and $S_a(T_{T1})_{gm}$) refer to ground shaking along two orthogonal directions. This figure shows the MAF of "equaling" any pair of the two *IM*'s considered at this site. This case applies to the undefined building orientation case (Orientation 3).
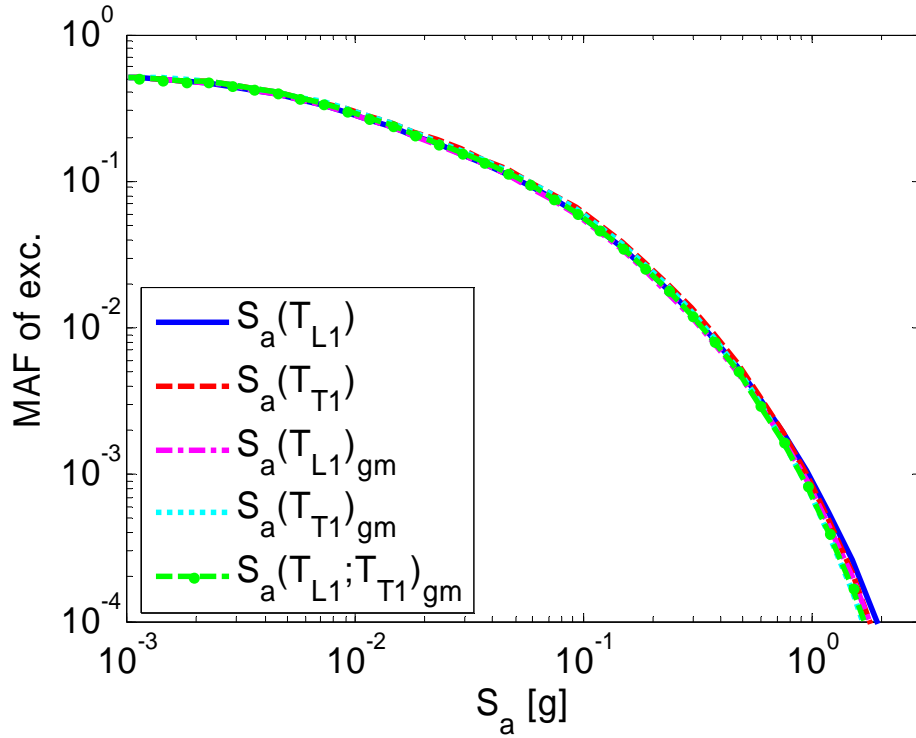
Figure 20 Scalar seismic hazard curves for $S_a(T_{L1})$, $S_a(T_{T1})$, $S_a(T_{L1})_{gm}$, $S_a(T_{T1})_{gm}$, and $S_a(T_{L1};T_{T1})_{gm}$ for the case with the longitudinal frame of the building aligned with FN conditions (Orientation 2). Given that the orientation of most faults in the San Francisco Bay Area is, approximately, N-S, the longitudinal frame is in the E-W direction. Note that in the case of $S_a(T_{L1};T_{T1})_{gm}$ the two components (before averaging) act in two orthogonal directions.
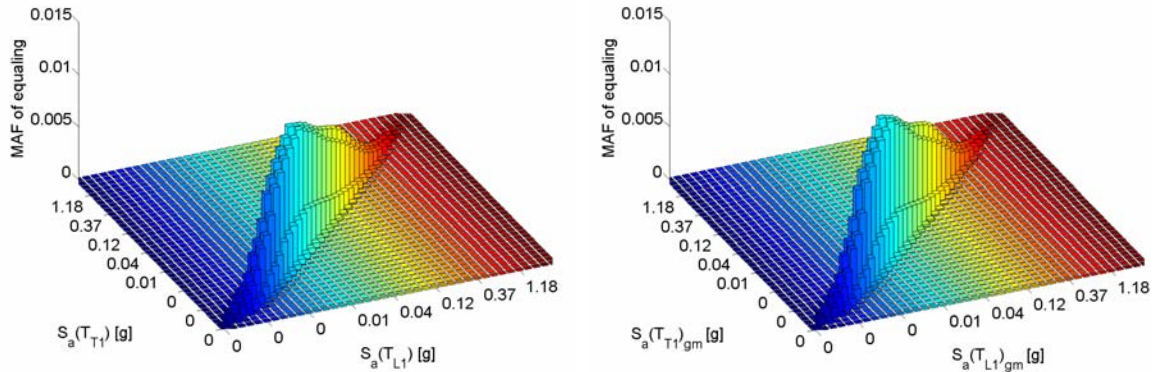

Figure 21 Joint seismic hazard for $S_a(T_{L1})$ and $S_a(T_{T1})$ (left) and for $S_a(T_{L1})_{gm}$ and $S_a(T_{T1})_{gm}$ (right) for the case with the longitudinal frame of the building aligned with FN conditions (Orientation 2). The case on the left assumes that $S_a(T_{L1})$ acts in FN direction (E-W) and $S_a(T_{T1})$ in FP direction (N-S). Ditto for $S_a(T_{L1})_{gm}$ and $S_a(T_{T1})_{gm}$ for the case on the right. This figure shows the MAF of "equaling" any pair of the two **IM**'s considered at this site.
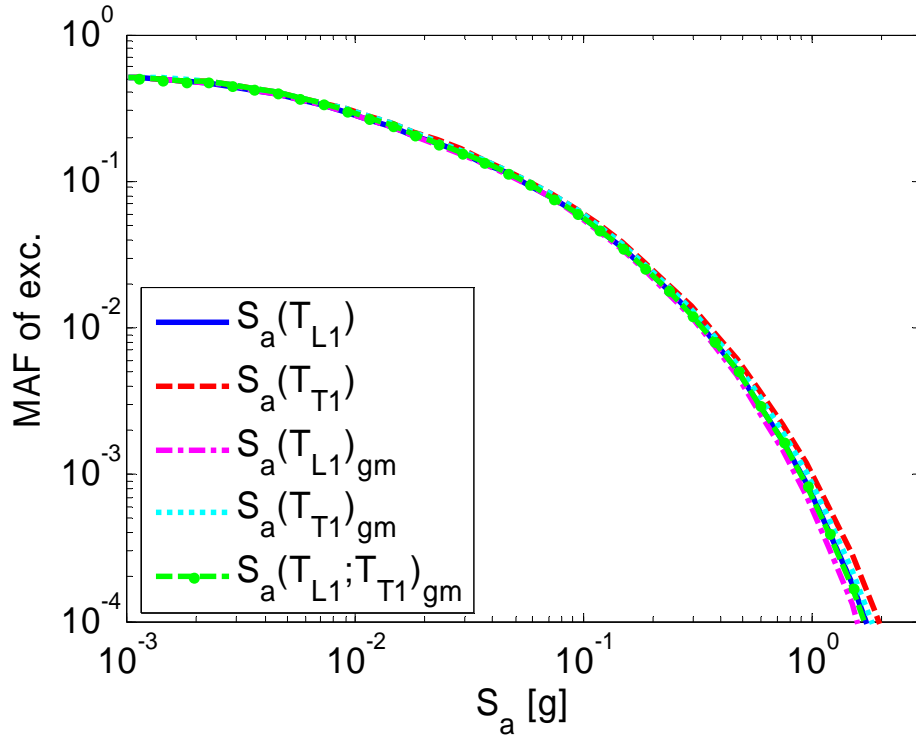
Figure 22 Scalar seismic hazard curves for $S_a(T_{L1})$, $S_a(T_{T1})$, $S_a(T_{L1})_{gm}$, $S_a(T_{T1})_{gm}$, and $S_a(T_{L1};T_{T1})_{gm}$ for the case with the longitudinal frame of the building aligned with FP conditions (Orientation 1). Given that the orientation of most faults in the San Francisco Bay Area is, approximately, N-S, the longitudinal frame is in the N-S direction. Note that in the case of $S_a(T_{L1};T_{T1})_{gm}$ the two components (before averaging) act in two orthogonal directions.
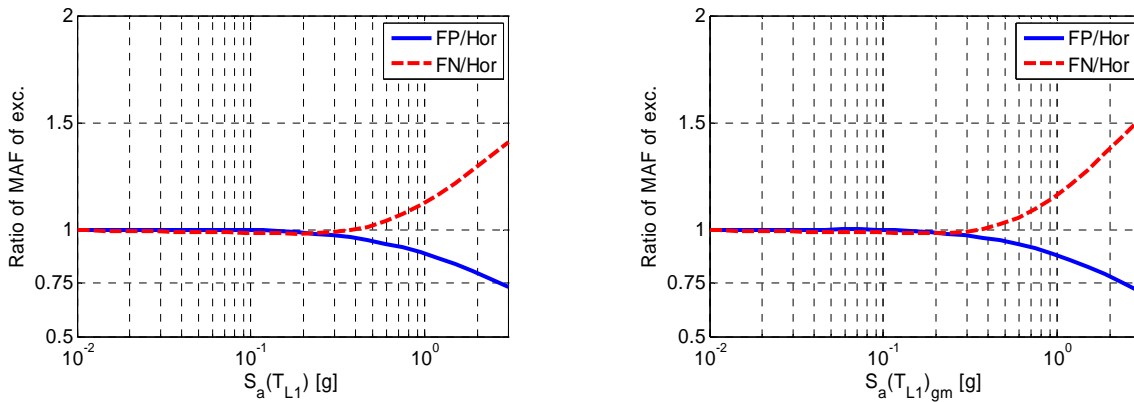
Figure 23 Ratio of the hazard curves for the FP and FN directions to that for the unspecified direction for $S_a(T_{L1})$ (left) and $S_a(T_{L1})_{gm}$ (right). The ratio for the other definitions of spectral accelerations is similar.
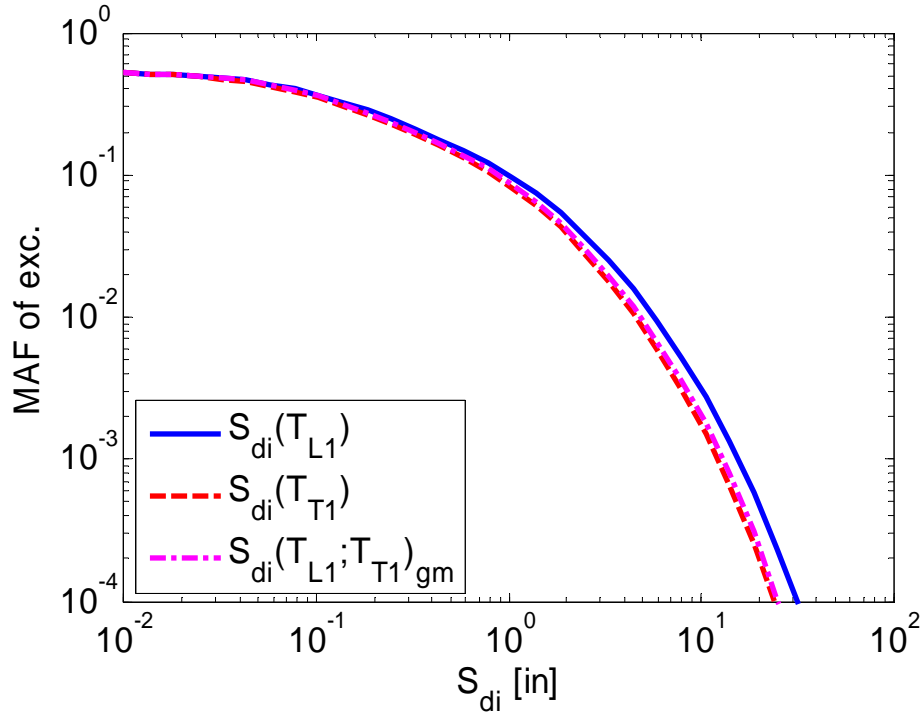
Figure 24 Scalar seismic hazard curves for $S_{di}(T_{L1})$, $S_{di}(T_{T1})$, and $S_{di}(T_{L1};T_{T1})_{gm}$ for an undefined ground shaking direction. This case applies to the undefined building orientation case (Orientation 3).
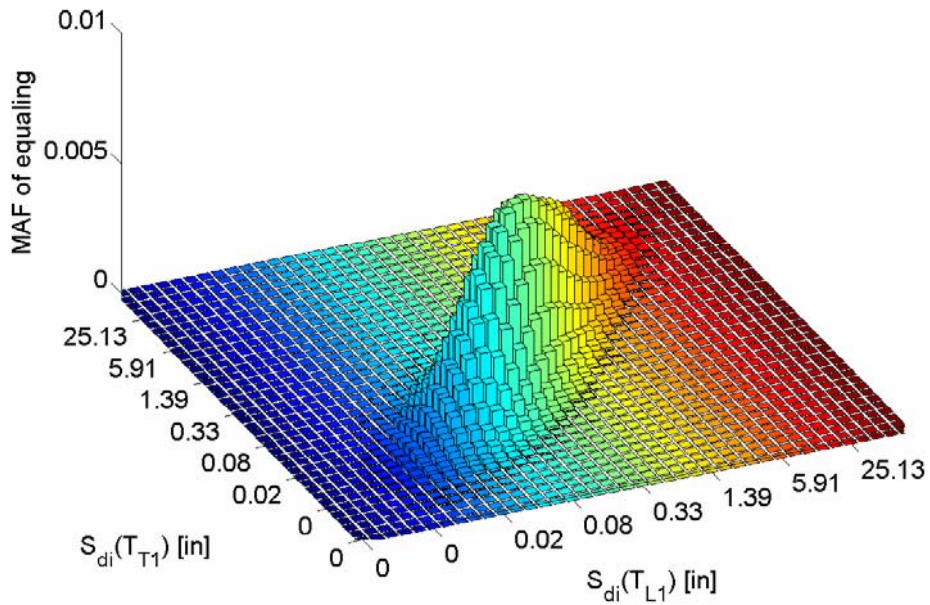
Figure 25 Joint seismic hazard for $S_{di}(T_{L1})$ and $S_{di}(T_{T1})$ for an undefined direction. Note that $S_{di}(T_{L1})$ and $S_{di}(T_{T1})$ refer to ground shaking along two orthogonal directions. This case applies to the undefined building orientation case (Orientation 3).
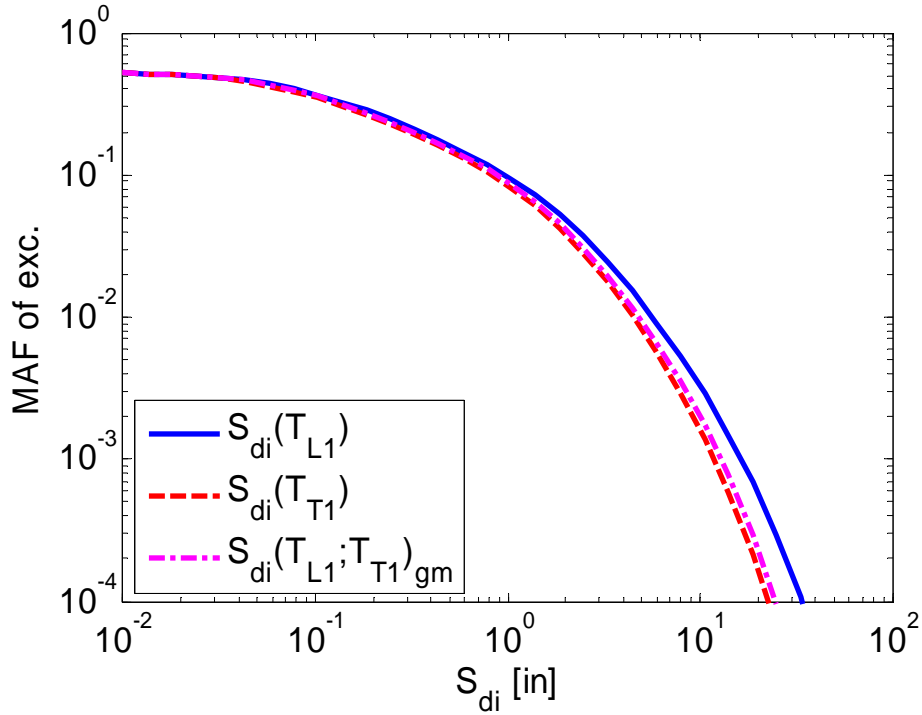
Figure 26 Scalar seismic hazard curves for $S_{di}(T_{L1})$, $S_{di}(T_{T1})$, and $S_{di}(T_{L1};T_{T1})_{gm}$ for the case with the longitudinal frame of the building aligned with FN conditions (Orientation 2). Given that the orientation of most faults in the San Francisco Bay Area is, approximately, N-S, the longitudinal frame is in the E-W direction. Note that in the case of $S_{di}(T_{L1};T_{T1})_{gm}$ the two components (before averaging) act in two orthogonal directions.
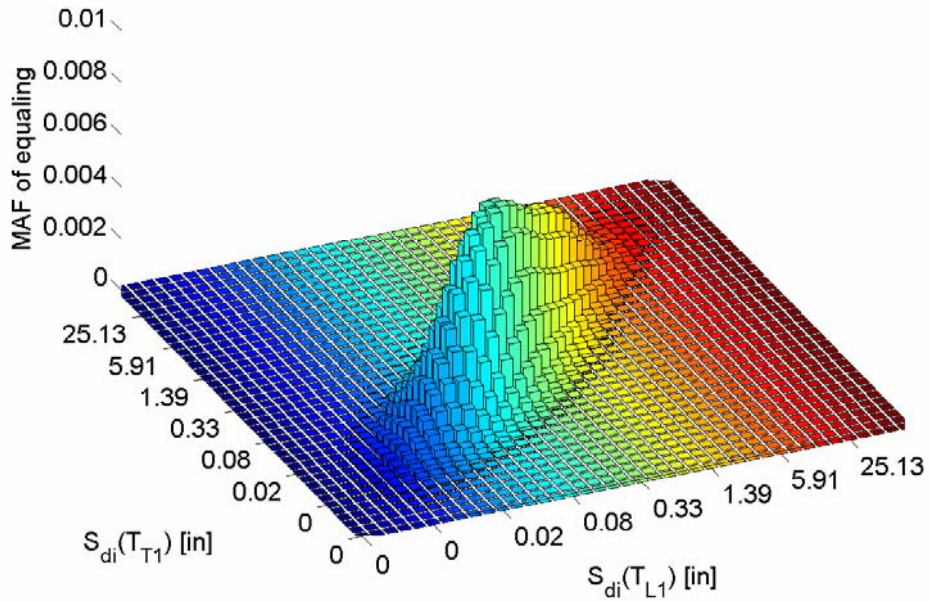
Figure 27 Joint seismic hazard for $S_{di}(T_{L1})$ and $S_{di}(T_{T1})$ for the case with the longitudinal frame of the building aligned with FN conditions (Orientation 2). It is assumed that $S_{di}(T_{L1})$ acts in FN direction (E-W) and $S_{di}(T_{T1})$ in FP direction (N-S).
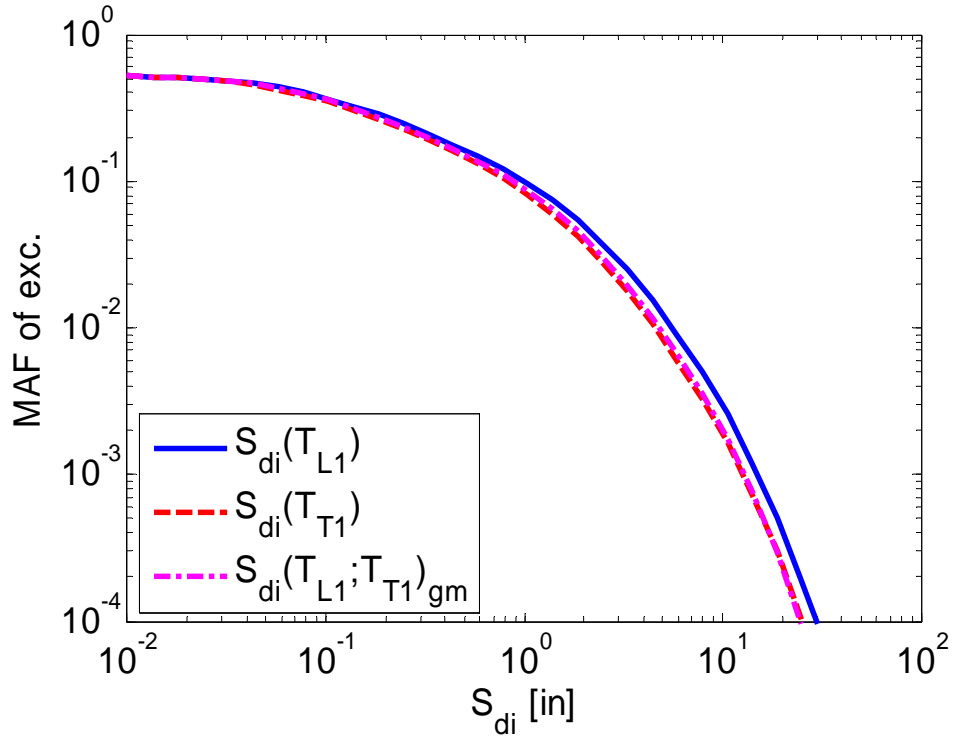
Figure 28 Scalar seismic hazard curves for $S_{di}(T_{L1})$, $S_{di}(T_{T1})$, and $S_{di}(T_{L1};T_{T1})_{gm}$ for the case with the longitudinal frame of the building aligned with FP conditions (Orientation 1). Given that the orientation of most faults in the San Francisco Bay Area is, approximately, N-S, the longitudinal frame is in the N-S direction. Note that in the case of $S_{di}(T_{L1};T_{T1})_{gm}$ the two components (before averaging) act in two orthogonal directions.
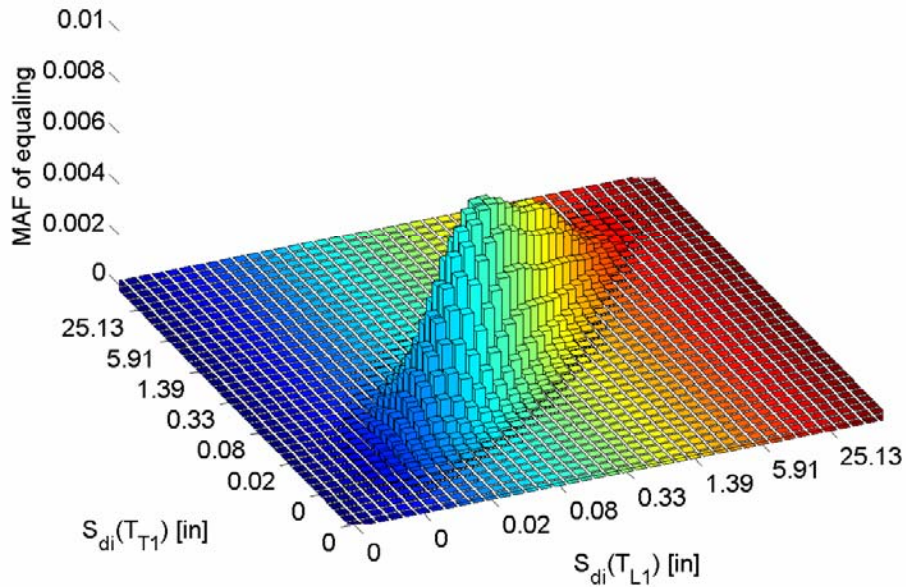
Figure 29 Joint seismic hazard for $S_{di}(T_{L1})$ and $S_{di}(T_{T1})$ for the case with the longitudinal frame of the building aligned with FP conditions (Orientation 1). It is assumed that $S_{di}(T_{L1})$ acts in FP direction (N-S) and $S_{di}(T_{T1})$ in FN direction (E-W).

31
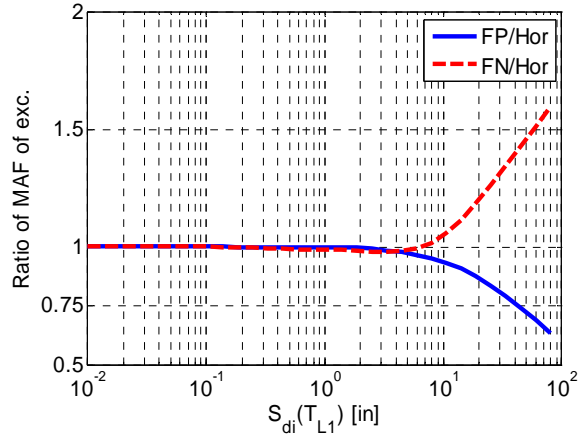
Figure 30 Ratio of the $S_{di}(T_{L1})$ hazard curves for the FP and FN directions to that for the unspecified direction. The ratio for the other definitions of inelastic spectral displacement is similar.

(a) Orientations 1 and 2 (FP-FN)

(b) Orientations 1 and 2 (FP-FN)

(c) Orientation 3 (random)

(d) Orientation 3 (random)
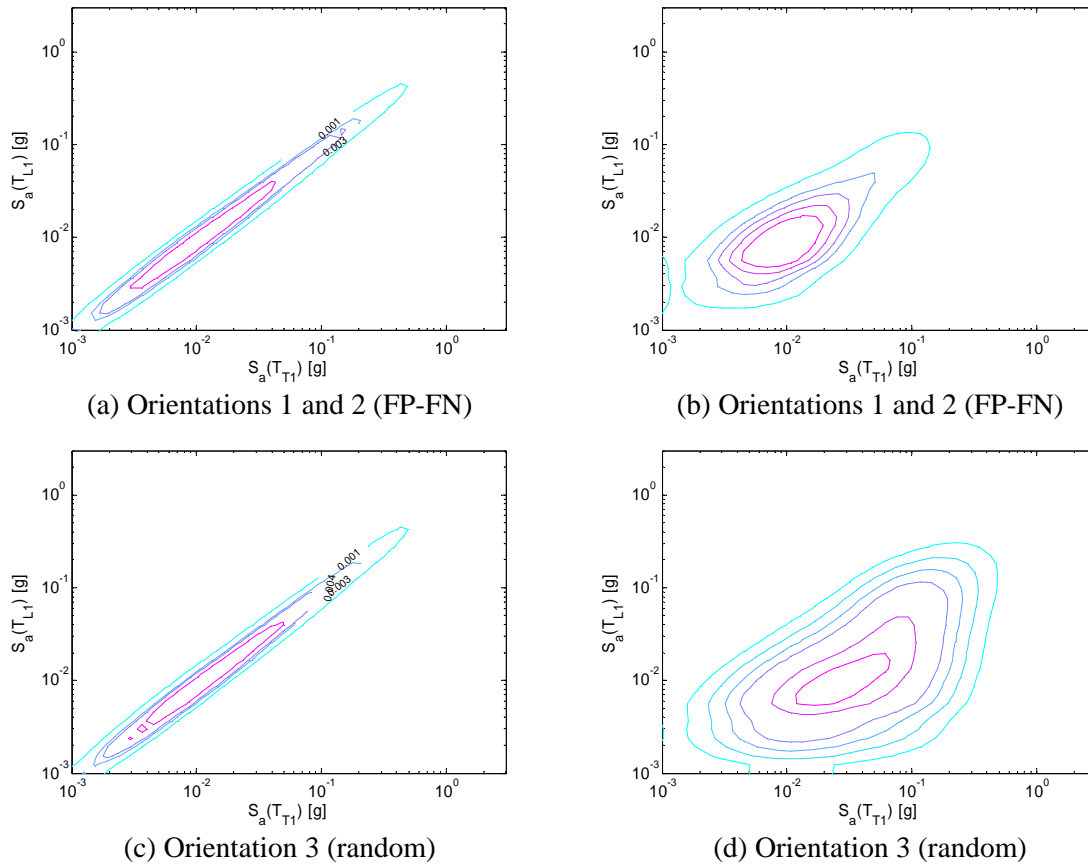
Figure 31 (Left) Contours of the MAF of equaling different levels of $S_a(T_{L1})$-$S_a(T_{T1})$ pairs at this site. The contours in (a) are from the MAF in the left panel of Figure 21and those in (b) are from the MAF of Figure 19. The contours in (b) and (d) are obtained by setting to zero the site-independent part of the correlation (i.e., that from Baker and Cornell, 2006b).

32

3.2   Building responses to seismic excitation

Building failure modes, deformed shapes, and interstory drifts

The set of results shown in this section intends to describe the behavior of the building subject to earthquake ground motion. A more systematic study on the prediction of the building response given the intensity of the ground motion is included in Subsection 3.3.

Figure 32 shows the static pushover curves obtained from the 2D longitudinal and transverse models, respectively. Figure 33 displays how the peak interstory drift in both directions varies along the height of the building for increasing levels of roof lateral displacement. At about 9in of roof lateral displacement the response of the building becomes unstable (at least statically) because of the shear failure of several columns at Stories 3, 4, and 5.   The instability occurs at approximately 1.1% roof drift with a corresponding peak interstory drift at Story 4 of about 2%. These drift values, however, should not necessarily be associated with physical building failure but with significant deterioration of the building global strength. The OpenSees static pushover algorithms could not handle the negative stiffness curves of the shear springs shown in Figure 5 and, therefore, the deteriorating part of the global pushover curve could not be determined. The occurrence of the failure modes along mid height of the building is consistent with the characteristics of the shear capacities of the springs located at these three stories that are lower than those at other floors by design, as explained in Subsection 2.1.
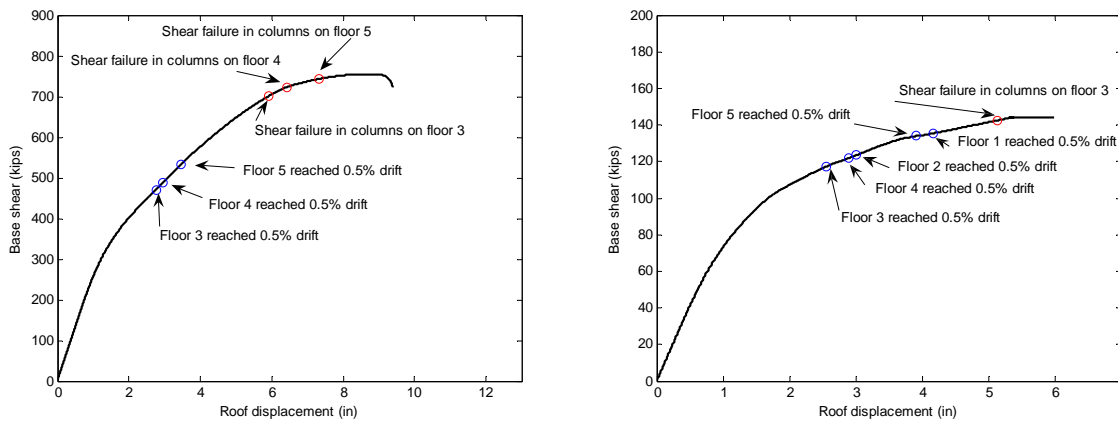

Figure 32 Static pushover curve in longitudinal direction (left) and transverse direction (right) obtained with the 2D models of the building (Figure 2 and Figure 3).
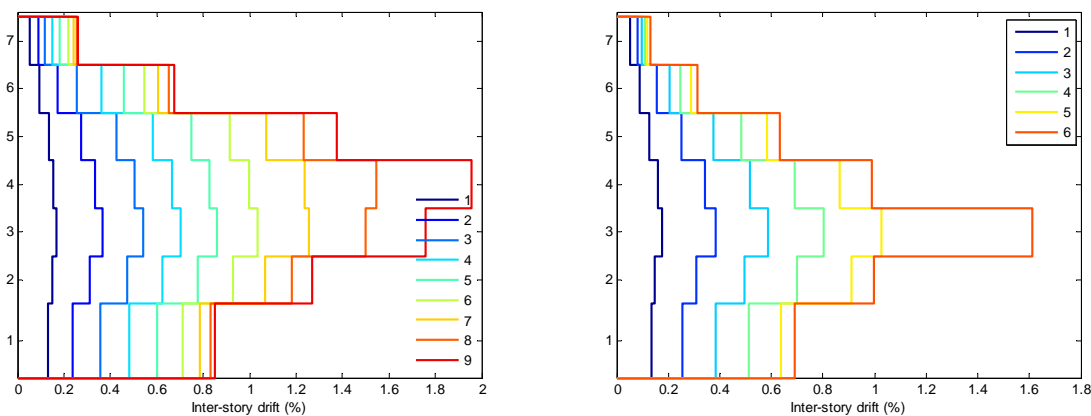

Figure 33 Interstory drift along the height of the building for roof displacements ranging from 1 to 9 inches in longitudinal (left) and transverse (right) directions from the static pushover analysis.

The failure mode identified by the static pushover is also confirmed by the dynamic analyses, which show that, in most cases, the largest drifts are observed at stories 3, 4, and 5. Figure 34 and Figure 35 illustrates the percentage of runs that exhibit peak interstory drifts in exceedance of 2, 3, 4, and 5% in longitudinal and transverse directions, respectively. Large interstory drifts, which indicate other less likely failure modes in addition to that identified above, occur also at other stories. As expected, the dynamic analyses show that the building can absorb larger deformations than those indicated by the static pushover analysis. The peak floor displacements and peak interstory drifts obtained by subjecting the 3D model to each one of the 100 record pairs for the three orientations of the building are depicted in Figure 36 to Figure 41. In these figures the median (50th percentile) line is plotted in red while the 16th and 84th percentile lines are shown in blue. Although inertia forces clearly allow the building to recover from large deformations when the ground shaking reverses its direction, values of peak interstory drifts in exceedance of 5% to 6% in brittle concrete frames may not be physically realizable and should be considered with extreme caution.
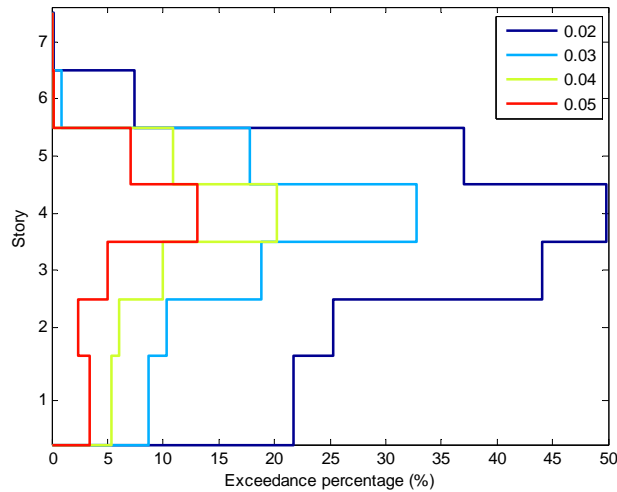

Figure 34 Percentage of records in the database that induce a peak interstory drift at each story in exceedance of 2, 3, 4, and 5% in the longitudinal direction (Figure 2). This figure includes the results from both the 3D and 2D models and for all three building orientations.
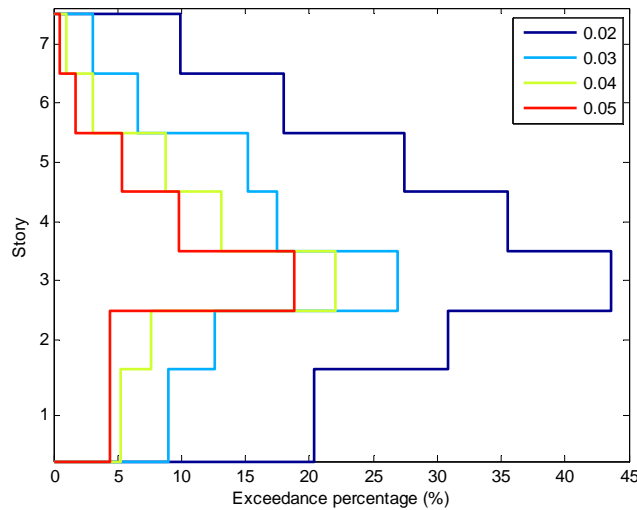

Figure 35 Percentage of records in the database that induce a peak interstory drift at each story in exceedance of 2, 3, 4, and 5% in the transverse direction (Figure 3). This figure includes the results from both the 3D and 2D models and for all three building orientations.
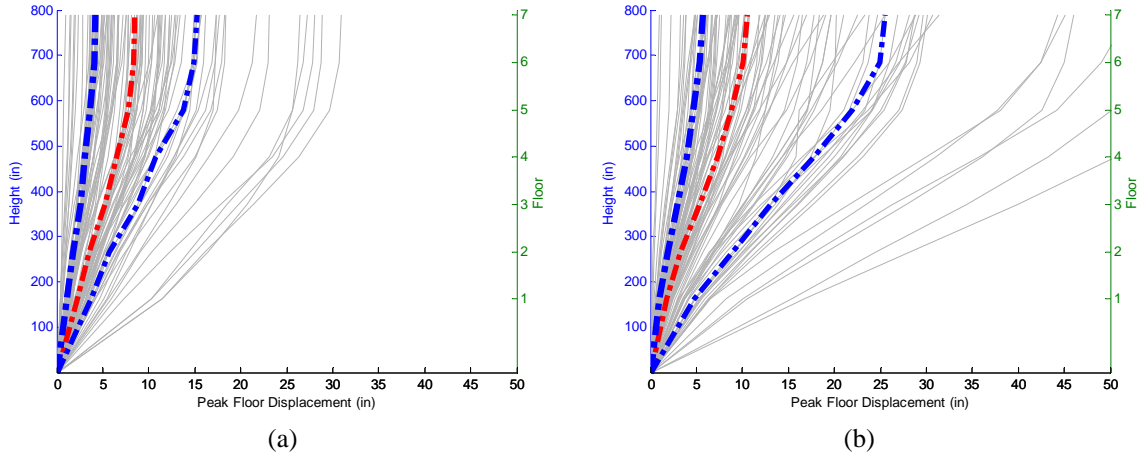
Figure 36 Peak floor displacement in the longitudinal direction (a) and transverse direction (b) of the 3D model of the building caused by each of the 100 record pairs. This set of results refers to Orientation 1.
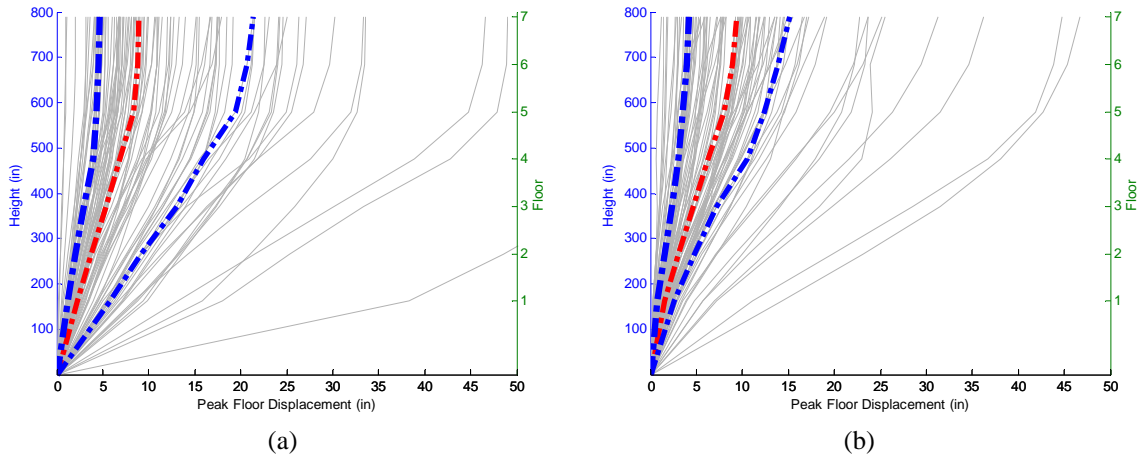

Figure 37 Peak floor displacement in the longitudinal direction (a) and transverse direction (b) of the 3D model of the building caused by each of the 100 record pairs. This set of results refers to Orientation 2.
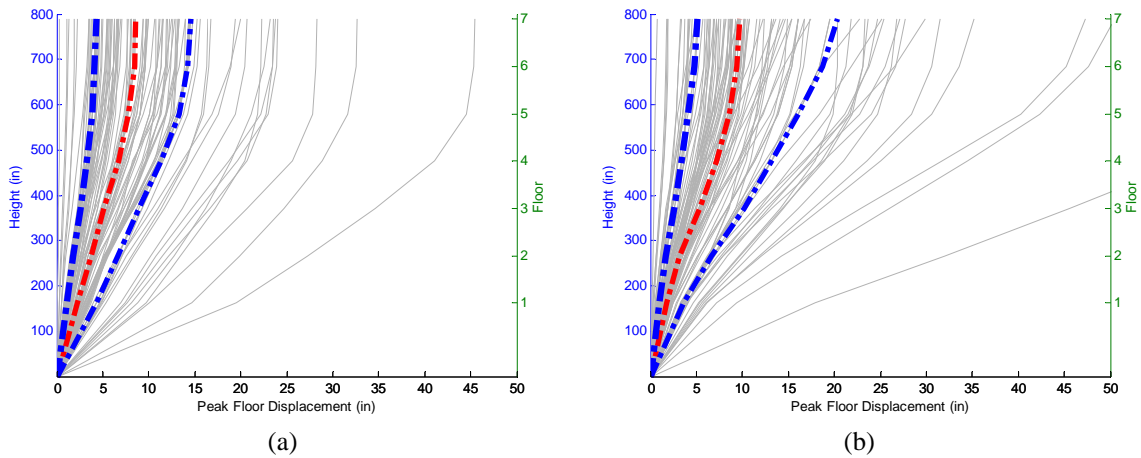
Figure 38 Peak floor displacement in the longitudinal direction (a) and transverse direction (b) of the 3D model of the building caused by each of the 100 record pairs. This set of results refers to Orientation 3.
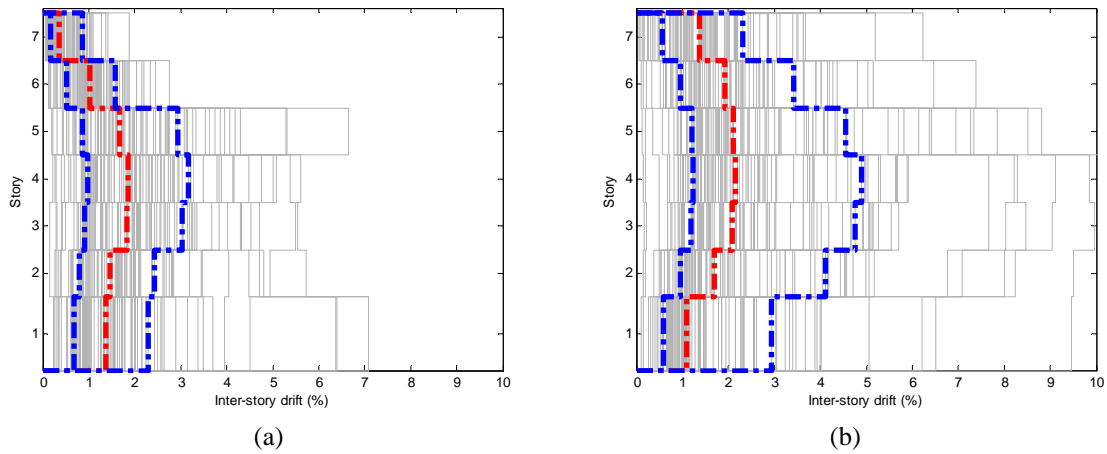
Figure 39 Peak interstory drift in the longitudinal direction (a) and transverse direction (b) of the 3D model of the building caused by each of the 100 record pairs. This set of results refers to Orientation 1.
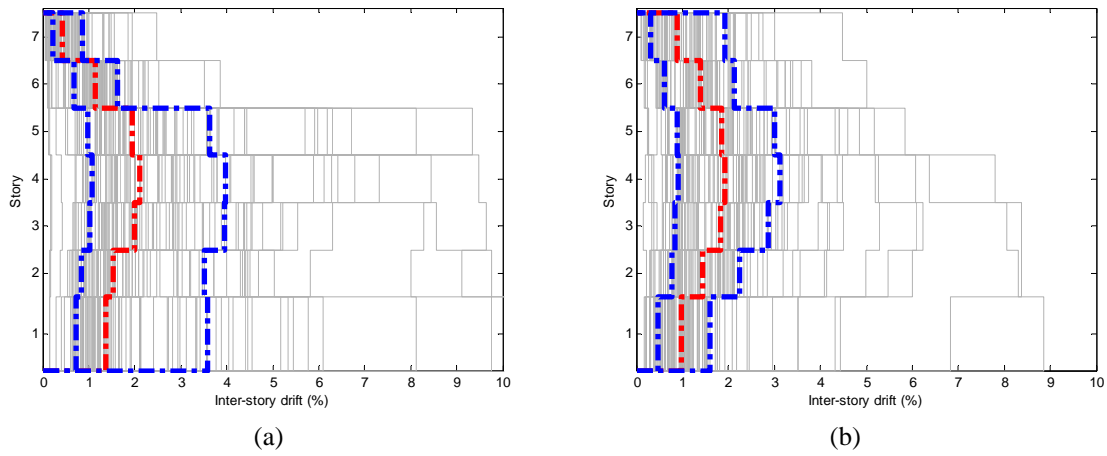
Figure 40 Peak interstory drift in the longitudinal direction (a) and transverse direction (b) of the 3D model of the building caused by each of the 100 record pairs. This set of results refers to Orientation 2.
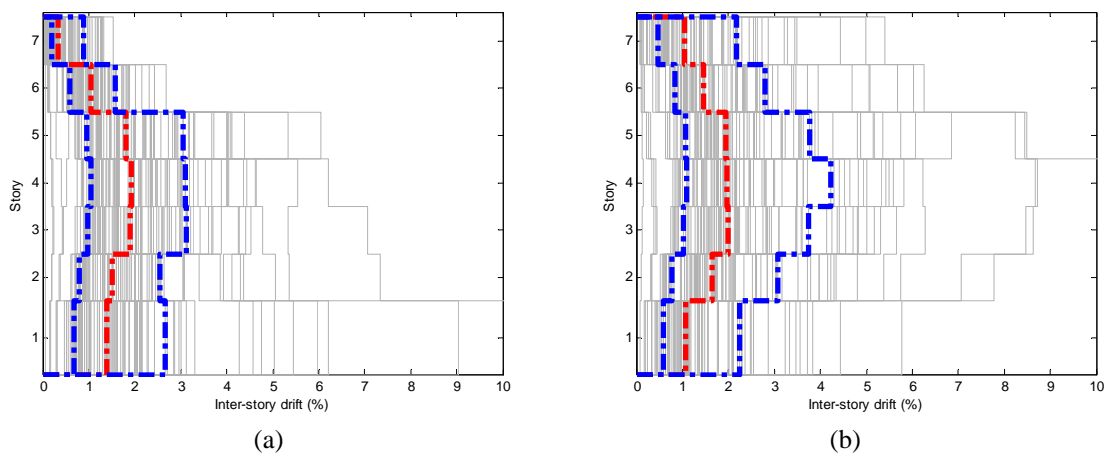
Figure 41 Peak interstory drift in the longitudinal direction (a) and transverse direction (b) of the 3D model of the building caused by each of the 100 record pairs. This set of results refers to Orientation 3.

A comparison of the displacement and drift results in Figure 36 to Figure 41 indicates that the peak floor displacements and interstory drifts are comparable in longitudinal and transverse directions. This finding is made clearer by Figure 42, which shows the curves representing the ratio of the transverse to longitudinal median peak displacement along the building height and the corresponding ratios of median peak interstory drifts for the 3D model. On average, the transverse frame undergoes somewhat larger drifts from the third story up and lower drifts at the first story. Given the similar strength of the two frames, it is apparent that, on average, the largest deformations are observed in the building frame aligned with the fault-normal direction (E-W here) shaken by the "stronger" component.

(a)　　　　　　　　　　　　　　　　(b)
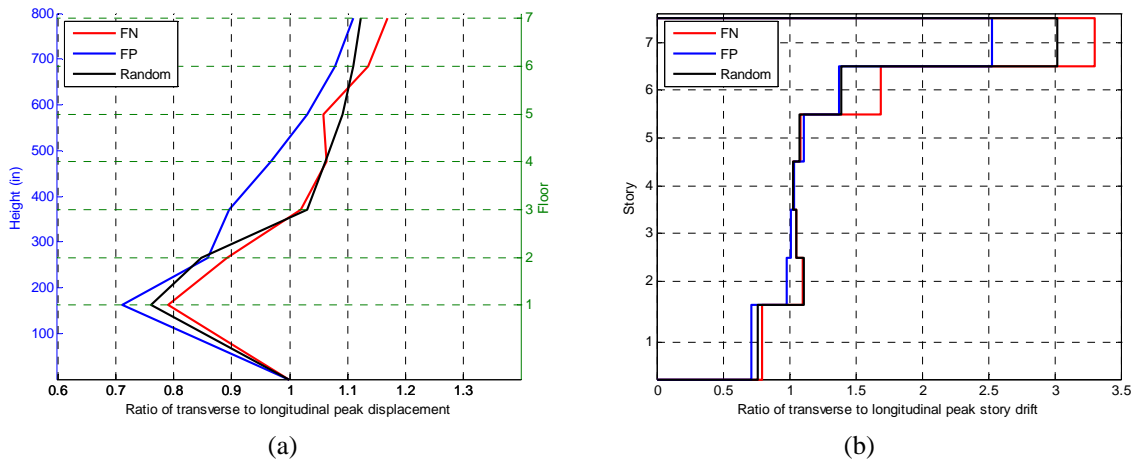
Figure 42 Ratio of the transverse to longitudinal median peak displacement curves along the height of the building (a) and corresponding ratio of peak interstory drifts (b) found using the 3D model. The curves refer to peak displacements caused in each direction by the following three cases: random component (Figure 36), FN component (Figure 37a and Figure 38b), and FP component (Figure 37b and Figure 38a).

Comparison of results from 2D and 3D models

Most of the results shown in this subsection were obtained using the 3D model of the building. In general, the δ_{max} in the same direction observed in the 2D models shaken by one horizontal component and in the 3D model shaken by both horizontal components were similar for the records that induced $\delta_{max} \leq 2\%$. Figure 43 shows a case where the similarity between the 2D and the 3D response is apparent. Some larger deformation cases, however, show a more significant discrepancy with larger drift values often found in the 2D models, especially in the 2D transverse model that does not account for the contribution of the gravity frames. This is apparent from Figure 44. Figure 44a presents the comparison of the δ_{max} caused in longitudinal direction by the FN component of the records computed using the 3D model (ordinates) and the 2D model (abscissa). The analogous plot with FN components acting in the transverse direction of the building is displayed in Figure 44b. Similar graphs for the FP and random components support this conclusion, although the difference of the 2D vs. 3D results at large δ_{max} levels is less pronounced.

The difference between the 3D and the 2D responses is due to several reasons both related to the seismic load and to modeling aspects:

- The action of the additional horizontal ground motion component in the 3D model.
- The contribution to the lateral force resisting system along one axis in the 3D model due to the presence of frames along the orthogonal axis.
- The absence of a gravity frame in the 2D model in transverse direction. When sufficient columns fail at adjacent stories in the 2D transverse frame a mechanism forms and a floor unzips. In the 3D case the unzipping would not necessarily happen given the presence of the interior gravity

frames in both directions and of the moment resisting frames in the orthogonal direction. This difference is clear from the inspection of the peak floor displacement curves in transverse direction obtained with the 3D model (Figure 45a) and the 2D transverse model (Figure 45b).
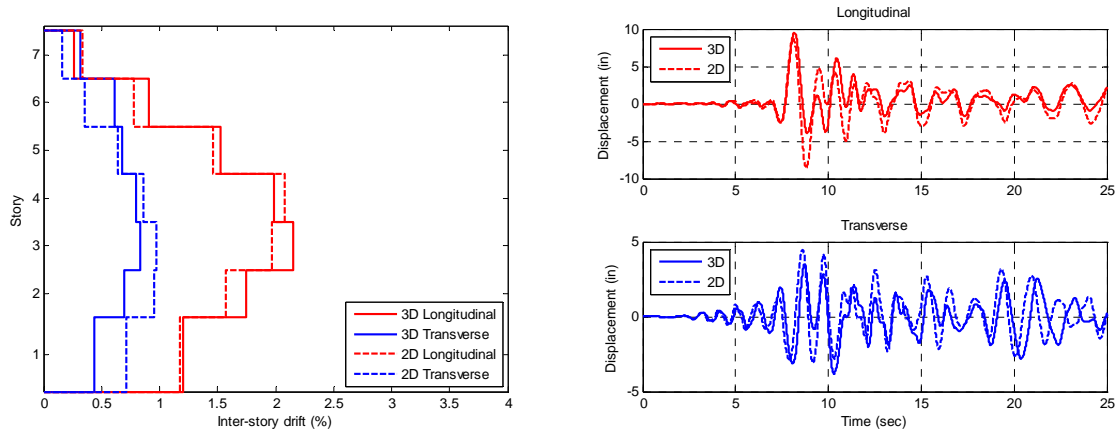
Figure 43 Peak interstory drift in the longitudinal and transverse direction subject to the M6.36 Coalinga Earthquake of 02/05/83 computed using both the 3D and the 2D models. These results are for Orientation 2 of the building.

(a) (b)
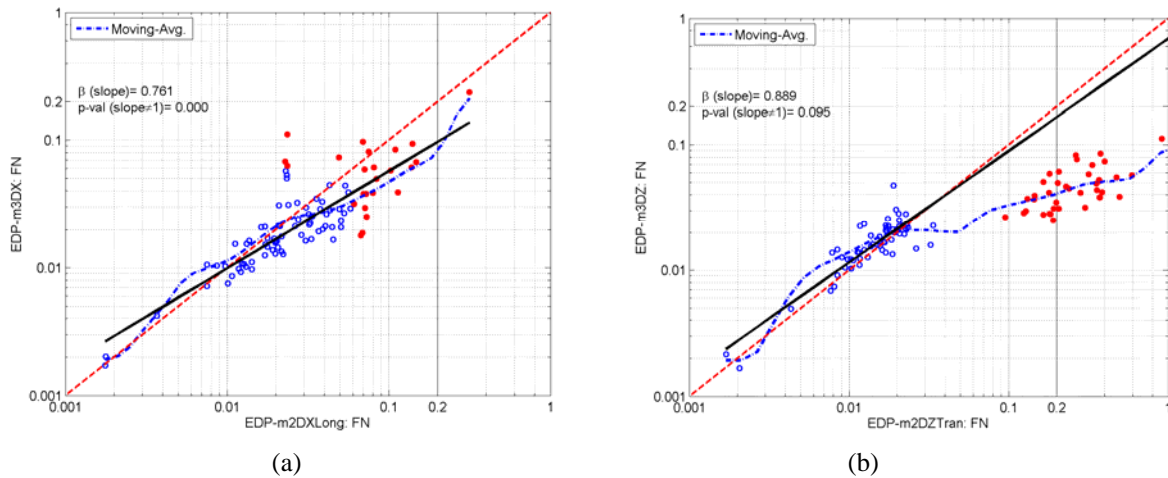
Figure 44 (a) Values of δ_{max} in longitudinal direction caused by the FN components applied to the 3D model (Y axis) and to the 2D model (X axis). (b) Same as above for the transverse direction. The solid line is a linear regression of the blue dots with $\delta_{max} \leq 6\%$ while the dotted line is the moving average of all the results. The red dots identify the runs with $\delta_{max} > 6\%$ in either one of the models.

(a)   (b)
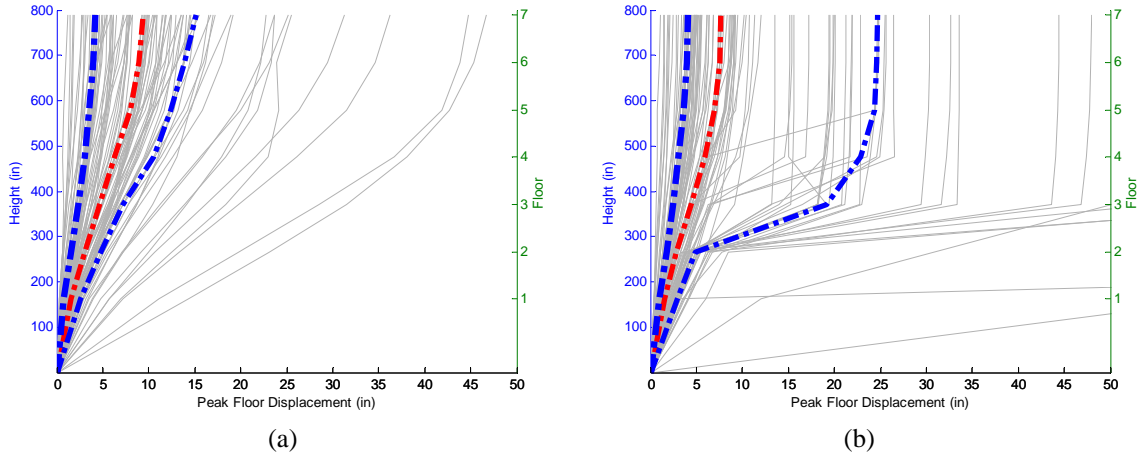
Figure 45 Peak floor displacement curves in the transverse direction from the 3D model (a) and from the 2D transverse model (b) subject to the FP components of the records (Orientation 2).

3.3   *Statistical analysis of building response*

The results of the δ_{max} statistical prediction exercise involving the 16 different cases of building models and ground motion *IM*'s listed in Table 3 are summarized here. The statistical analyses were repeated for the drifts obtained for the three different orientations of the structure for a total of 15 different cases (Table 4). The full statistical model that includes also the moment magnitude, *M*, and site-to-rupture distance, *R*, as predictors can be written as follows

$$\ln \delta_{\max} = \beta_0 + \beta_1 IM_1 + \cdots + \beta_n IM_n + \beta_{n+1}M + \beta_{n+2} \ln R + \varepsilon \sigma_{\ln \delta | IM} \qquad (1)$$

Where the β's represent the parameters of the regression; the *IM*'s are intensity measures of the ground motion, such as those in the third column of Table 3; ε is a standard normal variable representing the regression error; and $\sigma_{ln\delta | IM}$ is the standard error of estimation of (the natural log of) δ_{max} conditional on the *IM*'s in the regression model. Only the δ_{max} values below 6% were used in the regression. Larger values of 6% were considered as collapse cases and treated separately in the drift hazard calculations, as discussed in Subsection 3.4. *M* and *R* were included in the pool of predictors only for completeness sake. As discussed later, their contributions to explaining variability in the drifts of this building when $S_a(T_1)$ or $S_{di}(T_1)$ are already in the model is minimal and *M* and *R* were then subsequently dropped from any other statistical analysis.

Building Model	Direction of displacement	Record Component in direction of displacement		
		Orientation 1	Orientation 2	Orientation 3
3D	Longitudinal	FP	FN	Hor2
3D	Transverse	FN	FP	Hor1
3D	Vector sum	FP - FN	FN - FP	Hor2 - Hor1
2D	Longitudinal	FP	FN	Hor2
2D	Transverse	FN	FP	Hor1

Table 4 Different cases considered in the statistical analysis for the prediction of δ_{max} for this building. Hor1 and Hor2 stand for the randomly selected horizontal components as recorded. In the vector sum case the record components applied in each direction of the building axes change with building orientation as specified in the table.

As implied in Table 4, we considered three different variations of δ_{max} as the building response measure:

39

- $\delta_{max,L}$ in the building longitudinal direction
- $\delta_{max,T}$ in the building transverse direction
- $\delta_{max,sum}$, which is the maximum value of the vector sum of the peak interstory drift at each story. In any given run at each story the interstory drifts in longitudinal and transverse direction are combined at any time step and the peak value over time is selected. $\delta_{max,sum}$ is the maximum value across stories. The quantity $\delta_{max,sum}$ refers to a displacement that does not occur in the direction of the major building axes but at an angle, which, , in general, is different for each record pair.

The salient results of all the regression analyses are summarized in Table 5, Table 6, and Table 7 and in Figure 46 to Figure 50. The engineering demand parameter, *EDP*, is $\delta_{max,L}$ in Table 5, $\delta_{max,T}$ in Table 6, and $\delta_{max,sum}$ in Table 7 and the β's are the regression parameters in Eq. 1. Note that additional parameters after the first one are often added as ratios to avoid problems due to collinearity in the regression.

3D - Longitudinal

No.	IM	Orientation 1 - FP					Orientation 2 - FN					Orientation 3 - Hor2				
		$\sigma_{lnEDP\|IM}$	$\sigma_{lnEDP\|IM,M,R}$	β_0	β_1	β_2	$\sigma_{lnEDP\|IM}$	$\sigma_{lnEDP\|IM,M,R}$	β_0	β_1	β_2	$\sigma_{lnEDP\|IM}$	$\sigma_{lnEDP\|IM,M,R}$	β_0	β_1	β_2
1	$S_a(T_{L1})$	0.317	0.309	-2.980	0.955	NaN	0.373	0.369	-2.912	1.018	NaN	0.368	0.363	-2.938	0.999	NaN
2	$\{S_a(T_{L1}); S_a(T_{T1})/S_a(T_{L1})\}$	0.305	0.302	-2.931	1.054	0.164	0.356	0.350	-2.803	1.132	0.215	0.362	0.358	-2.924	1.051	0.157
3	$\{S_a(T_{L1})_{gm}; S_a(T_{T1})_{gm}/S_a(T_{L1})_{gm}\}$	0.380	0.382	-2.997	1.029	0.012	0.406	0.391	-2.912	1.082	0.762	0.408	0.404	-3.063	1.022	0.538
4	$\{S_a(T_{L1}); S_a(T_{T1})\}_{gm}$	0.383	0.382	-3.093	1.022	NaN	0.414	0.400	-2.891	1.057	NaN	0.411	0.406	-3.052	1.019	NaN
5	$S_{di}(T_{L1})$	0.242	0.244	-5.856	1.051	NaN	0.270	0.271	-5.881	1.031	NaN	0.252	0.253	-5.875	1.043	NaN
6	$\{S_{di}(T_{L1}); S_{di}(T_{T1})/S_{di}(T_{L1})\}$	0.241	0.243	-5.901	1.070	0.070	0.266	0.264	-5.933	1.074	0.110	0.245	0.246	-5.941	1.078	0.121
7	$\{S_{di}(T_{L1}); S_{di}(T_{T1})\}_{gm}$	0.345	0.344	-5.776	0.954	NaN	0.356	0.348	-5.747	1.032	NaN	0.334	0.337	-5.877	1.033	NaN

(a)

3D - Transverse

No.	IM	Orientation 1 - FN					Orientation 2 - FP					Orientation 3 - Hor1				
		$\sigma_{lnEDP\|IM}$	$\sigma_{lnEDP\|IM,M,R}$	β_0	β_1	β_2	$\sigma_{lnEDP\|IM}$	$\sigma_{lnEDP\|IM,M,R}$	β_0	β_1	β_2	$\sigma_{lnEDP\|IM}$	$\sigma_{lnEDP\|IM,M,R}$	β_0	β_1	β_2
1	$S_a(T_{T1})$	0.424	0.402	-3.130	0.888	NaN	0.376	0.366	-3.296	0.772	NaN	0.359	0.333	-3.188	0.846	NaN
2	$\{S_a(T_{T1}); S_a(T_{L1})/S_a(T_{T1})\}$	0.399	0.386	-2.879	1.082	0.283	0.374	0.367	-3.245	0.829	0.100	0.329	0.313	-3.018	0.961	0.312
3	$\{S_a(T_{T1})_{gm}; S_a(T_{L1})_{gm}/S_a(T_{T1})_{gm}\}$	0.428	0.415	-2.802	1.073	0.504	0.413	0.414	-3.184	0.867	0.676	0.325	0.313	-2.933	0.981	0.673
4	$\{S_a(T_{T1}); S_a(T_{L1})\}_{gm}$	0.431	0.416	-2.797	1.077	NaN	0.421	0.421	-3.259	0.826	NaN	0.339	0.325	-2.976	0.964	NaN
5	$S_{di}(T_{T1})$	0.234	0.235	-5.683	1.003	NaN	0.248	0.249	-5.512	0.901	NaN	0.211	0.211	-5.538	0.917	NaN
6	$\{S_{di}(T_{T1}); S_{di}(T_{L1})/S_{di}(T_{T1})\}$	0.225	0.228	-5.797	1.075	0.144	0.249	0.251	-5.525	0.906	0.015	0.205	0.206	-5.598	0.949	0.111
7	$\{S_{di}(T_{T1}); S_{di}(T_{L1})\}_{gm}$	0.312	0.311	-5.821	1.118	NaN	0.345	0.348	-5.586	0.855	NaN	0.277	0.278	-5.593	0.942	NaN

(b)

3D - Vector sum

| No.	IM	Orientation 1 - FP-FN					Orientation 2 - FN-FP					Orientation 3 - Hor2-Hor1				
		$\sigma_{lnEDP\|IM}$	$\sigma_{lnEDP\|IM,M,R}$	β_0	β_1	β_2	$\sigma_{lnEDP\|IM}$	$\sigma_{lnEDP\|IM,M,R}$	β_0	β_1	β_2	$\sigma_{lnEDP\|IM}$	$\sigma_{lnEDP\|IM,M,R}$	β_0	β_1	β_2
1	$S_a(T_{L1})$	0.456	0.424	-2.970	0.623	NaN	0.388	0.379	-2.935	0.772	NaN	0.376	0.361	-2.827	0.809	NaN
2	$\{S_a(T_{L1}); S_a(T_{T1})/S_a(T_{L1})\}$	0.321	0.310	-2.681	1.062	0.617	0.324	0.314	-2.712	0.998	0.396	0.295	0.285	-2.761	0.978	0.483
3	$\{S_a(T_{L1})_{gm}; S_a(T_{T1})_{gm}/S_a(T_{L1})_{gm}\}$	0.321	0.308	-2.639	1.062	0.495	0.321	0.308	-2.706	1.009	0.482	0.283	0.274	-2.762	0.986	0.485
4	$\{S_a(T_{L1}); S_a(T_{T1})\}_{gm}$	0.324	0.312	-2.648	1.064	NaN	0.328	0.316	-2.734	0.978	NaN	0.293	0.283	-2.762	0.978	NaN
5	$S_{di}(T_{L1})$	0.397	0.377	-4.996	0.780	NaN	0.289	0.290	-5.267	0.826	NaN	0.315	0.307	-5.210	0.850	NaN
6	$\{S_{di}(T_{L1}); S_{di}(T_{T1})/S_{di}(T_{L1})\}$	0.207	0.208	-5.508	1.024	0.665	0.228	0.226	-5.451	0.980	0.364	0.180	0.177	-5.480	1.000	0.563
7	$\{S_{di}(T_{L1}); S_{di}(T_{T1})\}_{gm}$	0.221	0.220	-5.538	1.055	NaN	0.237	0.233	-5.406	0.975	NaN	0.181	0.178	-5.484	1.002	NaN

(c)

Table 5 Regression results for δ_{max} computed using the 3D model. (a) $\delta_{max,L}$, (b) $\delta_{max,T}$, and (c) $\delta_{max,sum}$.

2D - Longitudinal

No.	IM	Orientation 1 - FP				Orientation 2 - FN				Orientation 3 - Hor2			
		$\sigma_{lnEDP\|IM}$	$\sigma_{lnEDP\|IM,M,R}$	β_0	β_1	$\sigma_{lnEDP\|IM}$	$\sigma_{lnEDP\|IM,M,R}$	β_0	β_1	$\sigma_{lnEDP\|IM}$	$\sigma_{lnEDP\|IM,M,R}$	β_0	β_1
1	$S_a(T_{L1})$	0.416	0.421	-2.793	0.973	0.469	0.474	-2.873	0.938	0.394	0.397	-2.498	1.192
2	$S_a(T_{L1})_{gm}$	0.456	0.459	-2.821	1.058	0.501	0.506	-2.726	1.024	0.426	0.430	-2.562	1.215
3	$\{S_a(T_{L1}); S_a(T_{T1})\}_{gm}$	0.467	0.472	-2.917	1.051	0.495	0.499	-2.826	1.007	0.432	0.436	-2.651	1.224
4	$S_{di}(T_{L1})$	0.430	0.431	-5.513	0.933	0.490	0.496	-5.460	0.871	0.393	0.397	-5.903	1.203

**Table 6** Regression results for $\delta_{max,L}$ computed using the 2D longitudinal model. Compare with Table 5a.

2D - Transverse

| No.	IM	Orientation 1 - FN				Orientation 2 - FP				Orientation 3 - Hor1			
		$\sigma_{lnEDP\|IM}$	$\sigma_{lnEDP\|IM,M,R}$	β_0	β_1	$\sigma_{lnEDP\|IM}$	$\sigma_{lnEDP\|IM,M,R}$	β_0	β_1	$\sigma_{lnEDP\|IM}$	$\sigma_{lnEDP\|IM,M,R}$	β_0	β_1
1	$S_a(T_{T1})$	0.267	0.270	-3.327	0.927	0.300	0.302	-3.586	0.743	0.252	0.253	-3.424	0.857
2	$S_a(T_{T1})_{gm}$	0.350	0.356	-3.325	0.895	0.357	0.359	-3.676	0.769	0.262	0.266	-3.423	0.887
3	$\{S_a(T_{T1}); S_a(T_{L1})\}_{gm}$	0.346	0.351	-3.206	0.943	0.349	0.345	-3.579	0.791	0.260	0.262	-3.312	0.912
4	$S_{di}(T_{T1})$	0.207	0.210	-6.117	1.195	0.276	0.273	-5.625	0.854	0.163	0.160	-5.913	1.047

Table 7 Regression results for $\delta_{max,T}$ computed using the 2D-model of the transverse frame. Compare with Table 5b.
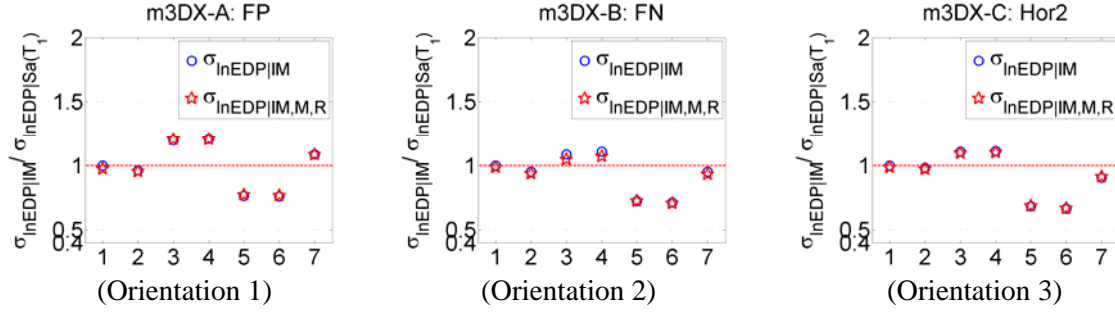
Figure 46 Gain or loss in the explained variability of $\delta_{max,L}$ computed via the 3D model when using a pool of predictors different from the single $S_a(T_{L1})$. Given that the ratio of standard errors of estimation is shown, a ratio less than 1 means gain and greater than 1 means loss. Compare to the analysis cases in Table 5a.
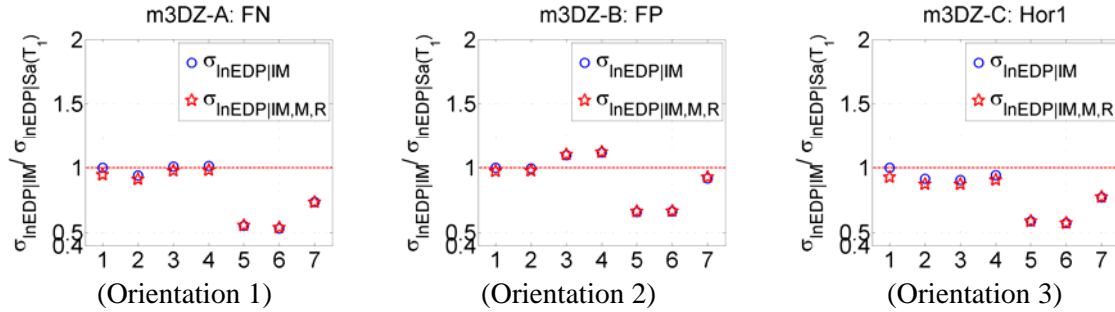

Figure 47 Gain or loss in the explained variability of $\delta_{max,T}$ computed via the 3D model when using a pool of predictors different from the single $S_a(T_{T1})$. Compare to the analysis cases in Table 5b.
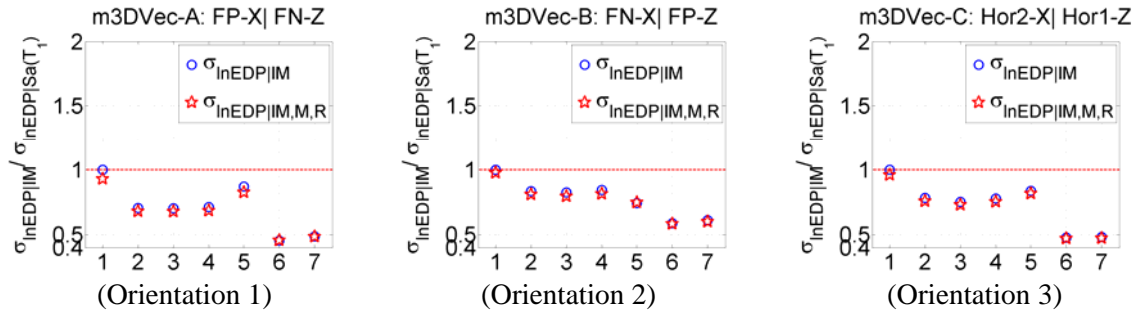
Figure 48 Gain or loss in the explained variability of $\delta_{max,sum}$ computed via the 3D model when using a pool of predictors different from the single $S_a(T_{L1})$. Compare to the analysis cases in Table 5c.
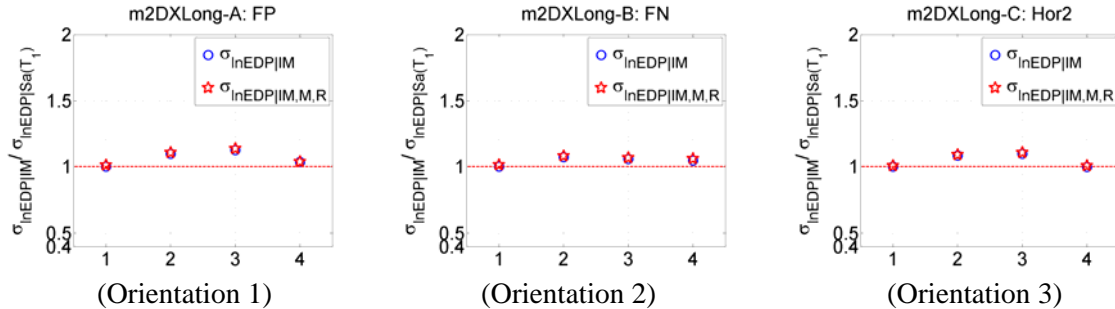
Figure 49 Gain or loss in the explained variability of $\delta_{max,L}$ computed via the 2D model of the longitudinal frame when using a pool of predictors different from the single $S_a(T_{L1})$. Compare to the analysis cases in Table 6.
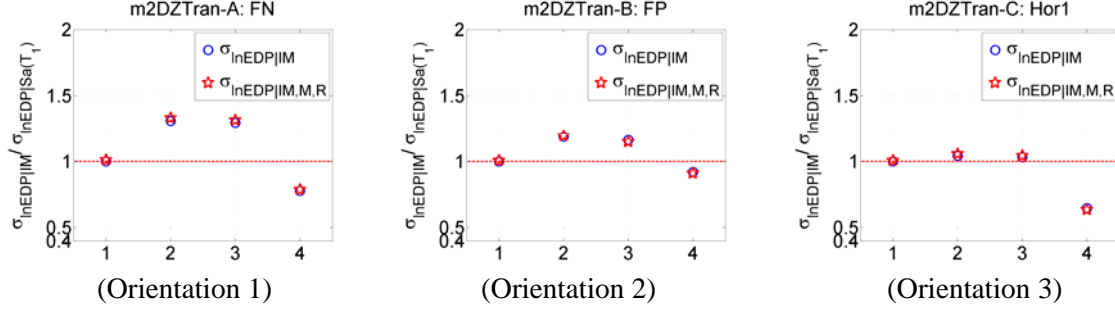
Figure 50 Gain or loss in the explained variability of $\delta_{max,T}$ computed via the 2D model of the transverse frame when using a pool of predictors different from the single $S_a(T_{T1})$. Compare to the analysis cases in Table 7.

From the inspection of these tables and figures the following main general conclusions can be drawn:

- The prediction of $\delta_{max,L}$ and $\delta_{max,T}$ is accurately and efficiently done with the knowledge of a single *IM* (e.g., $S_{di}(T_{L1})$ and $S_{di}(T_{T1})$) computed from the arbitrary component of the record acting in the direction of the response. The addition of any *IM* from the ground motion acting in the orthogonal direction, either as a part of vectorized *IM* or as a part of a single *IM* that contains the geometric mean of two *IM*'s acting along both major axes of the building, does not appreciably improve the prediction of $\delta_{max,L}$ and $\delta_{max,T}$. This implies that torsional effects in this building are small.

- The prediction of $\delta_{max,sum}$ is accurately and efficiently done using a single *IM* that combines in a geometric mean fashion two *IM*'s from both records acting along the two major structural axes. The single *IM* that combines inelastic spectral displacements, i.e., $(S_{di}(T_{L1});S_{di}(T_{L1}))_{gm}$ is the best choice. The use of $(S_{di}(T_{L1});S_{di}(T_{L1}))_{gm}$ provides an additional reduction in response variability compared to the base cases with either $S_a(T_{L1})$ or $S_a(T_{T1})$ between 41% and 55% depending on building orientations. A minor improvement in the prediction of $\delta_{max,sum}$ can be achieved by considering $S_{di}(T_{L1})$ and $S_{di}(T_{L1})$ separately in a vector form, but the slight improvement in accuracy does not justify the selection of this more complicated vector *IM*.

- Using $S_{di}(T_{L1})$ and $S_{di}(T_{T1})$ rather than the spectral acceleration counterparts $S_a(T_{L1})$ and $S_a(T_{T1})$ reduces the uncertainty in the prediction of $\delta_{max,L}$ and $\delta_{max,T}$ by 25 to 45% for the different orientations of the building. Similarly, using $(S_{di}(T_{L1}); S_{di}(T_{L1}))_{gm}$ rather than $(S_a(T_{L1}); S_a(T_{L1}))_{gm}$ lowers the variability by 30 to 40% in the prediction of $\delta_{max,sum}$.

- The $\sigma_{ln\delta|IM}$ values when the best scalar predictors identified above are used vary from about 0.16 to 0.27 across building orientations and models. The only exception is the prediction of $\delta_{max,L}$ in the 2D model that shows values of $\sigma_{ln\delta|IM}$ exceeding 40% even with the best predictors.

- The prediction of $\delta_{max,L}$, $\delta_{max,T}$, and $\delta_{max,sum}$ based on $S_a(T_{L1})$ (or $S_{di}(T_{L1})$) is not improved by considering a vector that includes higher modes *IM*'s, such as $S_a(T_{L2})$ (or $S_{di}(T_{L2})$). For example, the unexplained variability in $\delta_{max,sum}$ drops from 0.362 for the $(S_a(T_{L1}); S_a(T_{T1}))$ case to 0.361 for the case (not shown in the table) of $(S_a(T_{L1}); S_a(T_{T1}); S_a(T_{L2}); S_a(T_{T2}))$. Similarly almost identical $\sigma_{ln\delta|IM}$ values were found for the prediction of $\delta_{max,L}$ and $\delta_{max,T}$.

- In line with the findings of Baker and Cornell (2006a), a regression model that utilizes as response predictor an *IM* computed from the geometric mean of the two horizontal components rather than from the applied arbitrary component results in a larger unexplained response variability.

- Given that both frames have comparable displacements when subject to ground motions of similar intensity, the prediction of $\delta_{max,sum}$ can be done fairly accurately using conventional scalar *IM*'s, such as $S_a(T_{L1})$ or $S_a(T_{T1})$ provided that the *IM* for the stronger horizontal component is used. The direction of stronger ground motion, however, is not known for future earthquakes.

42

When a building has one major axis oriented as the fault strike and comparable drifts along both axes, an alternative but less effective option is to use the S_a of the fault normal component.

- The additional prediction power of M and R when $S_a(T_1)$ or $S_{di}(T_1)$ are already in the pool of predictors is minimal. For example, for the values of $\sigma_{ln\delta|IM}$ for the prediction of $\delta_{max,T}$ in the 3D longitudinal model were 0.42 for the case of $IM=S_a(T_{T1})$ and 0.40 for the case of $IM=\{S_a(T_{T1}), M, R\}$. In some cases the addition of M and R in the regression model even caused the value of $\sigma_{ln\delta|IM}$ to increase due to the loss of 2 degrees of freedom. This finding is in line with other studies (e.g., Bazzurro and Cornell, 1994; Shome *et al.*, 1998; Luco *et al.* 2005a and 2005b; Luco and Cornell, 2007) that analyzed steel moment resisting frame buildings, which are intrinsically less deteriorating systems than the concrete building considered here.

3.4   *Probabilistic interstory drift hazard curves*

Following Shome and Cornell (2000) and Tothong and Cornell (2006a), in the calculation of the drift hazard curves we separated the contributions of "collapse" data (δ_{max}>6%) from that of "non-collapse" data for which IM-δ_{max} relationships were derived (see Equation 1 and Table 5 to Table 7). The following equation is used to perform drift hazard calculation (i.e., MAF of exceeding a given level of structural response, called $\lambda_{\delta_{max}}$ here):

$$\lambda_{\delta_{max}}(x) = \int_{IM} \left\{ P\left[\delta_{max} > x \,|\, IM, NC\right] \cdot \left(1 - P_{Col|IM}\right) + P_{Col|IM} \right\} \cdot \left| d\lambda_{IM} \right| \tag{2}$$

where NC stands for non-collapse data, $\left| d\lambda_{IM} \right|$ is approximately the absolute value of the ground motion hazard curve or surface *equaling* a given value (or a set of values) of an IM. The first factor of the integrand can be estimated by using a linear regression analysis of $\ln \delta_{max}$ and $\ln IM$ (Hastie *et al.*, 2001) mentioned earlier. To estimate $P_{Col|IM,}$ that is the probability of collapse for a given value of an IM (or a set of values for vector IM), we used a logistic regression approach (e.g., McCullagh and Nelder 1990).

The drift hazard curves for $\delta_{max,L}$, $\delta_{max,T}$, and $\delta_{max,sum}$ computed using the drift estimates based on the 3D model analyses for the three building orientations and relevant cases (see Table 4) are shown in Figure 51 to Figure 53, respectively. The corresponding drift hazard curves for $\delta_{max,L}$ and $\delta_{max,T}$ based on the 2D model drifts are similar to those shown and only the ratios of the 2D vs. 3D curves will be shown later. To better compare and contrast these curves we also show (Figure 54) the ratio of all the drift curves to that of the base case. As discussed in the previous subsection, for both $\delta_{max,L}$ and $\delta_{max,T}$ the base case (Case 14 in Table 4) considers $S_{di}(T_{L1})$ and $S_{di}(T_{T1})$, respectively, as the predictors of choice with drift results based on the 3D model. For $\delta_{max,sum}$ the base case (Case 16 in Table 4) uses $(S_{di}(T_{L1});S_{di}(T_{T1}))_{gm}$ as predictor and, of course, results from the 3D model. For $\delta_{max,L}$, $\delta_{max,T}$ the cases with FN component acting in the longitudinal (Orientation 2) and transverse direction (Orientation 1) are shown, respectively. The Orientation 1 case is presented for $\delta_{max,sum}$. The ratios of drift hazard curves for the omitted cases are generally closer to one compared to those shown.
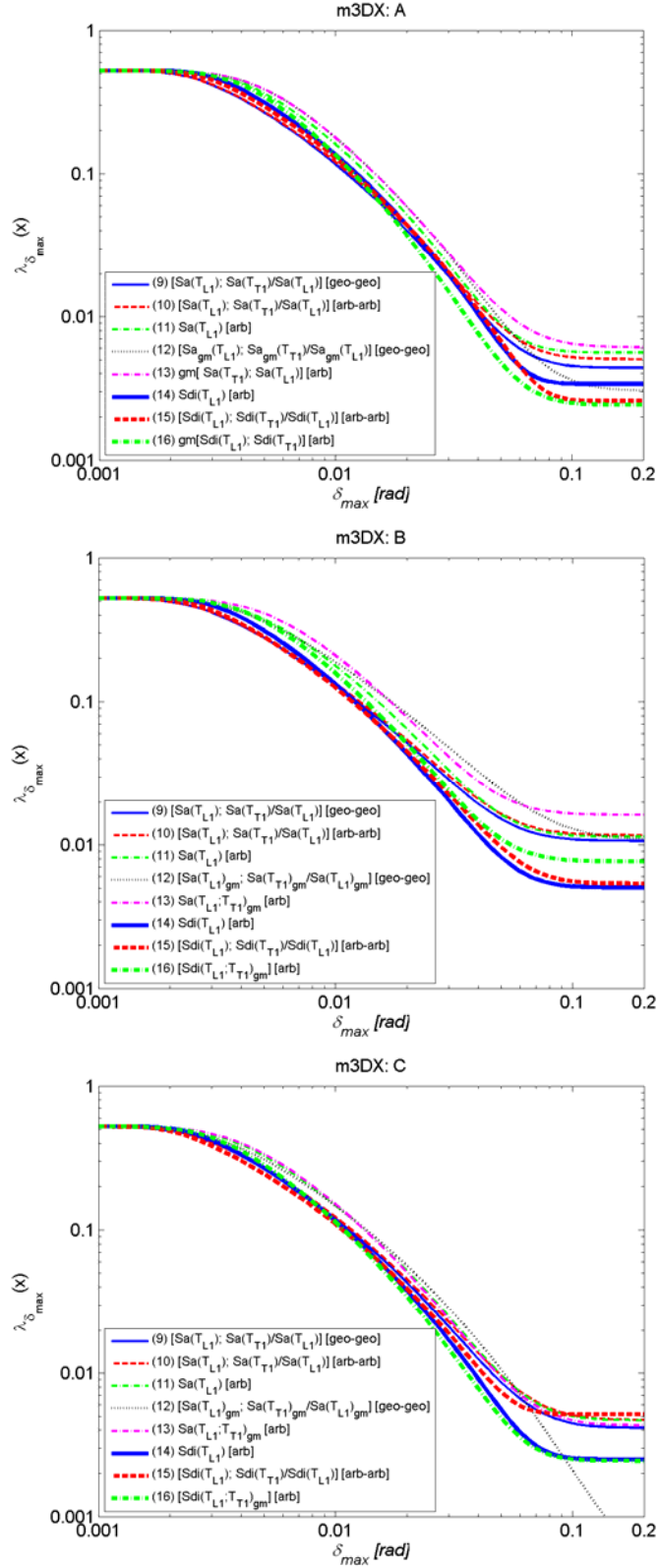
Figure 51 Drift hazard curves for $\delta_{max,L}$ computed using the 3D model analyses, the 8 combinations of *IM*'s defined in Table 4 (Cases 9 to 16), and the three orientations of the building: (top) Orientation 1 - FN; (middle) Orientation 2 - FP; and (bottom) Orientation 3 (undefined angle).

44
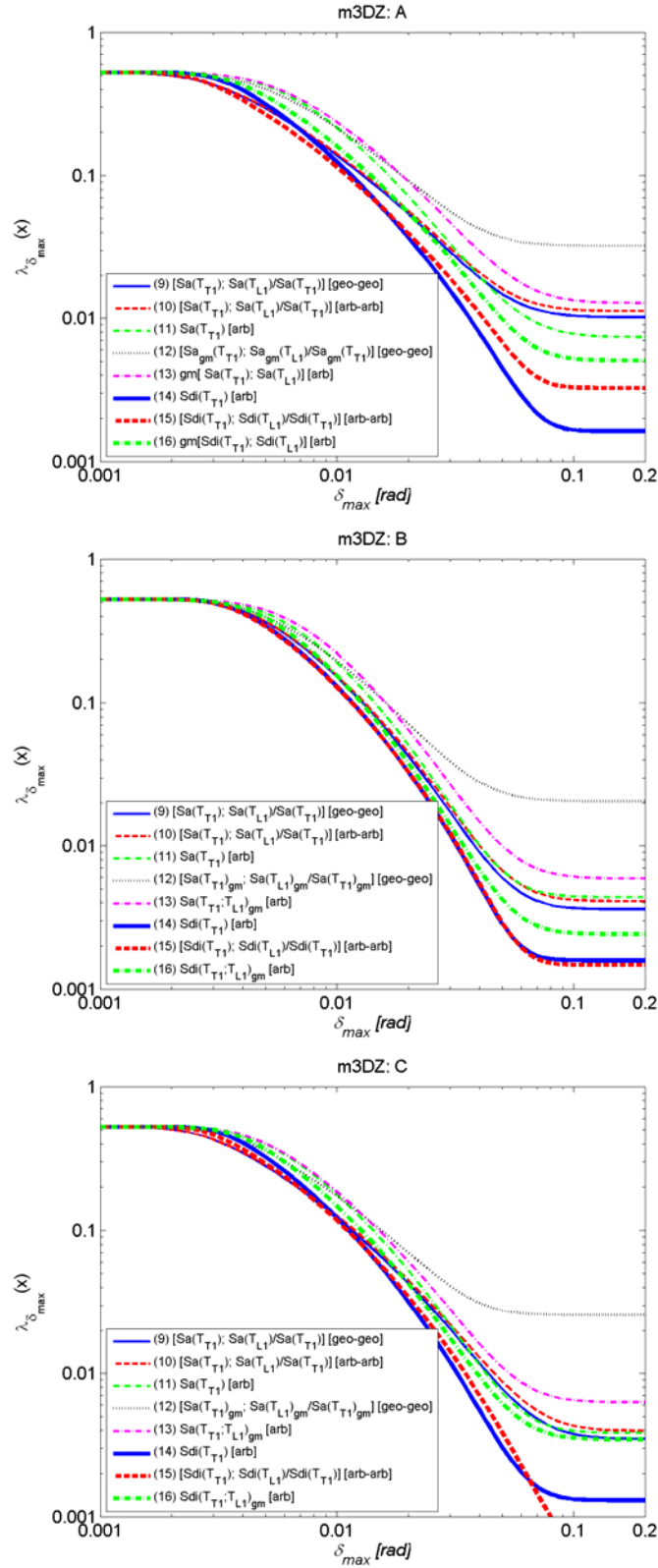
Figure 52 Drift hazard curves for $\delta_{max,T}$ computed using the 3D model analyses, the 8 combinations of *IM*'s defined in Table 4 (Cases 9 to 16), and the three orientations of the building: (a) Orientation 1 - FN; (b) Orientation 2 - FP; and (c) Orientation 3 (undefined angle).

45
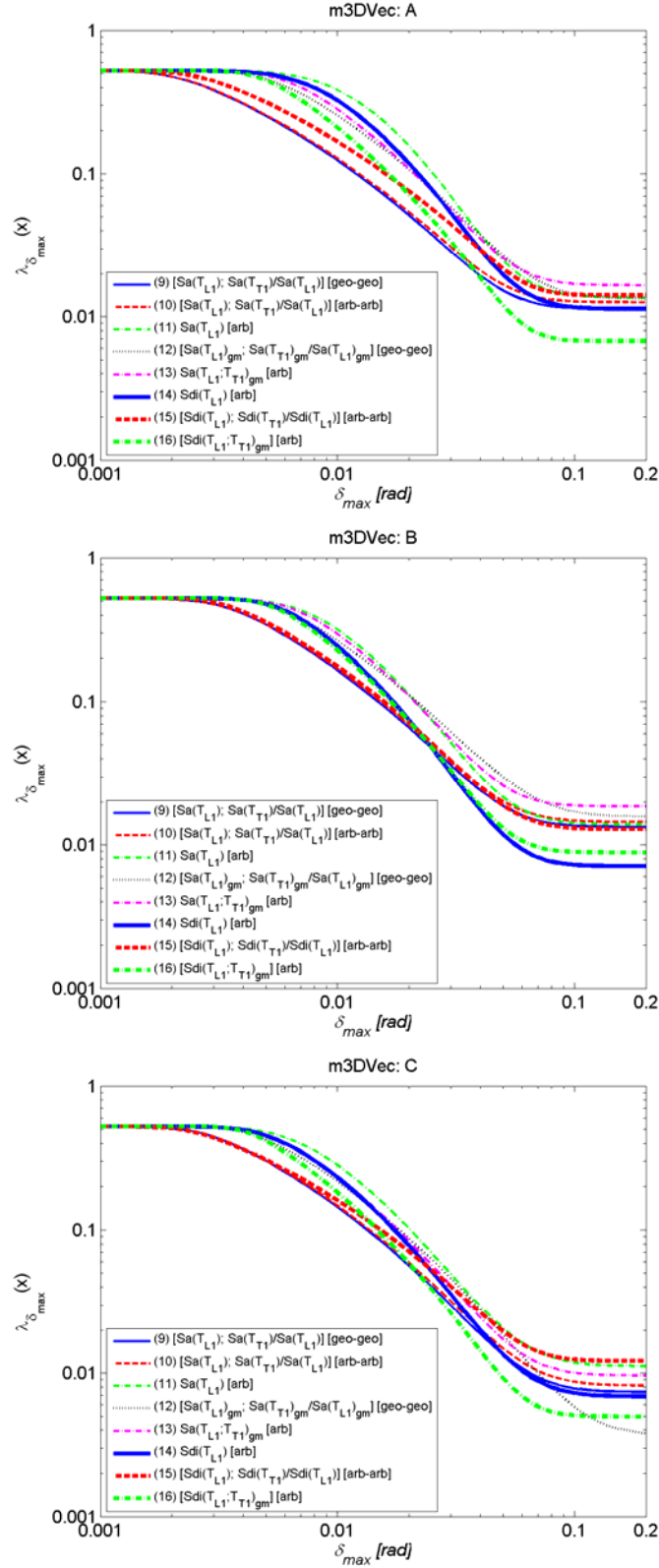
Figure 53 Drift hazard curves for $\delta_{max,sum}$ computed using the 3D model analyses, the 8 combinations of IM's defined in Table 4 (Cases 9 to 16), and the three orientations of the building: (a) Orientation 1 - FN; (b) Orientation 2 - FP; and (c) Orientation 3 (undefined angle).

46
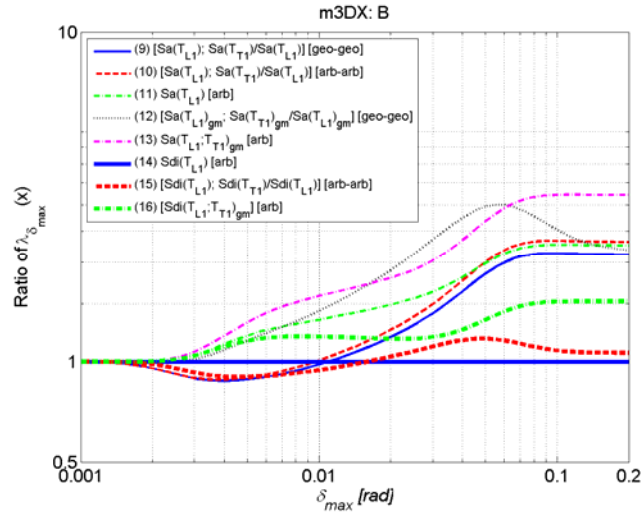
($\delta_{max,L}$ -- Orientation 2)
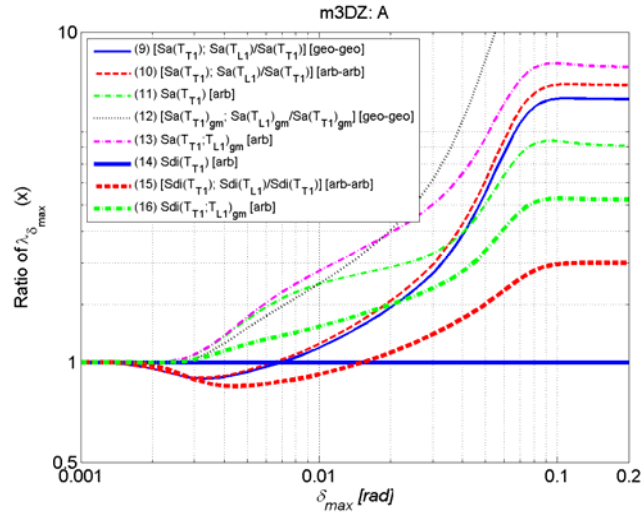
($\delta_{max,T}$ -- Orientation 1)
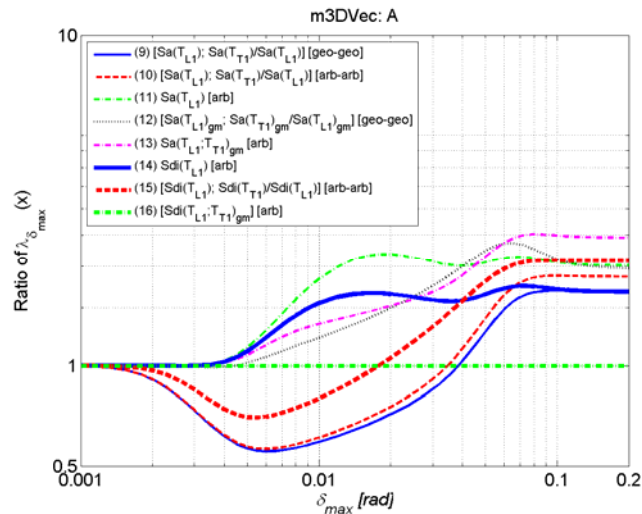
($\delta_{max,sum}$ -- Orientation 1)

Figure 54 Ratio of drift curves for $\delta_{max,L}$, $\delta_{max,T}$, and $\delta_{max,sum}$.

The main general conclusions applicable to this building stemming from the inspection of these figures and those that follow are:

- The selection of the *IM* used for the prediction of δ_{max} has a significant impact on the drift hazard curves especially for drift levels exceeding 1%. For δ_{max} values up to about 0.3%, which can be associated with no damage to minor damage states, almost any choice of *IM* will yield the same drift hazard curve.

- As expected, the higher unexplained variability in the response for some *IM's* (e.g., $(S_a(T_{L1});S_a(T_{T1}))_{gm}$ in Case 13 for $\delta_{max,L}$) compared to that of the base case is reflected in a hazard drift curve higher than that of the base case. The hazard curves with inferior predictors at δ_{max} levels of 3% to 4%, which are associated with severe damage and perhaps collapse in some cases, are usually up to about 100% higher than that of the base case. At δ_{max} values around 1%, which imply moderate damage, the difference is usually within 60%.

- The drift hazard curves flatten for very large δ_{max} values due to the explicit consideration of collapse via logistic regression.

- As expected, drift hazard curves for $\delta_{max,sum}$ are higher than those for $\delta_{max,L}$ and $\delta_{max,T}$. This is because $\delta_{max,sum} \geq \delta_{max,L}$ *or* $\delta_{max,T}$.

- The effect of the anisotropy of the hazard is reflected, generally, in higher drift hazard curves for the drift along the axes that are subject to the fault normal component (Figure 55a). This is evident when comparing the hazard for the building orientations subject to FN components (i.e., T for Orientation 1 and L for Orientation 2) with that for undefined orientation (Orientation 3). The FP comparison, however, does not follow the pattern expected, namely a similar pattern to that of the site hazard (Figure 23 and Figure 30). The reason for this apparent anomaly stands in the sample variability that affects the *IM* vs. *EDP* prediction equation differently in different cases. To show that this is indeed the case we show in Figure 55b the ratios of drift curves that are generated for all three building orientations using the same *IM* vs. *EDP* curve for all cases. The same pattern of the ground motion hazard is found again in the drift hazard case. Note that if we had used an infinite number of records instead of 100, the pattern of Figure 55a would be the same as that of Figure 55b.

- Figure 56 shows the effect of using the 3D model versus the 2D models for the estimation of the building response. For the reasons mentioned earlier the two 2D frames, and especially the transverse one, tend to provide higher δ_{max} values than the 3D model at higher interstory drifts. This is clearly reflected in the figure below where for the same orientation the drift hazard curves based on the 2D model are higher than the corresponding ones based on the 3D model for values higher than 2% for the transverse direction and higher than 0.2% for the longitudinal direction. The ratio of the 2D-based to the 3D-based drift hazard curves is less than 3 (in probability) in both the longitudinal and transverse cases for δ_{max} values less than 4%.

- The similarity in the response of the building in the longitudinal and transverse direction is confirmed by inspecting Figure 56. The drift hazard curves in longitudinal and transverse directions are very similar to one another for all the three orientations of the building, with the longitudinal one being slightly higher.

- Using an IM based on the arbitrary component of the ground motion for predicting the maximum interstory drift and, incorrectly, using the same IM based on the geometric mean of the horizontal components generates a drift hazard curve that is underestimated. The bias however is, for all practical purposes, not significant compared to the variability in the hazard curves introduced by other sources of uncertainty (e.g., record sampling).

- The drift hazard curves based on the longitudinal 2D frame analyses (Figure 56) are higher than others because of the large variability in EDP|IM.

- The drift hazard curves for the transverse 2D frame (Figure 56) flatten about δ_{max} of about 2% to 3% rather than the value of about 6% of the other cases. The flattening of the drift hazard curve

indicates collapse at a smaller δ_{max} (see also Figure 43b). This discrepancy is due to the lack of a gravity frame in the transverse 2D model.
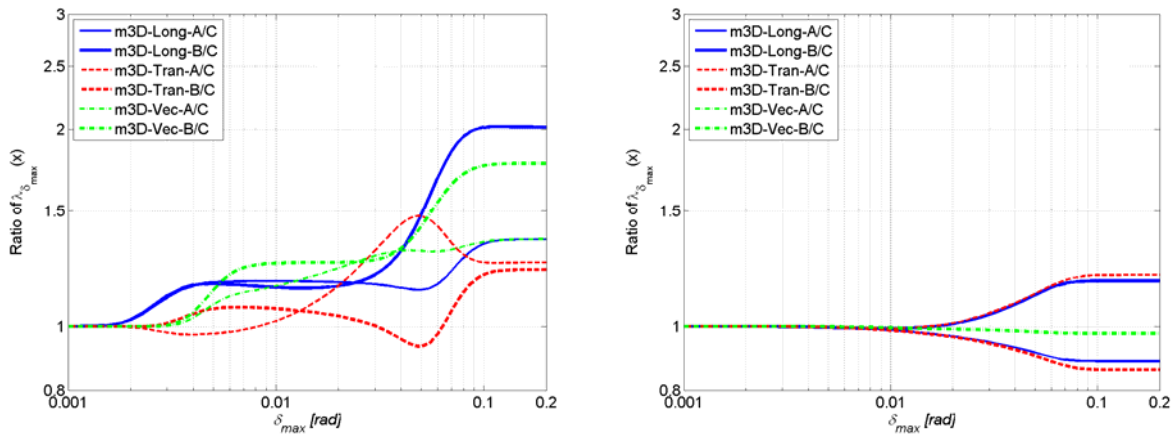
Figure 55 (a) Effect of the building orientation on the likelihood of exceeding a certain maximum interstory drift for the 3D model. The ratio is computed using the drift hazard curves that use the preferred *IM* for this case, namely $S_{di}(T_{L1})$ for $\delta_{max,L}$, $S_{di}(T_{T1})$ for $\delta_{max,T}$, and $(S_{di}(T_{L1}); S_{di}(T_{T1}))_{gm}$ for $\delta_{max,sum}$. (b) Same as in above but the hazard drift curves were generated using the same prediction equation for δ_{max} regardless of the building orientation. Legend: A=Orientation 1 (L-FP); B=Orientation 2 (L-FN); C=Orientation 3 (random).
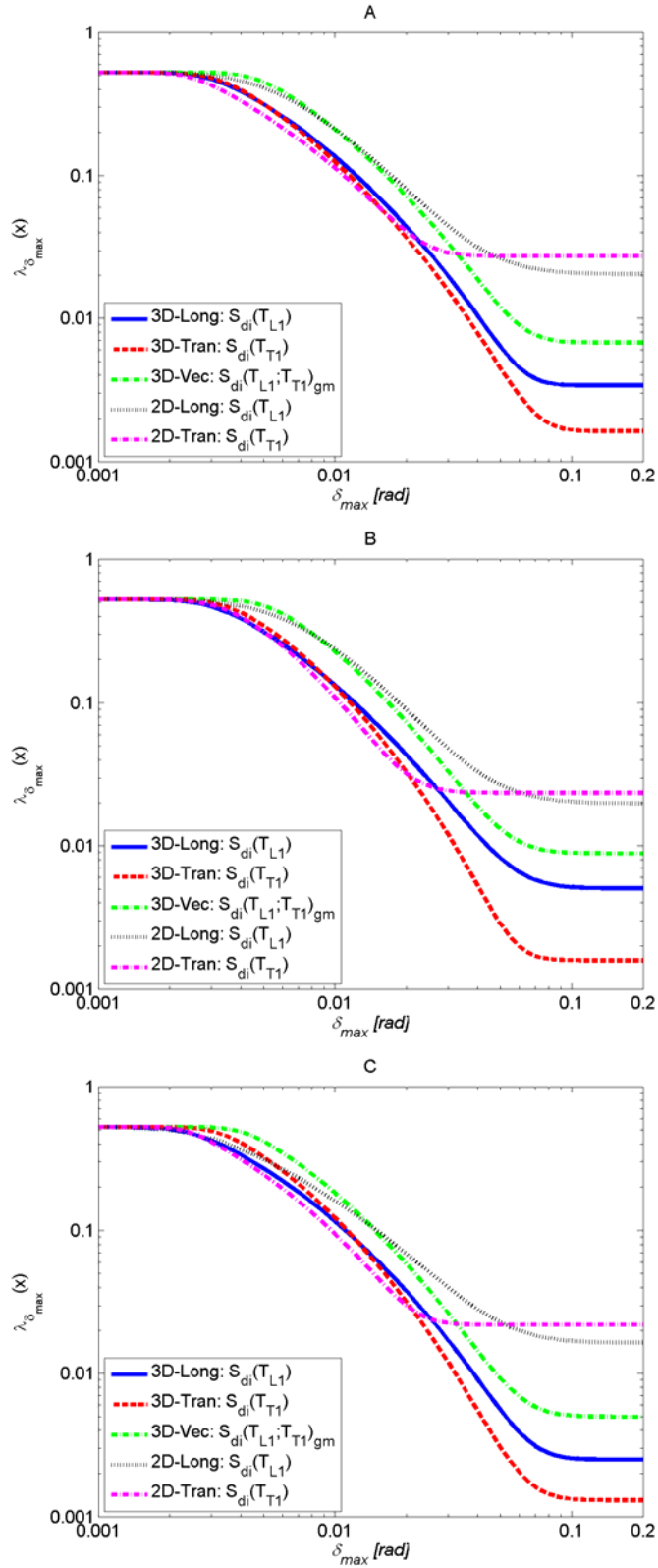
Figure 56 Effects of modeling on drift hazard curves based on analyses done on the 2D and 3D building models. Legend: A=Orientation 1; B=Orientation 2; C=Orientation 3.

3.5   The 30% rule for building design

To "ensure" life safety, under certain conditions several building design codes and guidelines such as the IBC (ICC, 2000), UBC (ICBO, 1997), FEMA356 (FEMA, 2000), and ASCE/SEI 31-03 Standard (ASCE, 2003) recommend designing a building for 100% of the target design ground motion (e.g., the one with 10% probability of exceedance in 50 years) in one horizontal direction plus 30% of the design ground motion in the perpendicular horizontal direction. In particular, the building corner columns should be designed to withstand the combination of such loads. In this section we intend to investigate whether for this 7-story concrete building at the selected San Francisco site the "30% rule" is appropriate or whether it is unconservative. Also, we intend to study whether the appropriateness of the 30% rule may depend on the building orientation with respect to the strike of the causative fault.

To answer these questions we examined the joint hazard of $S_a(T_{L1})$ and $S_a(T_{T1})$ in Figure 19 and Figure 31c for the unspecified orientation and in Figure 21 and Figure 31a for the building with one main axis aligned with the strike of the causative fault, which for this site is approximately N-S. The acceleration values exceeded, on average, 10% of the times in 50 years (i.e., once every 475 years, on average) of $S_a(T_{L1})$ and $S_a(T_{T1})$ for the three building orientations are listed in Table 8. These are the target design ground motion levels, called $S_a(T_{L1})_{475}$ and $S_a(T_{T1})_{475}$ here, that are consistent with the hazard curves and surfaces shown in Figure 18 to Figure 23. Figure 57 to Figure 60 show the probability mass function at this site for one of the ground motion parameters, $S_a(T_{L1})$ or $S_a(T_{T1})$, conditional on the other equaling or exceeding its 475yr MRP value for Orientations 1 and 3. The consequences of the extremely high correlation of $S_a(T_{L1})$ and $S_a(T_{T1})$ are that, should the 475yr MRP value of, say, $S_a(T_{L1})$ be observed at the site, then almost certainly $S_a(T_{T1})$ would exceed 30% of $S_a(T_{T1})_{475}$. In fact, for Orientation 1 of the building the median value of $S_a(T_{T1})|S_a(T_{L1}){\cong}S_a(T_{L1})_{475}$=0.695g is 0.696g (Figure 57a), which is 3 times larger than the value of 0.3 x $S_a(T_{T1})_{475}$ =0.231g that is recommended by the 30% rule. The value of 0.696g, which is actually about 90% of $S_a(T_{T1})_{475}$, would be exceeded in the transverse direction half of the times if the design ground motion $S_a(T_{L1})_{475}$ were to happen in the longitudinal direction. For the same Orientation 1 of the building similar considerations can be made for the dual design case when the design of the corner column is done for $S_a(T_{T1})_{475}$ and a fraction of $S_a(T_{L1})_{475}$. In this case Figure 58a shows that the median of $S_a(T_{L1})|S_a(T_{T1}){\cong}S_a(T_{T1})_{475}$=0.77g is 0.698g, which is about 100% of $S_a(T_{L1})_{475}$. In the random Orientation 3 case (Figure 59a), the median value of $S_a(T_{T1})|S_a(T_{L1}){\cong}S_a(T_{L1})_{475}$=0.717g is 0.736, more than 3 times larger than the value of 0.221g recommended by the code, and the median of $S_a(T_{L1})|S_a(T_{T1}){\cong}S_a(T_{T1})_{475}$=0.757g is 0.664g, more than 3 times larger than the code value of 0.221g.

Alternatively, one may consider that the ground motion adopted by the code has 10% probability in 50 years of been exceeded. Hence, the spirit of the code can be interpreted in this context by conditioning on $S_a(T_{L1}){\geq}S_a(T_{L1})_{475}$ when computing the conditional distribution of $S_a(T_{T1})$ rather than on $S_a(T_{L1}){\cong}S_a(T_{L1})_{475}$. Under this perspective, for example, for Orientation 1 of the building the median value of $S_a(T_{T1})|S_a(T_{L1}){\geq}S_a(T_{L1})_{475}$ is 0.835g, that is 108% the value of $S_a(T_{T1})_{475}$. Similar conclusions can be drawn for the other cases.

Note that the high correlation of $S_a(T_{L1})$ and $S_a(T_{T1})$ of the case discussed here may be considered an upper bound because $T_{L1}{\cong}T_{T1}$ and because of the common orientation of all the major faults around the site. When the ground motion parameters are less correlated due to periods of vibrations in orthogonal directions that are farther apart and because of more varied orientations of faults around the site (such as in Southern California) the correlation coefficient, ρ_{tot}, of $S_a(T_{L1})$ and $S_a(T_{T1})$ may go down to values perhaps around 0.5. In these less correlated cases, the median value of $S_a(T_{L1})|S_a(T_{T1}){\cong}S_a(T_{T1})_{475}$ would be significantly lower than the values exceeding 90% reported above. These median values, however, are expected to be in the neighborhood of the 30% suggested by the code only for values of $\rho_{\varepsilon 12}{\cong}0.3$ to 0.4

that occur only for extreme (and very rare cases) cases when T_{L1} and T_{T1} are very different (namely, $T_{L1}/T_{T1}>4$).

|	$S_a(T_{L1})_{475}$ (g)	$S_a(T_{T1})_{475}$ (g)
Orientation 1	0.695	0.77
Orientation 2	0.737	0.735
Orientation 3	0.717	0.757

Table 8 $S_a(T_{L1})$ and $S_a(T_{T1})$ 475 mean return period (MRP) values for the site, called here $S_a(T_{L1})_{475}$ and $S_a(T_{T1})_{475}$, for the three building orientations.
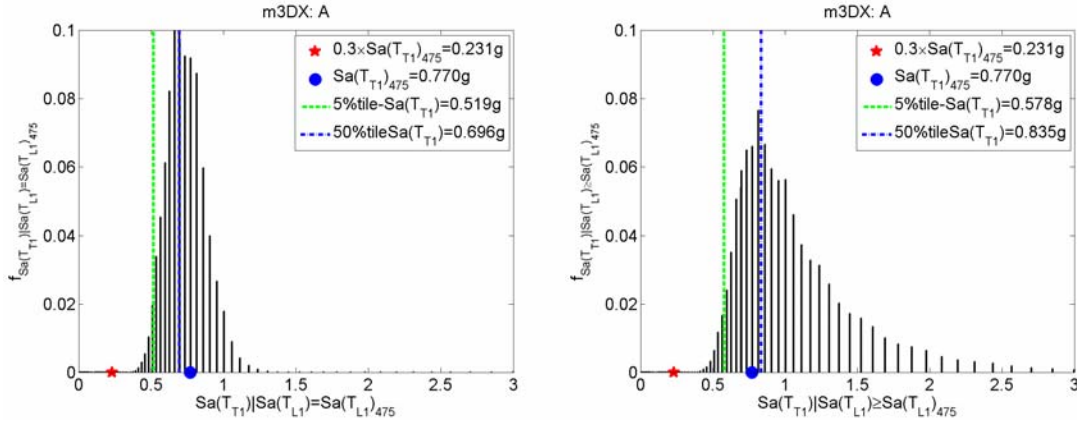

Figure 57 Probability mass function of $S_a(T_{T1})|S_a(T_{L1})\cong S_a(T_{L1})_{475}=0.77g$ and of $S_a(T_{T1})|S_a(T_{L1})\geq S_a(T_{L1})_{475}$ for Orientation 1 of the building (longitudinal frame of the building aligned with the fault parallel direction).
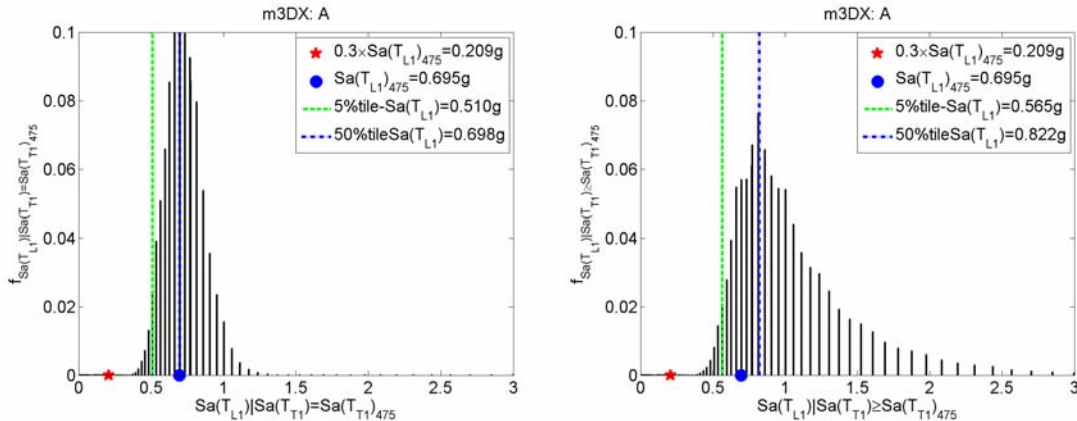
Figure 58 Probability mass function of $S_a(T_{L1})|S_a(T_{T1})\cong S_a(T_{T1})_{475}=0.82g$ and of $S_a(T_{L1})|S_a(T_{T1})\geq S_a(T_{T1})_{475}$ for Orientation 1.
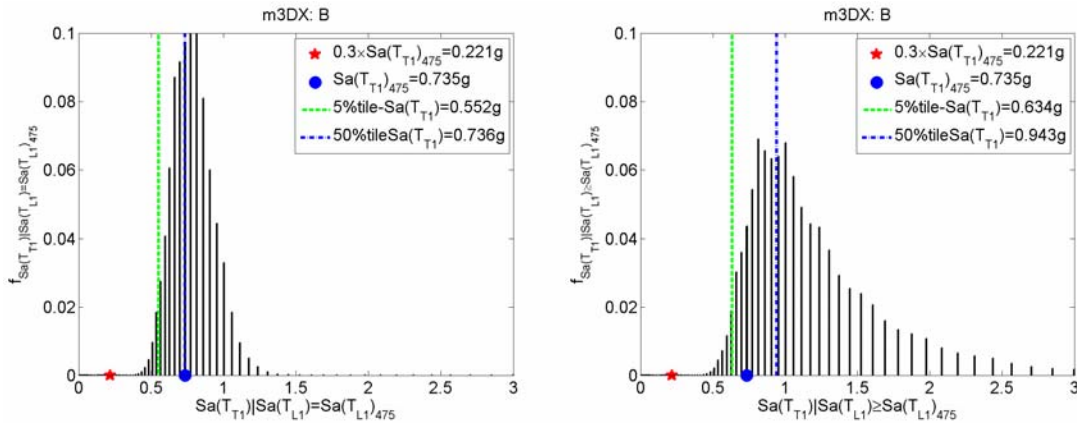
Figure 59 Probability mass function of $S_a(T_{TI})|S_a(T_{LI}) \cong S_a(T_{TI})_{475} = 0.79g$ and of $S_a(T_{TI})|S_a(T_{LI}) \geq S_a(T_{TI})_{475}$ for Orientation 3 (undefined angle).
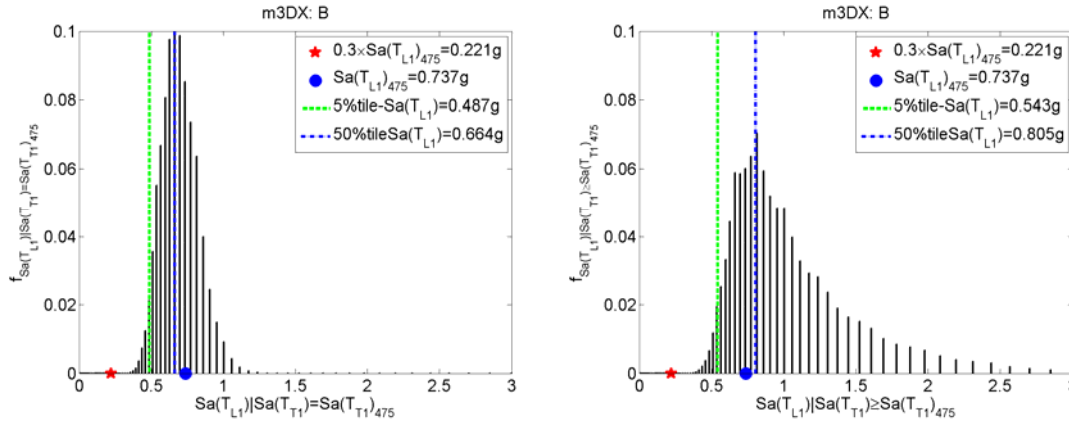
Figure 60 Probability mass function of $S_a(T_{LI})|S_a(T_{TI}) \cong S_a(T_{TI})_{475} = 0.79g$ and of $S_a(T_{TI})|S_a(T_{LI}) \geq S_a(T_{TI})_{475}$ for the Orientation 3 (undefined angle).

4   CONCLUSIONS

This study has addressed some of the issues pertinent to computing the likelihood of exceeding acceptable seismic responses for buildings located close to faults. In particular we have addressed the issues of a) effects of modeling the structure with increasing levels of complexity (two frames in 2 Dimensions or a single 3Dimensional model) on the drift hazard curves, b) predicting the building response in different directions and building orientations with respect to the causative fault using different ground motion parameters, and c) coupling the site hazard (both scalar and vector) with the building response. The study also briefly addressed d) the 30% rule used to design corner columns belonging to moment resisting frames of buildings.

The main lessons learned from this study are:

e) Modeling a structure as a 2D frame or as a 3D entity can result in quite different drift hazard curves and especially different collapse probabilities. When designing 2D frames attention should be devoted to the modeling of the gravity frames if very large deformations are to be predicted accurately. When gravity frames are excluded and leaning columns only are used, then large deformations can be overestimated.

f) Orientation of this building with respect to the fault strike changed the probability of collapse by as much as 70%.

g) The selection of the IM to be used as predictor of *EDP* is important because, for the same building orientation, the drift hazard curves that result may vary by a factor of 2 or more at larger drifts due mainly to the variability of *EDP|IM*. *IM*'s yielding the smallest level of response variability should be preferred. The inelastic spectral displacement at the first period of vibration of the building, $S_{di}(T_1)$, acting in the direction of the response to be predicted is the best single IM among those considered here. When the response of interest is a vector sum of the drifts along the main axes, then an *IM* that combines inelastic spectral displacements in both directions is the best choice. Vectors of *IM*'s turned out to be not particularly useful for the response prediction of this building because the contribution to the response due to higher modes was not significant.

h) The 30%-rule suggested by many building codes appears to be unconservative in most cases of practical interest due to the high correlations of ground motion parameters acting along the main

building axes. The more symmetrical the building (i.e., same period of vibration along the main axes), the more unconservative the 30%-rule.

5   AVAILABILITY OF SEISMIC DATA

The ground motion records used in this study (Table 2) were obtained from the Pacific Earthquake Engineering Research (PEER) database. These records are in ASCII format. The database is available online at http://peer.berkeley.edu/smcat/index.html. The contact name for PEER is: Dr. Yousef Bozorgnia, PEER Associate Director, Tel: 510-231-5779, Fax: 510-231-9471, E-mail: yousef@berkeley.edu.

6   ACKNOWLEDGEMENTS

The preliminary modeling work by Brian Sjoberg is gratefully acknowledged. We also thank Nicolas Luco for the insightful discussions on the scope of this study, Jack Baker for providing information about the variance-covariance structure of rotated ground motions, and Nick Gregor for providing a recent version of the hazard code developed by Norm Abrahamson.

7   REFERENCES

Abrahamson, N. (2002). HAZ33 – Software code for PSHA, October.

Abrahamson, N. A., and W. J. Silva (1997), "Empirical Response Spectral Attenuation Relations for Shallow Crustal Earthquakes", *Seismological Research Letters*, Vol. 68 (1), pp. 58-73.

ASCE (2003). "Seismic Evaluation of Buildings", ASCE Standard, ASCE/SEI 31-03, Reston, VA.

Baker, J.W. (2007). Personal communication, June.

Baker, J.W. and C.A. Cornell (2006a). "Which Spectral Acceleration Are You Using?", *Earthquake Spectra*, Vol. 22, No. 2, pp. 293-312.

Baker, J.W. and C.A. Cornell (2006b). "Correlation of Response Spectral Values for Multicomponent Ground Motions", *Bulletin of Seismological Society of America*, February 2006; Vol. 96; No. 1; pp. 215-227; DOI: 10.1785/0120050060.

Bazzurro, P., and C.A. Cornell (1994). ``Seismic Hazard Analysis of Non-Linear Structures. I: Methodology. II: Applications '', *Journal of Structural Engineering*, ASCE, Vol. 120, pp. 3325-3365, November.

Bazzurro, P. (1998). ``Probabilistic Seismic Demand Analysis''. Ph.D. Dissertation, Dept. of Civil and Environmental Engineering, Stanford University, Stanford, CA, August.

Bazzurro, P., and C.A. Cornell (2001). "Vector-valued Probabilistic Seismic Hazard Analysis (abst)''. *Seismological Research Letters*, Vol. 72, No.2, March/April, p.273.

Bazzurro, P., and C.A. Cornell (2002). "Vector-valued Probabilistic Seismic Hazard Analysis (VPSHA)''. *Proceedings of 7th U.S. National Conference on Earthquake Engineering*, Boston, MA, July 21-25, Paper No. 61.

Chopra, A. K. (2001). *Dynamics of Structures: Theory and Applications to Earthquake Engineering*, Second Edition, Prentice Hall, Englewood Cliffs, New Jersey, 844 pp.

Doulatabadi, P.R., (1997) "Three-dimensional nonlinear dynamic seismic behavior of a seven story reinforced concrete building", *Ph.D. thesis*, Department of Civil Engineering, University of British Columbia

Elwood, K.J., Moehle, J.P. (2003). "Shake table tests and analytical studies on the gravity load collapse of reinforced concrete frames" Report PEER 2003/01, Pacific Earthquake Engineering Research (PEER) Center, Richmond,CA

Fajfar, P. (2000). "A nonlinear analysis method for performance-based seismic design." *Earthquake Spectra. Vol. 16, no. 3, pp. 573-592.*

ICC (2000). "IBC -- International Building Code", Prepared by International Code Council, March.

ICBO (1997). UBC -- Uniform Building Code, Vols. 1-3, Prepared by International Conference of Building Officials, Whittier, CA, April.

FEMA (2000). "FEMA356 – Prestandard and Commentary for the Seismic Rehabilitation of Buildings", Washington D.C., November.

Hastie, T., Tibshirani, R., and Friedman, J. (2001), *The elements of statistical learning* 2 ed., Springer-Verlag: 536 pp.

Inoue, T. (1990). " Seismic Hazard Analysis of Multi-Degree-of-Freedom Structures", Rept. RMS-8, Dept. of Civil and Environmental Engineering, Stanford University, Stanford, CA. July.

Jalayer, F. (2006). "Direct Probabilistic Seismic Analysis: Implementing Non-Linear Dynamic Assessments", *Ph.D. Dissertation*, Department of Civil and Environmental Engineering, Stanford University, Stanford, CA, 2003; 244 pp. http://www.stanford.edu/group/rms/.

Luco, L., Manuel, L., Baldava, S., and P. Bazzurro (2005a). "Correlation of Damage of Steel Moment-Resisting Frames to a Vector-valued Ground Motion Parameter Set that includes Energy Demands", Report prepared for U.S. Geological Survey (USGS) Award No. 03HQGR0057, February.

Luco, L., Manuel, L., Baldava, S., and P. Bazzurro (2005b). "Correlation of Damage of Steel Moment-Resisting Frames to a Vector-Valued Set of Ground Motion Parameters", Accepted for publications in *Proceedings of the 9th ICOSSAR05*, June 19-22, Rome, Italy.

Luco, N., and Cornell, C.A. (2007). "Structure-Specific Scalar Intensity Measures for near-Source and Ordinary Earthquake Ground Motions," *Earthquake Spectra*; **23**(2):357-392

McCullagh, P., and Nelder, J. A. (1990), *Generalized linear models*, Second Edition, Chapman & Hall/CRC, 532 pp.

OpenSees (2002). *Open System for Earthquake Engineering Simulation*, (www.opensees.berkeley.edu), Berkeley, California: Pacific Earthquake Engineering Research Center, University of California

PEER (2005). "Van Nuys Hotel Building Testbed Report: Exercising Seismic Performance Assessment", Report PEER 2005/11, H. Krawinkler Editor, Pacific Earthquake Engineering Research (PEER) Center, Richmond,CA

Petersen, M.D. and Arthur D. Frankel (2003). "Incorporating Directivity and Shear Wave Polarization into Probabilistic Seismic Hazard Maps of Southern California", Southern California Earthquake Center (SCEC) Annual Meeting, September 8-10, Palm Springs.

Shome, N., Cornell, C.A., Bazzurro, P., and J.E. Carballo (1998). ``Earthquakes, Records, and Nonlinear MDOF Responses'', *Earthquake Spectra*, Vol. 14, No. 3, August, pp. 469-500.

Shome, N., and C.A. Cornell (2000). "Structural Seismic Demand Analysis: Consideration of Collapse", *Proc. of 8th ASCE Specialty Conference on Probabilistic Mechanics and Structural Reliability*, University of Notre Dame, Notre Dame, IN, July 22-24.

Somerville, P.G., Smith, N.F., Graves, R.W., Abrahamson, N.A. (1997), "Modification of empirical strong ground motion attenuation relations to include the amplitude and duration effect of rupture directivity," *Seismological Research Letters*, 68(1): 199-222.

Stewart, J.P. *et al*. (2001). "Ground Motion Evaluation Procedures for Performance-Based Design", Pacific Earthquake Engineering Research Center, PEER Report 2001/09. College of Engineering, University of California, Berkeley, CA, September.

Theiss, A. (2005). *The impact of beam-column joint damage on the response of an older reinforced concrete frame building*, M.S. Thesis, CE&E Department, University of Washington.

Tothong, P. and Cornell, C.A. (2006a), "Probabilistic seismic demand analysis using advanced ground motion intensity measures, attenuation relationships, and near-fault effects," Pacific Earthquake Engineering Research Center, PEER Report 2006/11. University of California: Berkeley, CA. 2007; 205 pp.

Tothong, P. and Cornell, C. A. (2006b), "An empirical ground motion attenuation relation for inelastic spectral displacement," Bulletin of the Seismological Society of America, 96(6): 2146-2164.

Tothong, P. and Luco, N. (2007), "Probabilistic seismic demand analysis using advanced ground motion intensity measures," Earthquake Engineering & Structural Dynamics: (In press in the special issue: Seismic Reliability Analysis of Structures).